

## N O T I C E

THIS DOCUMENT HAS BEEN REPRODUCED FROM  
MICROFICHE. ALTHOUGH IT IS RECOGNIZED THAT  
CERTAIN PORTIONS ARE ILLEGIBLE, IT IS BEING RELEASED  
IN THE INTEREST OF MAKING AVAILABLE AS MUCH  
INFORMATION AS POSSIBLE

**TWO-DIMENSIONAL ELECTRON BEAM CHARGING MODEL FOR  
POLYMER FILMS**

(NASA-CR-164758) TWO-DIMENSIONAL ELECTRON  
BEAM CHARGING MODEL FOR POLYMER FILMS M.S.  
Thesis (Toronto Univ.) 157 p HC A08/MF A01  
CSCL 11G

N81-32270

G6/27 27459  
Unclas

R.D. Reeves  
Department of Electrical Engineering  
University of Toronto  
Toronto, Canada

September 1981

Prepared under NASA Grant NSG-7647  
Principal Investigator: K.G. Balmain



Funding agencies:  
U.S. Air Force Weapons Laboratory  
U.S. National Aeronautics and Space Administration

# **TWO-DIMENSIONAL ELECTRON BEAM CHARGING MODEL FOR POLYMER FILMS**

**R.D. Reeves  
Department of Electrical Engineering  
University of Toronto  
Toronto, Canada**

**September 1981**

**Prepared under NASA Grant NSG-7647  
Principal Investigator: K.G. Balmain  
Submitted to NASA Lewis Research Center  
21000 Brookpark Road, Cleveland, Ohio  
NASA Technical Officer: J.V. Staskus**

**Funding agencies:  
U.S. Air Force Weapons Laboratory  
U.S. National Aeronautics and Space Administration**

**The material in this report was submitted to the University of  
Toronto in partial fulfilment of the requirements for the  
degree of Master of Applied Science.**

## ABSTRACT

A two-dimensional model is developed to describe the charging of thin polymer films exposed to a uniform mono-energetic electron beam. The study is motivated by observed anomalous behaviour of geosynchronous satellites which has been attributed to electrical discharges associated with the differential charging of satellite surfaces by magnetospheric electrons.

Electric fields both internal and external to the irradiated specimen are calculated at steady state in order to identify regions of high electrical stress. Particular emphasis is placed on evaluating the charging characteristics near the material's edge.

The model has been used to identify and quantify the effects of some of the experimental parameters notably: beam energy; beam angle of incidence; beam current density; material thickness; and material width. Simulations of the following situations have also been conducted: positive or negative precharging over part of the surface; a central gap in the material; and a discontinuity in the material's thickness.



## ACKNOWLEDGMENTS

The author gratefully acknowledges the guidance and support of Professor K.G. Balmain. Many thanks are also due to Miss Margarida Silva for her patience and her proof reading.

Support for this research was provided by the U.S. Air Force Weapons Laboratory and by NASA through Grant NSG-7647, and by the Natural Sciences and Engineering Research Council of Canada through Operating Grant A-4140. The personal financial support of the Natural Sciences and Engineering Council of Canada is acknowledged with gratitude.

## TABLE OF CONTENTS

	Page
1. INTRODUCTION	1
2. ELECTRON BEAM CHARGING EFFECTS IN DIELECTRICS	4
2.1 Introduction	4
2.2 Secondary Emission and Backscatter	4
2.3 Electron Range	11
2.4 Dose Rate	13
2.5 Conductivity	16
2.5.1 Temperature Dependence	17
2.5.2 Photoconductivity	17
2.5.3 Field Dependence	18
2.5.4 Radiation-Induced Conductivity	18
2.6 Optical Effects of Irradiation	22
2.7 Radiation Chemistry	22
2.8 Electrical Breakdown and Surface Discharge	23
3. ONE-DIMENSIONAL MODELLING	24
3.1 External Model Development	24
3.2 External Model Results	29
3.2.1 Steady State Surface Potential	29
3.2.2 Charging Dynamics	32
3.3 Internal Model Development	35
3.4 Internal Model Results	39
3.4.1 Controlled Beam	39
3.4.2 General Front Face Field	40
3.4.3 Grounded Front Face Results	43
3.4.4 Experimental and Numerical Results	44

## TABLE OF CONTENTS (Cont'd...)

	Page
4. TWO-DIMENSIONAL SIMULATION DESCRIPTION	47
4.1 External Charging Model	47
4.1.1 Derivation of Electric Field from an Arbitrary Surface Charge Distribution	49
4.1.2 Incident Current Profile	57
4.1.3 Net Charge Accumulation	58
4.2 Internal Charging Model	60
4.3 Transverse Conduction Current	62
5. SIMPLIFIED ANALYSIS	65
5.1 Central Fields of a Uniform Charge Distribution	65
5.2 Surface Fields	75
6. TWO-DIMENSIONAL NUMERICAL RESULTS AND DISCUSSION	82
6.1 Beam Energy Dependence for Teflon	82
6.2 Material Width Dependence for Teflon	100
6.3 Beam Angle Dependence for Teflon	105
6.4 Material Thickness Dependence for Teflon	113
6.5 Non-conventional Charging Geometries for Teflon	113
6.5.1 Grounded Central Slot	113
6.5.2 Precharging Effects	121
6.5.3 Non-uniform Material Thickness	125
6.6 Beam Current Dependence for Kapton	129
6.7 Tangential Current Results for Kapton	132
7. CONCLUSIONS	143
REFERENCES	146

# PRINCIPAL SYMBOLS

A, B	coefficients for linear charge distribution, $A + Bz$
BE	beam energy (keV)
BS	backscatter emission coefficient
C	capacitance per unit area ( $F/cm^2$ )
d	material thickness (cm)
$\bar{D}$	displacement density vector ( $C/cm^2$ )
$\dot{D}$	dose rate (rads/sec)
$\bar{E}$	electric field vector (V/cm)
$E_{ff}$	internal front face field (V/cm)
e	magnitude of electron charge (C)
G	coefficient for radiation induced conductivity ( $\Omega cm \text{ rad/sec}$ ) <sup>-1</sup>
g	conductivity ( $\Omega cm$ ) <sup>-1</sup>
$J_b$	beam current density ( $A/cm^2$ )
$J_{bs}$	backscatter current density ( $A/cm^2$ )
$J_c$	conduction current density ( $A/cm^2$ )
$J_i$	incident current density at surface ( $A/cm^2$ )
$J_{se}$	secondary emission current density ( $A/cm^2$ )
K	coefficient for secondary emission (keV)
KE	kinetic energy of electron (keV)
$KE_m$	kinetic energy where secondary emission is maximized (keV)
$KE_1, KE_2$	first and second unity emission energies (keV)
m	mass of an electron (kg)
q	volume charge distribution ( $C/cm^3$ )
$\bar{r}$	average electron range (cm)
SE	secondary emission coefficient

T	elapsed time in trajectory calculation (sec)
t	time increment in trajectory calculation (sec)
V	surface potential (kV)
w	material half width (cm)
x,y,z	rectangular coordinates
$\delta$	material density (gm/cm <sup>3</sup> )
$\epsilon_r$	relative dielectric permittivity
$\theta_b$	beam angle with respect to surface normal (degrees)
$\theta_i$	incident electron angle at surface (degrees)
$\phi$	potential (V)
$\rho$	net surface charge density (C/cm <sup>2</sup> )

## 1. INTRODUCTION

Geosynchronous satellites in the early seventies exhibited anomalous behaviour which at that time defied explanation. Telemetry indicated non-existent status changes, antenna gains changed in the absence of commands, tracking and spin stabilization were momentarily lost and occasional loss of communications led to total mission failure [Rosen, 1975]. Of more than 150 communications and remote sensing satellites now in geosynchronous orbit about 30 have had unexplained and seemingly random anomalies. Correlational studies indicated that these failures occurred mainly in the midnight-to-dawn local time period and that electron spectrometers in orbit simultaneously registered unusually high fluxes of energetic electrons. In other words, the problem was linked to an environmental effect rather than random component failures [Sharp et al, 1970]. Analysis of the ATS-5 satellite plasma detector data by De Forest [1972] suggested the possibility that such satellites could be charged by ionospheric electrons to potentials greater than 10 kV. Actual confirmation that the charging and violent discharging process does occur in geosynchronous orbit was established in recent reports from the ATS-5, ATS-6 and SCATHA satellites [Stevens, 1980; Koons, 1980].

Synchronous satellite orbits are circular, with a radius of 6.6 earth radii. In the midnight-to-dawn sector of such orbits, the satellite environment can become filled with a hot plasma during magnetic substorms. Electron energies encountered range from 3-200 keV [Hirshberg and Colburn, 1969] during such intervals and the accumulated satellite charge can therefore result in high spacecraft potentials. The electron current density is approximately 0.1 to 10 nA/cm<sup>2</sup> [McPherson and Schober, 1976]. The proton current density during the substorm is estimated to be only 3% of the

electron current density [Inouye, 1976].

The abrupt loss of charge (discharge) generates electromagnetic interference which can couple into control systems and temporarily degrade their performance. Repetitive discharging has caused some surface damage to such materials as optical surfaces, solar cell arrays and thermal control surfaces thus possibly reducing their useful lifetime. The potential gradient that develops about the satellite can also perturb normal magnetospheric conditions sufficiently to render useless some scientific measurements of the environment.

An understanding of the behaviour of materials under charged particle bombardment is essential to the prediction and prevention of the adverse effects associated with spacecraft charging. Such an understanding has been sought through ground based tests on the charging and discharging characteristics of dielectrics when exposed to uniform monoenergetic electron beams [Balmain and Dubois, 1979; Aron and Staskus, 1979; Stevens et al, 1977; Robinson, 1977; Purvis et al, 1979]. Typical experimental layouts employ small ( $< 100 \text{ cm}^2$ ) planar samples mounted on a conducting substrate. Measurements indicate that a large fraction (25 - 50%) of the trapped charge can leave the surface in the form of blowoff electrons during the discharge event, a phenomenon referred to as "charge cleanoff". Spanning three orders of magnitude of exposed-area variation a consistent set of empirical scaling laws describes the substrate return current during the discharge; the total charge released is proportional to the sample area and the peak current is proportional to the sample radius [Balmain and Dubois, 1979; Flanagan et al, 1979]. The appearance of the discharge arcs suggests that the discharges start at the dielectric edges or seams and propagate across the surface [Stevens, 1980]. A second class of discharge, termed

"punchthrough", releases a smaller fraction of charge and is characterized by the appearance of a pinhole-sized puncture in the material. Subsequent discharges appear to originate in rapid succession from this site.

Past modelling of the laboratory simulations has concentrated on a one-dimensional description of the charging process [Beers et al, 1980; Purvis et al, 1977] which represents the charging process near the centre of the specimen. However, the tendency of the discharge to be associated with a well defined edge suggests that such a model cannot adequately describe the conditions of discharge initiation. In addition, data from the SCATHA satellite suggests that discharges can occur at differential voltages of only 3 kV [Stevens, 1980]. The resulting bulk field in the material calculated by a one-dimensional theory is not thought to be sufficient to cause the dielectric breakdown associated with such discharges. Investigators attempting to understand the discharge process have therefore been forced to examine the details of the internal charge distribution and to determine multi-dimensional effects which could influence the material's stability [Beers et al, 1981; Stevens, 1981].

This work represents an attempt to quantify the higher-dimensional effects present in the charging of planar dielectric films exposed to a mono-energetic electron beam. Regions of high charge concentration and intense electric fields are identified under a variety of charging conditions in order to isolate factors related to the discharge process.

The following two chapters (Chapter 2 and Chapter 3) are a review of the present state of the art in electron beam charging effects. New material is introduced in Chapter 4 and the following chapters.



## 2. ELECTRON BEAM CHARGING EFFECTS IN DIELECTRICS

### 2.1 Introduction

Electron beam effects begin with the interaction between an energetic incident electron (1 - 100 keV) and a target atom resulting in a transfer of energy. This energy can appear in a number of forms including excitation of the target atom, vibrational and rotational motion of the atom manifested as heat, and ionization of the atom. Some ionizing events transfer sufficient energy to create recoil electrons in the material. These can initiate further ionizing interactions resulting in an abundance of free electrons which can be moved under an applied field through the usual thermal activation process.

If the primary electron mean free path between collisions is too small then its range will not be sufficient to penetrate the material. These trapped electrons result in an accumulation of net charge and the development of large fields within the dielectric. The remainder of this section is devoted to listing some of the material responses which can influence the charge accumulation in the exposed material.

### 2.2 Secondary Emission and Backscatter

Any material exposed to an electron beam is found to emit electrons with a broad spectrum of energies, as illustrated in Fig. 2.1 [Harrower, 1957]. The distribution is distinctly bimodal for primary energies greater than 500 eV. Those electrons emitted with lower energy are referred to as the secondary emission component while those with higher energy are referred to as the backscatter component of the total emission. The relative magnitude and characteristic energies depend on the material and the energy of the primary electrons.

The high energy of the backscattered electrons is the result of near-

elastic collisions with the material. The backscatter spectrum has the primary energy as its maximum. This high energy nature implies that the scattering process could occur over an appreciable fraction of the primaries' range. The backscatter coefficient BS defined as the fraction of incident electrons emitted in the high energy tail of the emission spectrum, is usually found to decrease slowly with increasing energy. For most polymer dielectrics the following empirical relationship holds [Wall et al, 1977]

$$BS = 0.1(KE)^{-0.2} \quad (2.1)$$

where  $BS = J_{bs}/J_i$  = backscatter coefficient

KE = kinetic energy of primary electrons (keV)

The backscatter coefficient for primaries incident at an angle  $\theta$  with respect to the surface normal of most metals has been described as [Darlington, 1975]

$$BS(\theta) = B(BS(0)/B)^{\cos\theta} \quad (2.2)$$

where B = dimensionless material constant

$\theta$  = angle of incidence with respect to the surface normal

If we take B to be unity then this expression also fits the data for most polymers [Wall et al, 1977].

The secondary electrons are a direct manifestation of the ionization process in the material. The shape of the secondary emission energy spectrum is largely independent of the primaries' energy. The probability of a secondary electron escaping from a given volume of irradiated material is assumed to decrease exponentially with increasing distance from the material

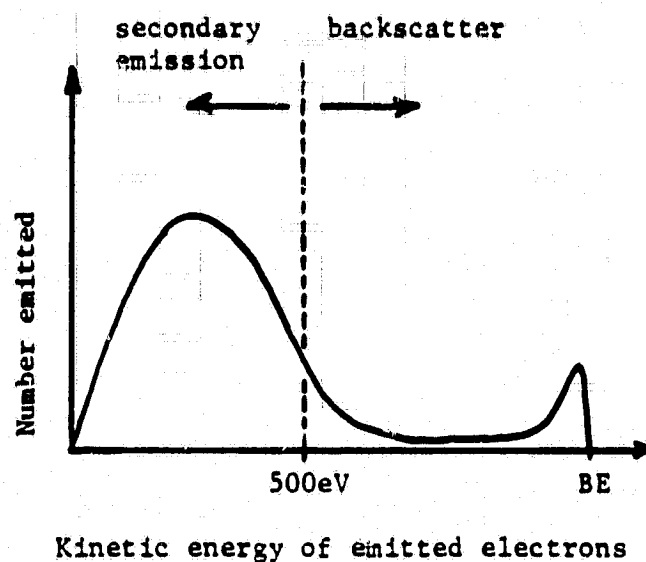


Fig. 2.1 Generalized emission spectrum.

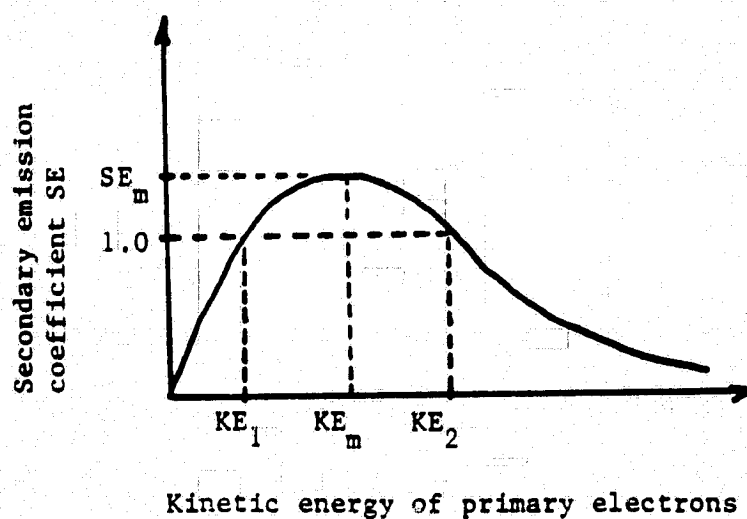


Fig. 2.2 Generalized secondary emission yield vs. primary energy.

surface. The decay constant for most polymers varies between 0.002 and 0.005  $\mu\text{m}$  [Budd, 1981].

The secondary emission coefficient SE, defined as the number of secondaries emitted per incident primary, is a strong function of the primaries' energy as indicated in Fig. 2.2. The energies where the coefficient is equal to unity,  $KE_1$  and  $KE_2$ , are known as the first and second crossover points. The mechanisms responsible for the maximum are a minimum ionization energy requirement and the increasing penetration of the primaries at higher energies. Burke [1980] has demonstrated that a universal curve can be generated relating the secondary emission coefficient and the primaries' energy for most inorganic insulators. At high energies the secondary emission coefficient is given by a simple power law relationship

$$SE = K(KE)^{-0.725}$$

where  $KE$  = primaries' energy (keV)

The constant  $K$  is found to decrease as the complexity of the repeating unit in the polymer increases. Quantitatively this can be expressed in terms of the gram molecular weight  $M$  and the number of valence electrons in the repeating unit  $N$  (1,4,5,6 for H,C,N,O respectively). Polymers containing just these elements are governed by the following relationships [Burke, 1980]:

emission coefficient	$K = 10.64(N/M) - 3.15$	(2.3)
----------------------	-------------------------	-------

energy at maximum yield	$KE_m = (K/12.09)^{0.58}$	(2.4)
-------------------------	---------------------------	-------

maximum yield	$SE_m = 9.5 KE_m$	(2.5)
---------------	-------------------	-------

secondary emission	$SE = SE_m \left[ \frac{(1 - \exp(-Z^{1.725}))^{1.526}}{Z^{0.725}} \right]$	(2.6)
--------------------	---	-------

where  $Z = 1.284 KE/KE_m$

POLYMER	FORMULA	K	KE <sub>m</sub>
Teflon	CF <sub>2</sub>	1.546	0.303
Polyethylene	CH <sub>2</sub>	1.370	0.283
Polyvinylalcohol	C <sub>2</sub> H <sub>4</sub> O	1.242	0.267
Nylon	C <sub>6</sub> H <sub>11</sub> ON	1.148	0.255
Lucite	C <sub>5</sub> H <sub>8</sub> O	1.115	0.251
Polystyrene	C <sub>8</sub> H <sub>8</sub>	0.907	0.223
Mylar	C <sub>10</sub> H <sub>8</sub> O <sub>4</sub>	0.847	0.214
Kapton	C <sub>22</sub> H <sub>10</sub> O <sub>5</sub> N <sub>2</sub>	0.682	0.189

Table 2.1 Emission coefficient K (from Burke [1980])

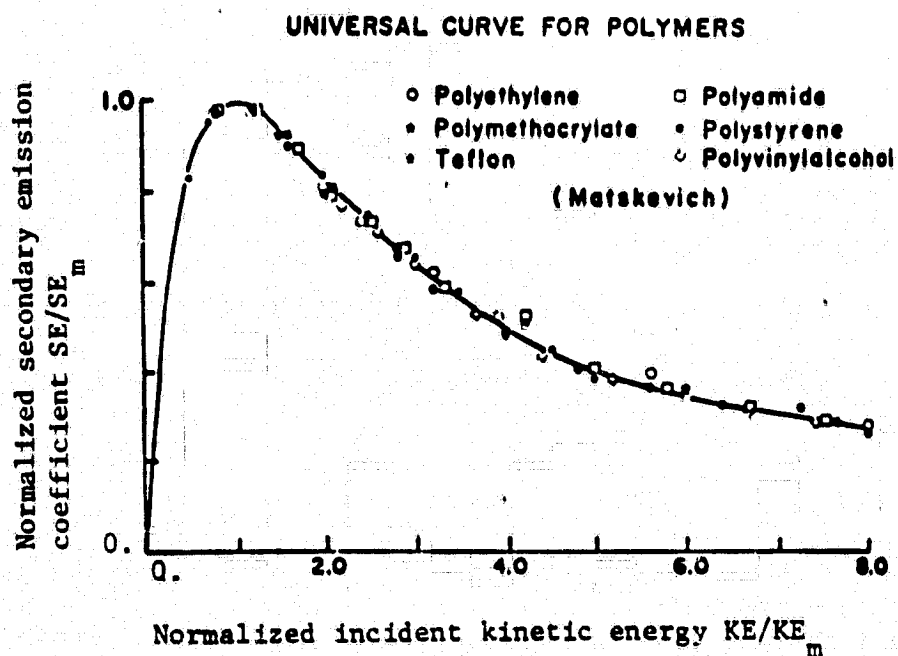


Fig. 2.3 Experimental results and eq. 2.6 (from Burke [1980]).

For KE greater than  $1.5 KE_m$  the following approximation represents an over-estimate of less than 5%

$$SE \approx K KE^{-0.725} \quad (2.7)$$

Values of K for a large number of polymers are presented in Table 2.1. In Fig. 2.3 the universal emission curve, represented by eq. 2.6, is presented.

Robinson and Budd [1980] have fitted measurements of total emission from Teflon for large primary energies to a single power law term

$$BS + SE = (KE_2/KE)^{0.58} \quad (2.8)$$

where  $KE_2$  is the second unity crossover energy  
( $KE_2 \approx 2.1$  keV for Teflon)

This figure is slightly larger than that suggested by Burke (eqs. 2.1 and 2.7) though both predict the same second crossover energy. Budd [1981] has also reported measurements of the total emission dependence on the beam angle of incidence. For  $\theta$  less than  $50^\circ$  it was found to vary as  $1/\cos\theta$  as would be consistent with the number of secondaries being proportional to the deposition of energy in a fixed-thickness surface layer. Wall et al [1977] suggest an alternative semi-empirical relationship which can be compared to Robinson's formulation:

$$\text{Wall et al} \quad SE(\theta) = SE(0) \exp(2(1 - \cos\theta)) \quad (2.9)$$

$$\text{Robinson} \quad SE(\theta) = SE(0)/\cos\theta \quad (2.10)$$

For angles in the interval  $0^\circ - 78^\circ$  the functional form suggested by Robinson produces a smaller emission yield.

Surface contamination and surface roughness can also influence secondary

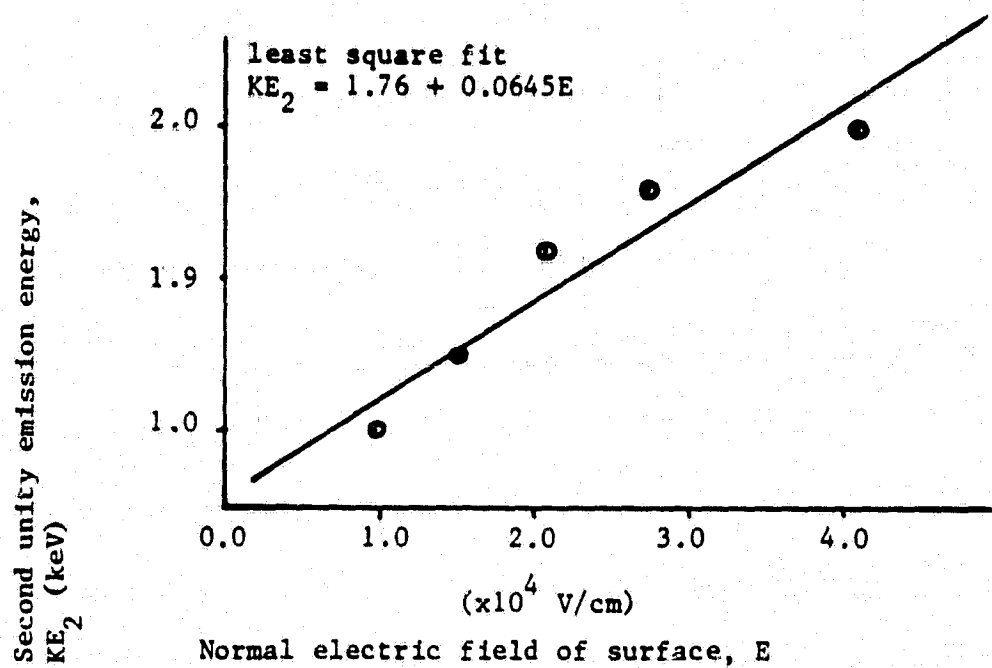


Fig. 2.4 Dependence of unity crossover energy on normal surface field strength for Teflon (from Robinson and Budd [1980]).

emission [Budd, 1981; Davies, 1979]. The possibility of a surface electric field dependence also exists due to the relatively low energies of the freed secondaries. Robinson and Budd [1980] have made measurements indicating that the second unity crossover point is a weak function of the normal surface field when accelerating the secondaries away from the surface (see Fig. 2.4). Robinson and Nguyen [1979] have also speculated that surface tangential fields may enhance secondary emission. Balmain [1978] and Feder [1976] have used the enhancement of secondary emission due to charge storage in a material to image the charge deposited in a dielectric with a scanning electron microscope. No quantitative data concerning these effects have been found in the literature.

### 2.3 Electron Range

An electron, due to its low mass, is prone to large changes in its momentum in any interaction. The statistical nature of these deflections results in a very broad deposition profile known as range straggling. The number of electrons penetrating to a particular depth in a material does not drop sharply at the mean range as is the case of heavier particles. Instead the loss is gradual as shown in Fig. 2.5.

Various measures of electron penetration have been used including mean or average range, extrapolated or practical range and linear range. The mean range refers to the distance at which 50% of the incident electrons have been absorbed. The extrapolated range is obtained by projecting the slope of the fraction penetrating versus distance curve to a zero crossing as indicated in Fig. 2.5.

The linear range is a calculated quantity based on a formulation of the energy loss per unit distance of penetration. The most common approach used



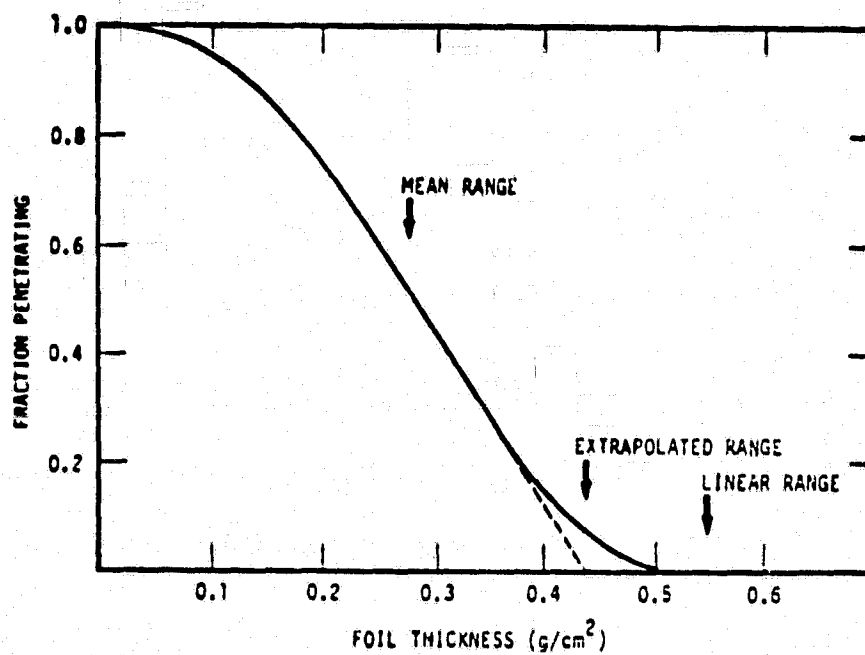


Fig. 2.5 Penetration of 1 MeV electrons through aluminum foils (from Marshall and Ward [1937]).

in this calculation is to assume a continuously slowing down approximation (CSDA range) where the energy loss per unit distance is a constant equal to the mean rate of energy loss. The linear range is a measure of the length of a possible electron path which can be deflected far from the projected incident trajectory and is therefore usually 25 - 50% larger than the extrapolated range. For Teflon the average range is found to be about 60% of the extrapolated range [Gross et al, 1974].

At primary energies less than 50 keV a reasonable representation of the extrapolated range is given by the Gledhill relation [Gross, 1980]:

$$\log r_{\text{ex}} = -5.1 + 1.358 \log KE + 0.215(\log KE)^2 - 0.043(\log KE)^3 \quad (2.11)$$

where  $r_{\text{ex}}$  = extrapolated range  $\times$  material density (gm/cm<sup>2</sup>)

KE = primary energy (keV)

From eq. 2.11 for energies less than 10 keV

$$\begin{aligned} r_{\text{avg}} &\approx 0.6 r_{\text{ex}} \\ &\approx 4.8 \times 10^{-6} (KE)^{1.358} \quad (\text{gm/cm}^2) \end{aligned} \quad (2.12)$$

The electron deposition profile has been calculated using Monte Carlo simulations [Beers et al, 1979; Frederickson, 1979; Berkley, 1979] although the necessary penetration-energy loss mechanisms for very low energy electrons are not well established [Beers et al, 1980]. Typical deposition profiles for various primary energies are given in Fig. 2.7 as calculated by these codes.

## 2.4 Dose Rate

The dose is defined as the mean energy imparted by ionizing radiation to the material in a volume element divided by the mass in that volume.

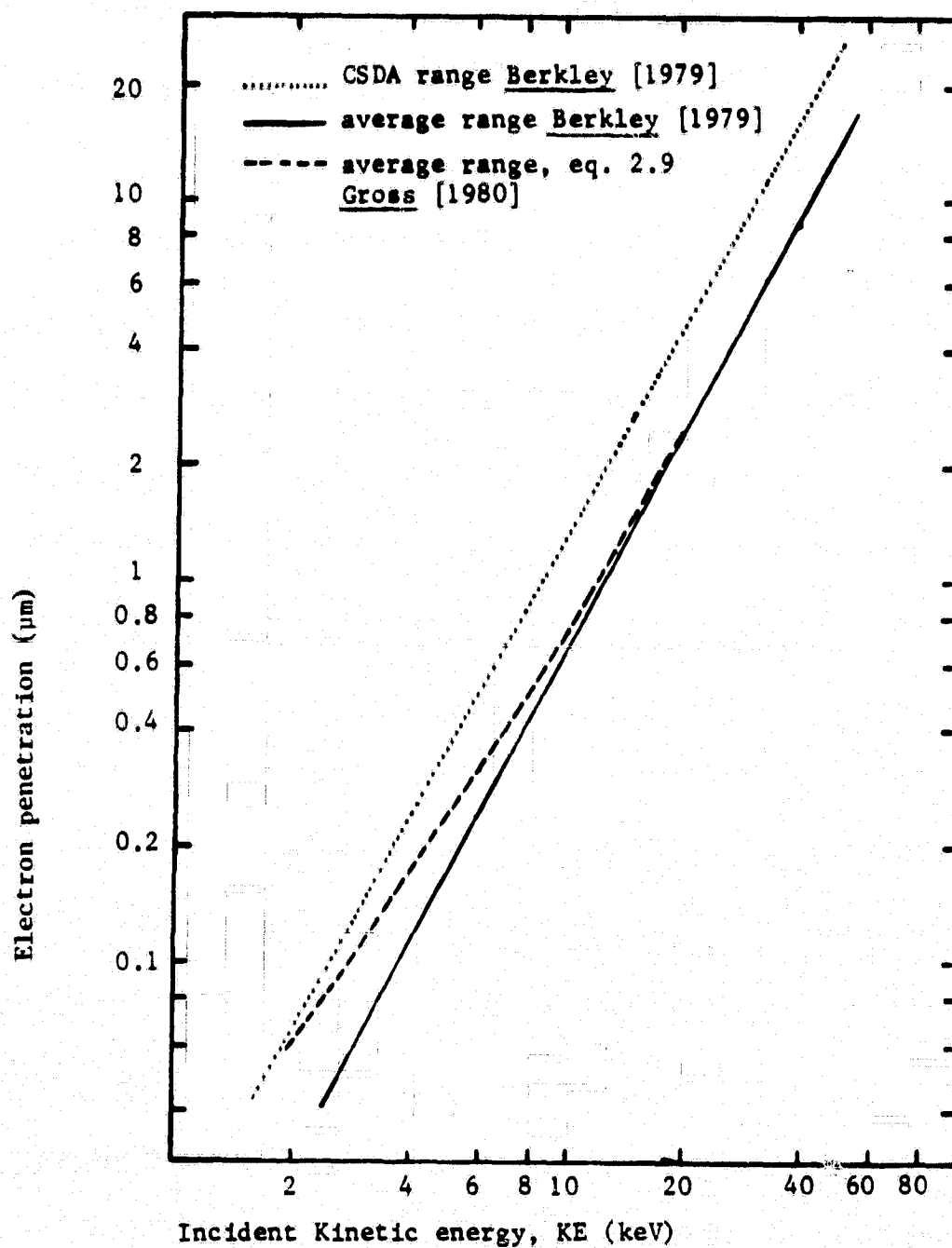


Fig. 2.6 Range - energy relationships for electrons in Teflon.

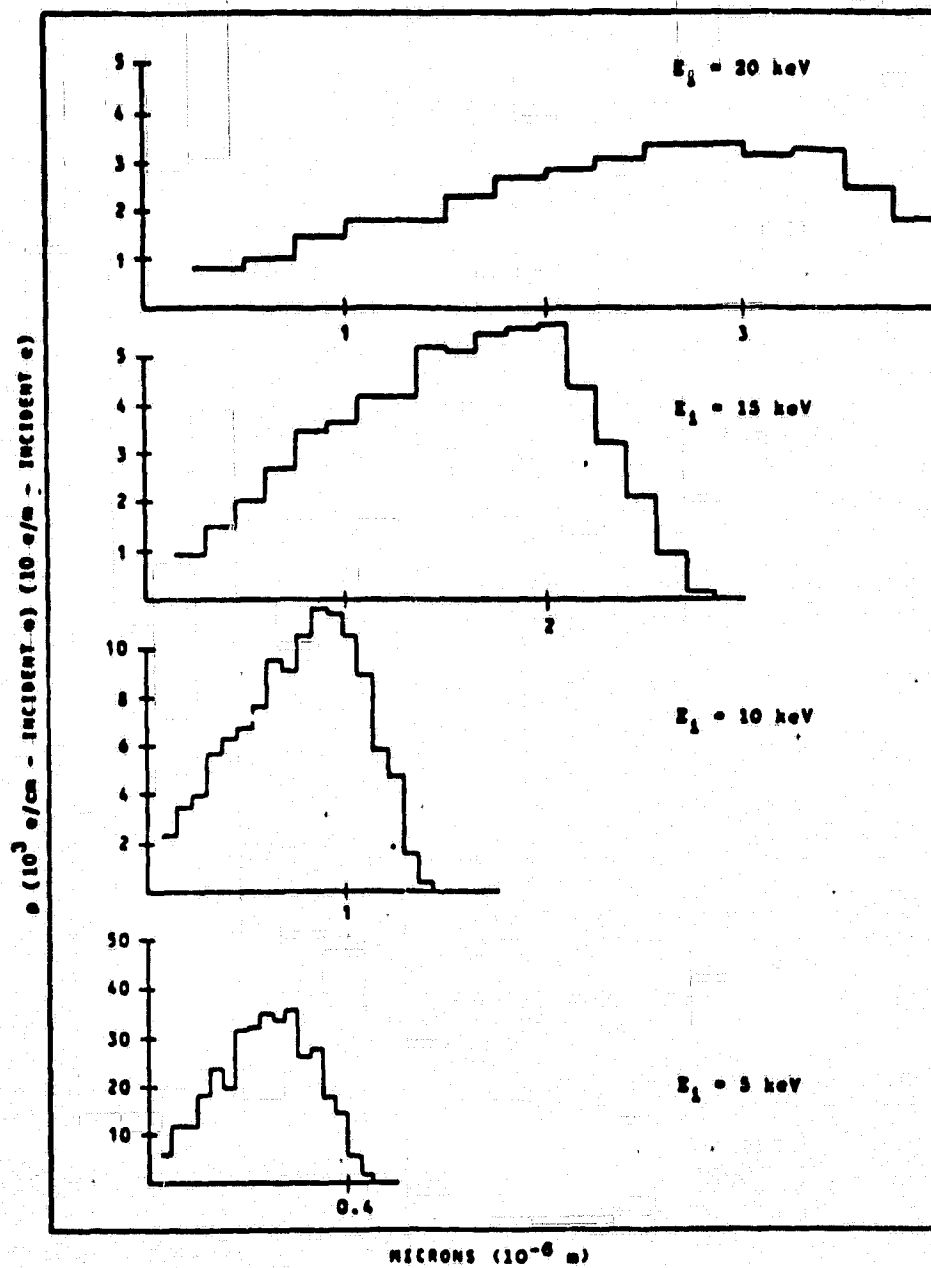


Fig. 2.7 CHARGE DEPOSITION PROFILE IN TEFLON  
FOR NORMALLY INCIDENT ELECTRONS  
(from Beers et al [1977]).

We shall adopt as a measure of dose the "rad" ( $1 \text{ rad} = 10^{-2} \text{ Joules/kg}$ ). The average absorbed dose rate for non-penetrating, normally incident electron beam is [Gross, 1980]:

$$\text{dose rate} = \dot{D} = I_1 KE \times 10^8 / (a \bar{r} \delta) \quad (\text{rads/sec}) \quad (2.13)$$

where  $D$  = dose (rads)

$I_1$  = incident current measured to the material surface  $a$  (A)

$KE$  = primary electron energy (keV)

$a$  = surface area ( $\text{cm}^2$ )

$\bar{r}$  = average range (cm)

$\delta$  = material density ( $\text{gm/cm}^3$ )

Assuming a constant current to the surface eq. 2.13 can be modified for non-normal incidence by dividing by the new irradiated volume  $a \bar{r} \cos \theta$ , instead of  $a \bar{r}$ :

$$\dot{D}(\theta) = \dot{D}(0) / \cos \theta \quad (2.14)$$

If the range-energy (eq. 2.12) and the dose-energy (eq. 2.13) relations are combined we find that the mean dose rate decreases as the energy of the primaries increases.

Details of the actual deposition profile can again only be calculated using Monte Carlo techniques [Beers et al, 1979; Frederickson, 1979]. Typical curves show a broad maximum near the mean range due to beam straggling.

## 2.5 Conductivity

The conductivity  $g$  of most polymers under low electric fields, in the dark and at room temperature is very small making it often difficult to establish accurately. For Teflon FEP the estimates vary considerably:

$< 10^{-22} (\Omega\text{cm})^{-1}$	[ <u>Sessler</u> , 1974]
$3.3 \times 10^{-18} (\Omega\text{cm})^{-1}$	[ <u>Beers et al</u> , 1979]
$10^{-20} (\Omega\text{cm})^{-1}$	[ <u>Kinney</u> , 1957]
$10^{-20} - 10^{-17} (\Omega\text{cm})^{-1}$	[ <u>Frederickson</u> , 1979]

For Kapton H there has been less work published although a figure between  $10^{-18}$  and  $10^{-17} (\Omega\text{cm})^{-1}$  has been established from a series of measurements made by Adamo and Nanevicz [1977]. In general it has been observed that Teflon is a better insulator than Kapton by about two orders of magnitude.

#### 2.5.1 Conductivity: Temperature Dependence

The conductivity of most insulators displays a temperature dependence that can be described by the following empirical expression [Wall et al, 1977]:

$$\sigma_0 = A \exp(-W/kT) \quad (2.15)$$

where  $T$  = absolute temperature  $\geq 300^\circ\text{K}$

$A, W$  = material constants

In the limit of zero applied fields Hanscombe and Calderwood [1973] found  $W$  to be 1.55 eV for Kapton. Amborski [1963] found  $W$  to be about 1.0 eV for Kapton under a field strength of  $5 \times 10^4$  V/cm. Using data from Adamo and Nanevicz [1977] we find  $W = 0.77$  eV for Teflon FEP under fields of  $10^5$  V/cm.

Under normal spacecraft operating conditions temperature ranges can be expected from  $0^\circ\text{C}$  to  $120^\circ\text{C}$  [Rosato, 1968; Streed and Arvensen, 1967]. Using  $W$  equal to 1.0 eV we find that over this temperature range the magnitude of the dark conductivity could increase by a factor of  $5 \times 10^5$ .

#### 2.5.2 Conductivity: Photoconductivity

The effect of light on the conductivity of a variety of materials

has been reported briefly by Adamo and Nanevich [1977]. The most sensitive material listed is Kapton which when illuminated by a Xenon lamp at an intensity of one sun displayed an increase of up to 4 orders of magnitude in conductivity. There was no attempt to isolate temperature effects or spectral response. No further work has been found in the literature.

### 2.5.3 Conductivity: Field Dependence

The conductivity of most polymers is a non-linear function of applied electric field. In particular there exists a range of high fields where it increases as  $\exp(E^{1/2})$ . A functional form describing this behaviour is [Adamec and Calderwood, 1975]

$$g/g_0 = \left( \frac{2 + \cosh(aE^{1/2}/T)}{3} \right) \left( \frac{T}{bE} \sinh(bE/T) \right) \quad (2.16)$$

where  $a, b$  = material constants

$T$  = absolute temperature ( $^{\circ}\text{K}$ )

$E$  = applied electric field

For fields less than  $10^6$  V/cm the second term in eq. 2.16 is near unity. The value of  $a/T$  at  $22^{\circ}\text{C}$  was found to be  $4.68 \times 10^{-3}$  (cm/V) $^{1/2}$  and  $4.03 \times 10^{-3}$  (cm/V) for Kapton and Teflon respectively as indicated in Figs. 2.9 and 2.10.

### 2.5.4 Conductivity: Radiation-Induced Conductivity

The charge carriers generated by the ionizing radiation give rise to an enhanced conductivity. A power law relationship between the equilibrium radiation-induced conductivity and the dose rate has the following form

$$g_{ric} = G(\dot{D})^{\Delta} \quad (2.17)$$

where  $\Delta, G$  = material constants

$$0.5 \leq \Delta \leq 1.0$$

$\dot{D}$  = dose rate

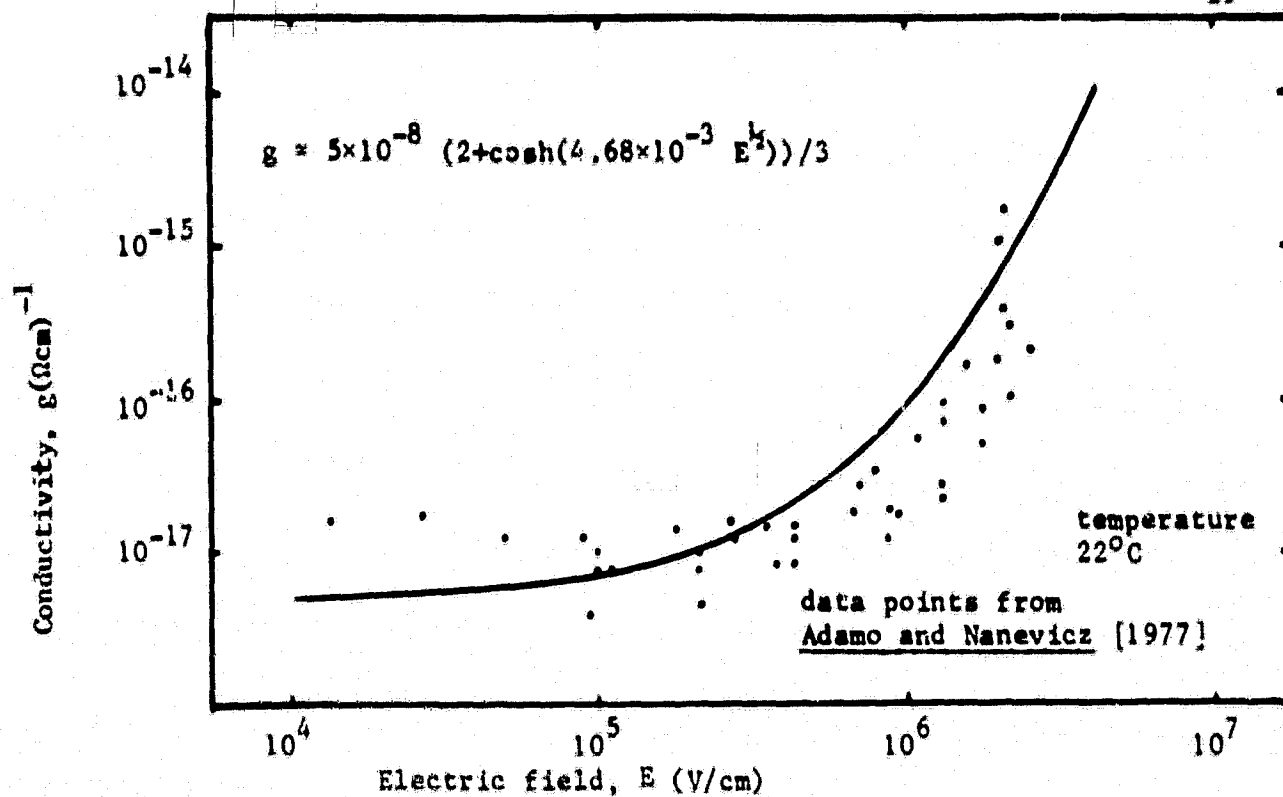


Fig. 2.8 Field induced conductivity in Kapton.

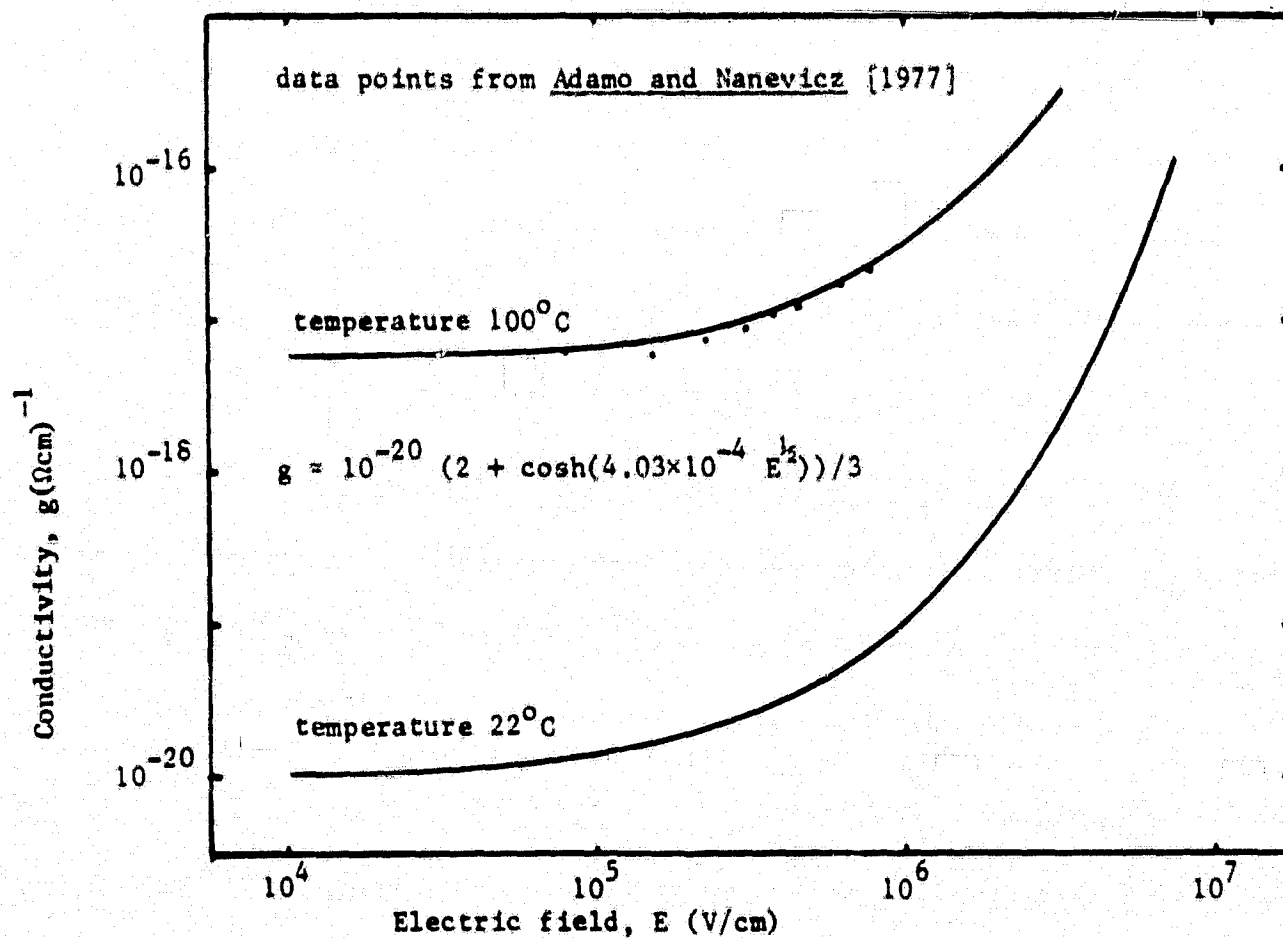


Fig. 2.9 Field induced conductivity in Teflon.



The value of  $\Delta$  is determined by the energy distribution of traps in the material; a uniform distribution gives  $\Delta$  equal to 1.0, while a single trap level gives  $\Delta$  equal to 0.5 [Gross, 1980]. It is often assumed that the radiation induced conductivity is proportional to the dose rate ( $\Delta = 1$ ) [Beers, 1979; Wall et al, 1977]. Table 2.2 lists the range of values found in the literature for  $G$  based on this assumption.

Gross et al [1974] report that measurements made at low dose rates tend to yield lower values of  $\Delta$  than those made at high rates. Data in Fig. 2.11 produce a power law fit for Teflon FEP at an average dose rate of  $2 \times 10^4$  rad/sec;  $\Delta = 0.7$ ,  $G = 1.7 \times 10^{-16} (\Omega\text{cm})^{-1}$ . In Fig. 2.12 this is plotted together with the upper and lower limits suggested by Table 2.2. The choice of  $\Delta = 0.7$  seems to fit the bounds quite well over the dose rate interval of interest. Fitting a similar curve for Kapton we find  $\Delta = 0.7$ ,  $G = 1.7 \times 10^{-17} (\Omega\text{cm})^{-1}$ .

A delayed component of radiation induced conductivity persists after the radiation has been removed for a period of seconds due to the finite lifetime of the free charge carriers. A functional form suggested by Gross [1980] is:

$$g_{\text{ric}} = g'/(1 + bt) \quad (2.18)$$

where  $g' = 1/3$  of the radiation induced conductivity at the end of irradiation

$t =$  time after end of irradiation (sec)

$b =$  constant approximately unity (sec) $^{-1}$   
[Beers et al, 1980]

The net conductivity of the sample is calculated as the sum of the radiation induced and dark conductivities.

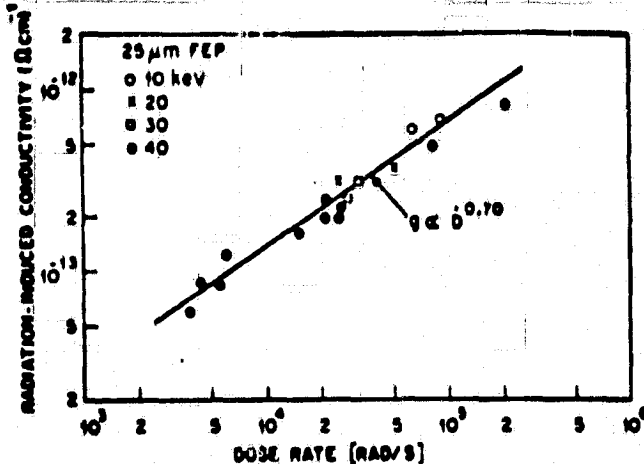


Fig. 2.10 Radiation-induced steady-state conductivity as a function of dose rate, determined from time constants of radiation-induced discharge currents, from Gross [1980]).

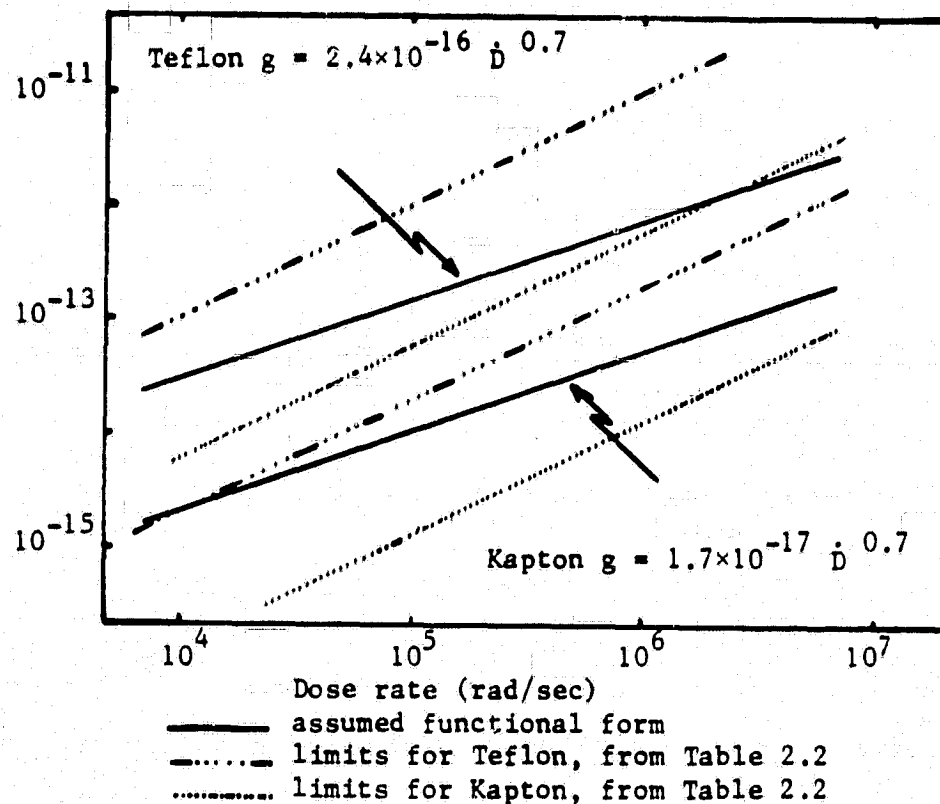


Fig. 2.11 Functional form of radiation induced conductivity.

Material	$G_{\max}$ sec/(Ωcm rad)	$G_{\min}$ sec/(Ωcm rad)
Kapton	$6.0 \times 10^{-18}$	$1.2 \times 10^{-19}$
Teflon	$1.0 \times 10^{-16}$	$2.8 \times 10^{-18}$
Mylar	$2.1 \times 10^{-19}$	$1.8 \times 10^{-19}$
Polyethylene	$4.5 \times 10^{-18}$	$3.0 \times 10^{-19}$
Polystyrene	$1.0 \times 10^{-16}$	$2.0 \times 10^{-18}$

Table 2.2 Upper and lower limits of  $G$ . Assumed functional form  $g = G\dot{D}$  (from Wall et al [1977]).

## 2.6 Optical Effects of Irradiation

Irradiation by an electron beam of sufficient energy can cause any of the following optical effects [van Lint et al, 1980]:

- luminescence
- Cerenkov radiation
- introduction and/or bleaching of optical bands
- changes in optical scattering
- changes in the index of refraction

Luminescence for the energy range of interest is easily detected for most of the materials under study here. The other effects are small except at very large doses or high energies.

## 2.7 Radiation Chemistry

The subject of radiation chemistry is too broad to be treated in detail at this level. For a more detailed discussion the reader is referred to the literature [Ausloos, 1968]. In polymers ionizing radiation produces free radicals that can effect chemical changes falling under two classifications; cross-linking and scission. Cross-linking refers to the formation of bonds between adjacent polymer chains. Scission refers to the breaking of a chain.

Frederickson [1979] claims that Teflon starts to degrade when the accumulated dose exceeds  $10^6$  rads, while other dielectrics require more than  $10^8$  rads. Wall et al [1977] suggest that variations in the reported values for the radiation induced conductivity constant  $G$  may be caused by radiation damage. Gross et al [1974a] report that large doses of the order of  $50 \times 10^6$  rads can cause a reduction in  $G$  by at least an order of magnitude. A  $10^6$  rad dose can be delivered to a  $0.1 \mu\text{m}$  deep layer by a 2 keV electron beam when the current density - time product is  $65 \text{ nC/cm}^2$ . A  $10 \text{ nA/cm}^2$  beam can therefore deliver such a dose in 6.5 sec.

## 2.8 Electrical Breakdown and Surface Discharge

Electron irradiation of insulators can produce an accumulation of charge sufficient to cause dielectric breakdown which is accompanied by the removal of a large fraction of the stored charge. The first published description by Gross [1957] indicated that the discharge was localized at a depth roughly equal to the mean range of the primary electrons. Further experimental work has evolved to help quantify the discharge process: Balmain and Hirt, 1980; Balmain and Dubois, 1979; Balmain, 1978; Purvis et al, 1977; Roche and Purvis, 1979; Yadlowsky et al, 1980; Aron and Staskus, 1979; Stevens, 1980; Bosma and Levadou, 1979. The actual discharge mechanism, however, remains largely unexplained. There is evidence that defects in the material may play a large role in the breakdown process [Davies, 1977].

The breakdown threshold of most dielectrics has been found in the range  $1 \times 10^6 - 5 \times 10^6$  V/cm [Beers et al, 1979; Davies, 1977; Frederickson, 1979]. Reports also suggest a close association of the discharge with the edge of the exposed material [Beers et al, 1980; Stevens et al, 1978; Balmain, 1978; Robinson, 1977]. Stevens [1980] concludes that the data collected from the SCATHA satellite indicate breakdowns in orbit are occurring despite the comparatively low (2 - 4 keV) differential voltages that have been observed, implying that the surface potential may not be the deciding factor in the initiation of the discharge event, in turn prompting questions about the internal charge distribution and multi-dimensional effects.

### 3. ONE-DIMENSIONAL MODELLING

A one-dimensional study of the charge build up on planar dielectrics exposed to a uniform monoenergetic electron beam has the advantage of simplicity over a multi-dimensional treatment. Such models can be used to check parameter sensitivity, to determine main factors governing the charging process, and to serve as a standard to which the results of more complex analyses can be compared.

The analysis can be separated into an external and an internal charging model. The external model is concerned with the net accumulation of charge in the material and deals with the measurable quantities of surface potential and total charge. The internal model is concerned with the distribution of charge within the material and the resultant internal electric fields. The work in this chapter follows that outlined by Beers et al [1979].

#### 3.1 External Model Development

The net accumulation of charge on a planar dielectric exposed to a uniform mono-energetic electron beam closely resembles the charging of a simple resistor-capacitor network. The resistive elements represents the mechanisms of charge loss from the surface and the capacitive element corresponds to the physical geometry shown in Fig. 3.1. To determine the capacitance per unit area we assume that the structures are infinite in a x-z plane thus obtaining a one-dimensional differential equation derived from Gauss' Law describing the relationship between the electric field and the volume charge density

$$\partial E_y / \partial y = -q(y) / \epsilon \quad (3.1)$$

where  $E_y$  is the electric field normal to the surface

$q$  is the electron volume charge density  
(C/m<sup>3</sup>, positive for electrons)

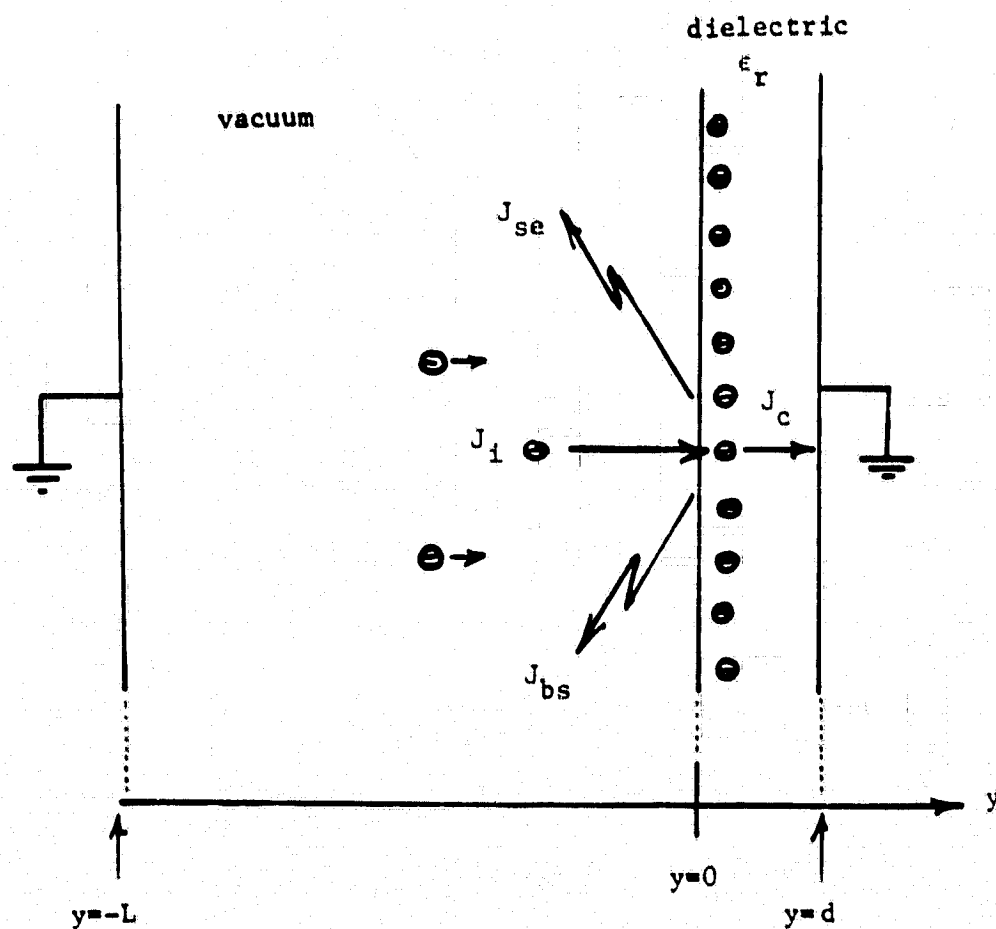


Fig. 3.1 External charging model geometry.

note; since the electron is the principal charge carrier the currents and charge densities will be referenced to the movement or accumulation of negative charge, to conform with the major part of the relevant literature.

We shall assume that the space charge density due to the beam current is negligible. Thus in the interval  $(-L, 0^-)$  the electric field is constant. The grounding of the plates at  $y = -L$  and  $y = d$  imposes the following constraints on the electric field.

$$\int_{-L}^d E(y) dy = 0$$

or

$$\int_0^d E(y) dy = -E_0 L \quad (3.2)$$

where  $E_0$  = magnitude of the electric field for  $-L < y < 0^-$

From eq. 3.1 we find

$$E(s) - E(0^+) = - \int_0^s q(y) / \epsilon_0 \epsilon_r dy, \quad s > 0^+$$

$$\int_0^d E(s) ds - E(0^+) d = - \int_0^d ds \int_0^s q(y) / \epsilon_0 \epsilon_r dy \quad (3.3)$$

$$-E_0 L - E(0^+) d = - \int_0^d ds \int_0^s q(y) / \epsilon_0 \epsilon_r dy$$

Using the condition of continuity for the normal component of the displacement density we find  $E(0^+) = E_0 / \epsilon_r$ . Integrating the right hand side of eq. 3.3 by parts we find

$$\rho = -V \frac{(1 + d/(L\epsilon_r)) \epsilon_0 \epsilon_r}{(d - \bar{y})} \quad (3.4)$$

where  $V = \int_0^d E(y)dy$  the potential at the dielectric surface

$\rho = \int_0^d q(y)dy$  effective charge per unit area

$\bar{y} = \int_0^d yq(y)dy/\rho$  the charge centroid

For thick samples where  $d \gg \bar{y}$  the external variables (voltage and charge density) are largely independent of the internal charge distribution. The range-energy relationship illustrated in Fig. 2.6 suggests that unless considerable low energy excess charge transport occurs after deposition the approximation that  $d \gg \bar{y}$  will be valid for samples thicker than 25  $\mu\text{m}$  and beam energies less than 20 keV. If we also assume that the surface capacitance to the ground at  $y = -L$  is negligible compared to the capacitance to the ground at  $y = d$  then eq. 3.4 reduces to

$$\rho = -V C \quad (3.5)$$

where  $C = \epsilon_0 \epsilon_r / d$  the capacitance per unit area

Restricting the possible charge transfer mechanisms to the incident beam, conduction current, secondary emission and backscatter we find:

$$\rho = \int J_{\text{net}} dt \quad (3.6)$$

where

$$J_{\text{net}} = J_i - J_{\text{bs}} - J_{\text{se}} - J_c \quad (3.7)$$

$J_i$  = incident beam current density

$J_{\text{bs}}$  = backscatter current density

$J_{\text{se}}$  = secondary emission current density

$J_c$  = conduction current density



Combining eqs. 3.6 and 3.5

$$\int_{V_0}^V dV/J_{\text{net}}(V) = -(t - t_0)/C \quad (3.8)$$

Equation 3.8 corresponds to that previously used by both Purvis et al [1977] and Beers et al [1979] to describe the net charge accumulation in the dielectric.

It is implied in eq. 3.8 that the net current density is a function of the surface voltage. This voltage dependence is due in part to the secondary emission and backscatter currents which tend to increase with decreasing primary kinetic energy. The decrease in the impact energy is directly related to the potential barrier, i.e. surface potential, that must be overcome to reach the surface. By performing an energy balance we find:

$$KE + |eV| = BE \quad (3.9)$$

where KE = electron kinetic energy at impact

V = surface potential

e = charge on an electron

BE = the total beam energy (a constant)

In general the net current density is a non-linear function of the surface potential and numerical integration must be used to solve eq. 3.8.

The model does not incorporate the following effects:

- surface conductivity
- radiation hardening of the secondary emission coefficient
- field dependence of the secondary emission coefficient
- temperature effects
- photoconductivity
- photoemission
- material degradation

Any of the above could be incorporated once a reasonable data base had been established. The development of eq. 3.8 involved several assumptions which are inherent in this discussion. These include:

- no multidimensional effects
- no spacecharge effects due to current densities
- quasi-static potential (potential does not appreciably change during electron transit time)
- thick-film, short range approximation

Two materials, Teflon and Kapton, will be studied in detail. Teflon has a relative permittivity of approximately 2.25 and a density of 2.2 gm/cm<sup>3</sup> permittivity whereas Kapton has a relative permittivity of approximately 3.6 and a density permittivity of 1.42 gm/cm<sup>3</sup> [Beers et al, 1980]. The expressions for the backscatter and secondary emission coefficients will be chosen to agree with those proposed by Burke [1980] and Wall et al [1977] (i.e. eqs. 2.1, 2.2, 2.7 and 2.9).

### 3.2 External Model Results

#### 3.2.1 Steady State Surface Potential

A steady state is achieved by reducing the net current to the surface to zero, suggesting from eq. 3.7 that

$$J_i = J_{bs} + J_{se} + J_c$$

or equivalently

$$J_i(1 - BS - SE) = J_c \quad (3.10)$$

For a normally incident beam, eqs. 2.1 and 2.7 can be substituted for BS and SE using eq. 3.9 to express the kinetic energy at the surface in terms of the surface potential and the beam energy. Assuming the steady state kinetic energy is greater than 1.5 KE<sub>m</sub> (a necessary condition for eq. 2.7 to be valid) we obtain:

$$J_i(1 - 0.1(BE - |eV|)^{-0.2} - K(BE - |eV|)^{-0.725}) = |V|/d \cdot g(V/d) \quad (3.11)$$

where  $g$  = material-dependent conductivity

$K$  = material constant

0.68 keV for Kapton

1.55 keV for Teflon

$V$  = surface potential (kV)

The bulk conductivity of Teflon is assumed to be a constant  $g_0$  in order to simplify the following analysis. We shall relax this constraint allowing a field-dependent conductivity for the analysis of Kapton.

The solution of eq. 3.11 for Teflon is presented in Fig. 3.2. Two distinct regions exist depending on the ratio of conduction current to beam current. If the beam current dominates then the steady state surface potential will be proportional to the difference between the beam energy and the second unity crossover energy for total emission (BS + SE). If the currents are comparable, as is the case for low beam currents, the surface potential is proportional to the beam current. The asymptotic behaviour is given by:

$$\text{if } J_1/J_c = 1, |V| = J_1 d / g_0 (1 - SE - BS) \text{ evaluated for } KE = BE \quad (3.12)$$

$$\text{if } J_1/J_c \gg 1, |V| = (BE - KE_2) / |e| \quad (3.13)$$

where  $KE_2$  = second unity crossover energy for  
total emission  
0.69 keV for Kapton  
2.10 keV for Teflon

The critical value of  $J_1 d / g_0$  separating the conduction-limited and emission-limited regions is obtained by equating eqs. 3.12 and 3.13. For Teflon we find:

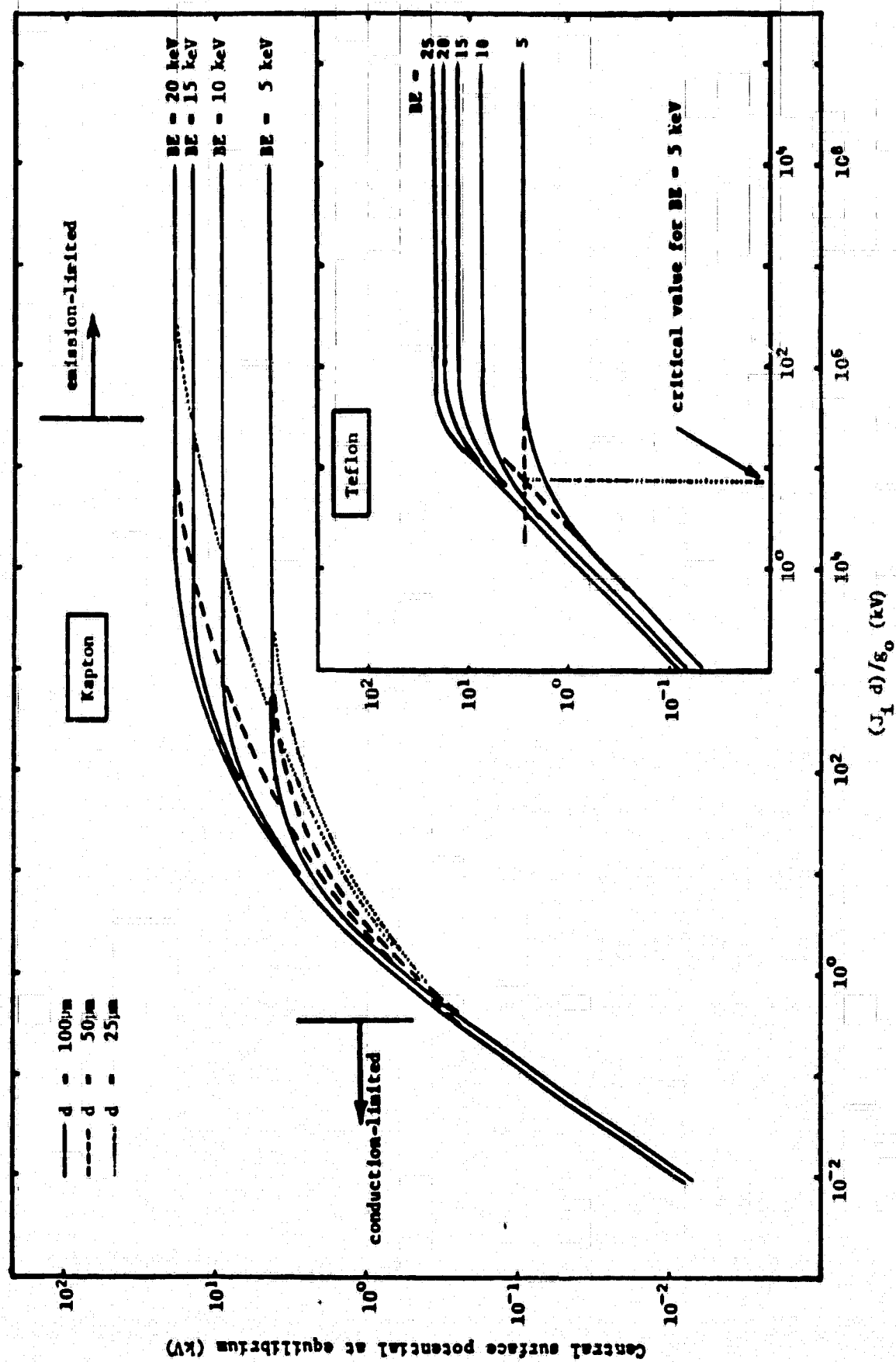
$$(J_1 d / g_0)_{\text{critical}} = \frac{(BE - 2.1) / |e|}{(1 - 1.55BE^{-0.725} - 0.1BE^{-0.2})} \quad (3.14)$$

where BE = beam energy (keV)

Using the total emission coefficient of eq. 2.8 suggested by Robinson and Budd [1980] results in a slight downward shift in the conductivity-limited region of the curves.

The introduction of a field dependent conductivity as suggested by eq.

Fig. 3.2 Equilibrium surface potential as a function of the charging parameters  $J_1$ ,  $d$ ,  $\epsilon_0$ , BE.



2.16 for Kapton does not affect the asymptotic analysis previously discussed. The transition between these regions however, is much expanded as indicated in Fig. 3.2 for Kapton. The effect is most significant for high beam energies and thin samples.

Interpreting Fig. 3.2, we find that for typical spacecraft charging parameters (material thickness 25  $\mu\text{m}$ , bulk conductivity  $10^{-18} (\Omega\text{cm})^{-1}$ ) the critical current density for Teflon is 0.013 nA/cm<sup>2</sup>. For densities greater than this the equilibrium surface voltage and charge will be practically independent of the beam current. Balmain and Hirt [1980] have found that the total charge released from Teflon during a discharge event displays this same independence for typical charging conditions (current density 0.4 - 100 nA/cm<sup>2</sup>, beam energy 20 keV, material thickness 30  $\mu\text{m}$ ) as would be expected if the specimen is emission-limited. Balmain and Dubois [1979] have also found that the total charge released is proportional to the area irradiated (see Fig. 3.3). Figure 3.3 indicates that approximately 25% of the net available charge at equilibrium in Teflon is released per discharge. For Kapton with a beam current density of 80 nA/cm<sup>2</sup>, the charge released is reduced to 10%.

In Fig. 3.4 the equilibrium surface potential for Kapton has been graphed in the transition region (assuming  $g_0 = 5 \times 10^{-18}$  as suggested in Fig. 2.9 and a beam energy = 20 keV). The span of current densities, 0.1 - 100.0 nA/cm<sup>2</sup>, covers the typical range employed in laboratory simulations. A discharge dependence on the incident current density is therefore expected and indeed Balmain and Hirt [1980] have reported a total released charge dependence of  $J_1^{0.23}$  as indicated in Fig. 3.5. The total available charge, under similar charging conditions as indicated in Fig. 3.4 has a current density dependence of  $J_1^{0.22}$ .

### 3.2.2 Charging Dynamics

The development of the stored charge is governed by the current

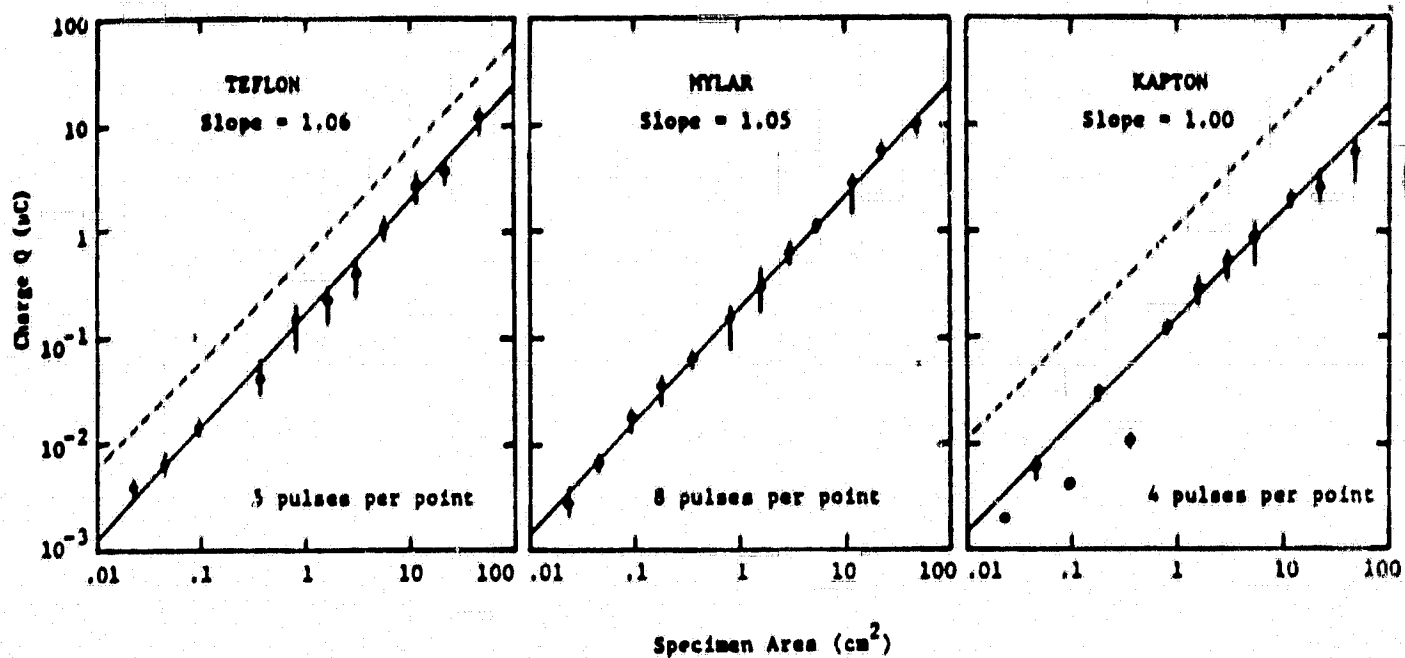
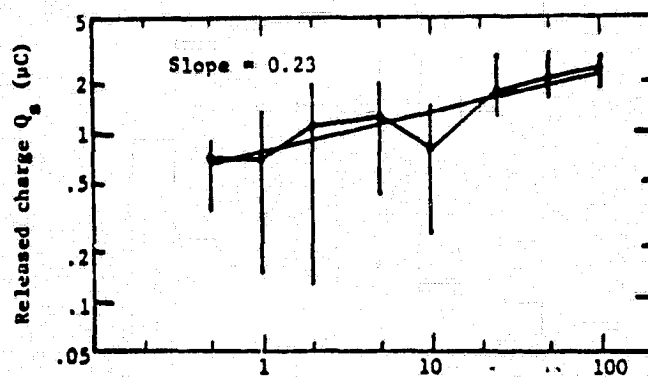
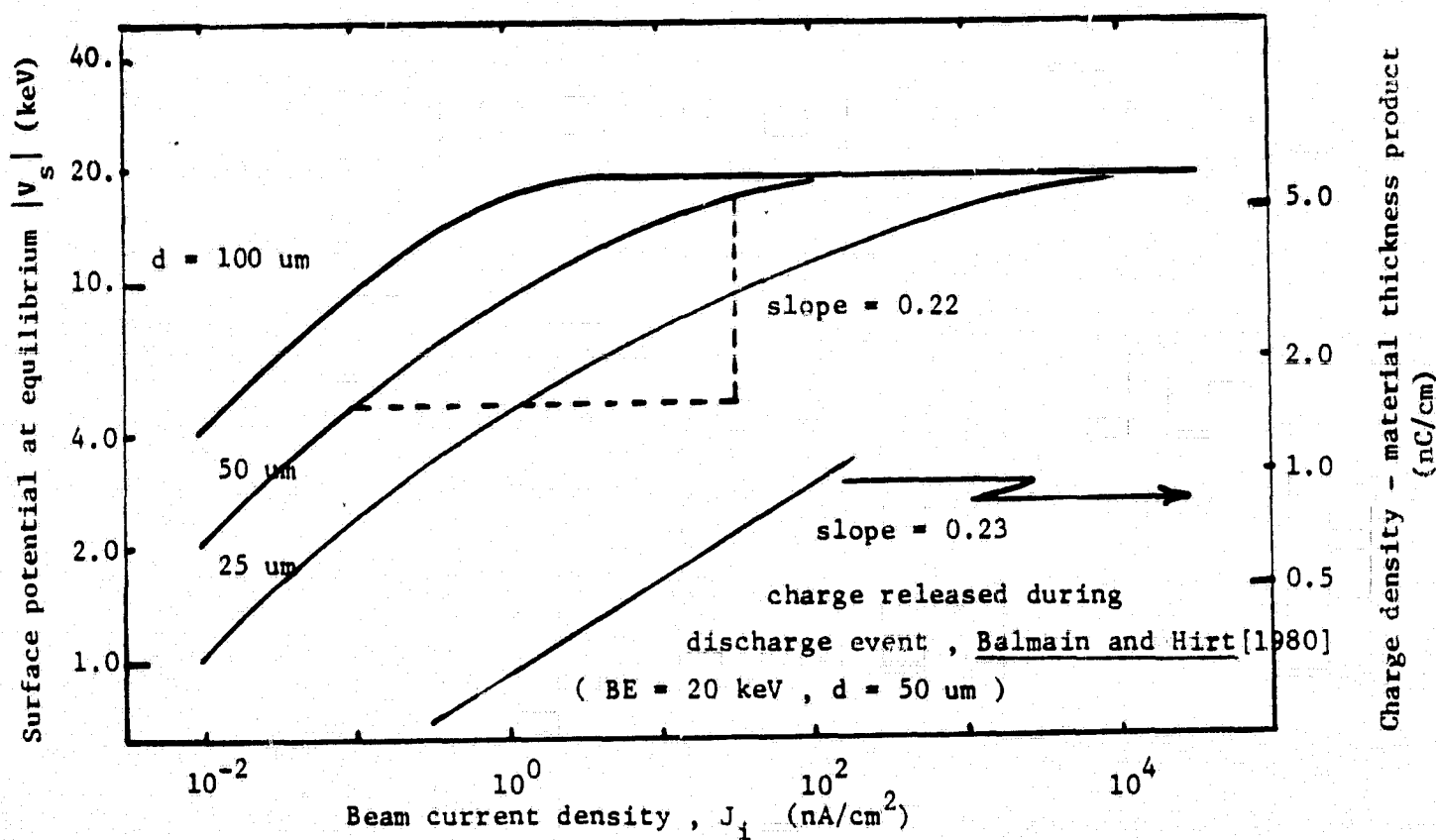


Fig. 3.3 The variation of released charge  $Q = \int i \, dt$  with dielectric specimen area. (from Balmain and Dubois [1979]).

----- net charge available at equilibrium

Fig. 3.4 Equilibrium surface potential and charge density vs. current density for Kapton.



ORIGINAL PAGE IS  
OF POOR QUALITY

Fig. 3.5 Incident electron current density (nA/cm<sup>2</sup>)

(from Balmain and Hirt [1980])

Substrate discharge current pulse properties for Kapton H. Beam energy = 20 keV, specimen area = 11.7 cm<sup>2</sup>, specimen thickness = 50  $\mu\text{m}$ .

balance to the surface (eq. 3.6) which is dependent upon the surface voltage through the effective capacitance (eq. 3.5), these two relations giving:

$$J_{\text{net}}(V) = -C \, dV/dt \quad (3.15)$$

For Teflon the incident current is assumed to be sufficiently large so that the charging process is emission-limited. Equation 3.15 can then be written as follows:

$$t J_1 d / \epsilon_0 \epsilon_r = - \int_0^V \frac{dV}{(1 - BS - SE)} \quad (3.16)$$

Numerical integration of eq. 3.16 for the energy-emission relationships suggested by Burke [1980] (eq. 2.1 and 2.7) and Robinson and Budd [1980] (eq. 2.8) produces the curves in Fig. 3.6. Both relationships yield reasonably consistent results. The experimental results of Purvis et al [1977] are in general much faster, but show the same qualitative behaviour. A more detailed comparison will be made in Chapters 4 and 6. Good agreement is obtained with the model developed by Beers et al [1980].

The voltage and charging dynamics as suggested in Fig. 3.6 can be matched to an arbitrary beam current density or material thickness by a simple scaling of the time axis.

### 3.3 Internal Model Development

The development of intense internal fields was first proposed by Meulenburt [1976]. It was suggested that two oppositely charged layers could develop in the irradiated material. As discussed in Chapter 2 secondary emission is a process that is essentially a surface phenomenon whereas the electron beam can pass through the surface with little attenuation resulting in a depletion of negative charge at the surface as illustrated in Fig. 3.7. A second negative charge layer was proposed at the mean electron range. If



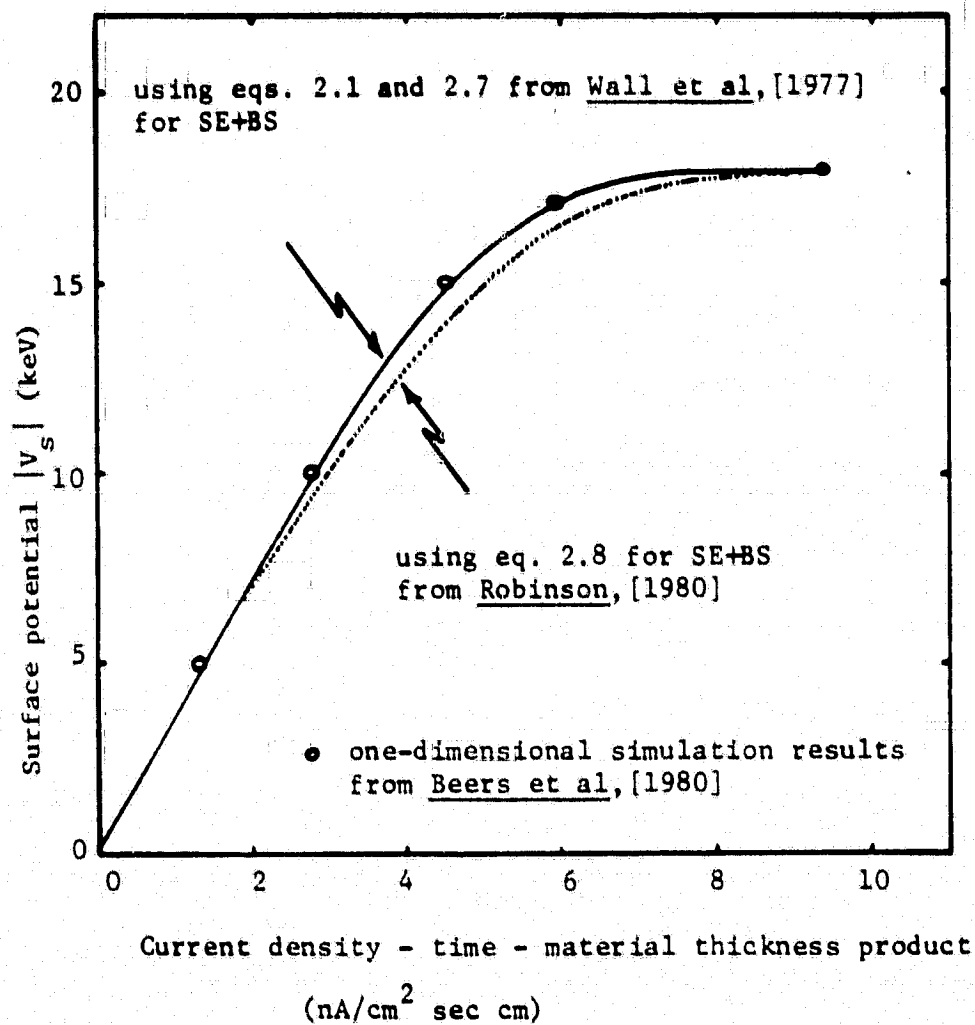
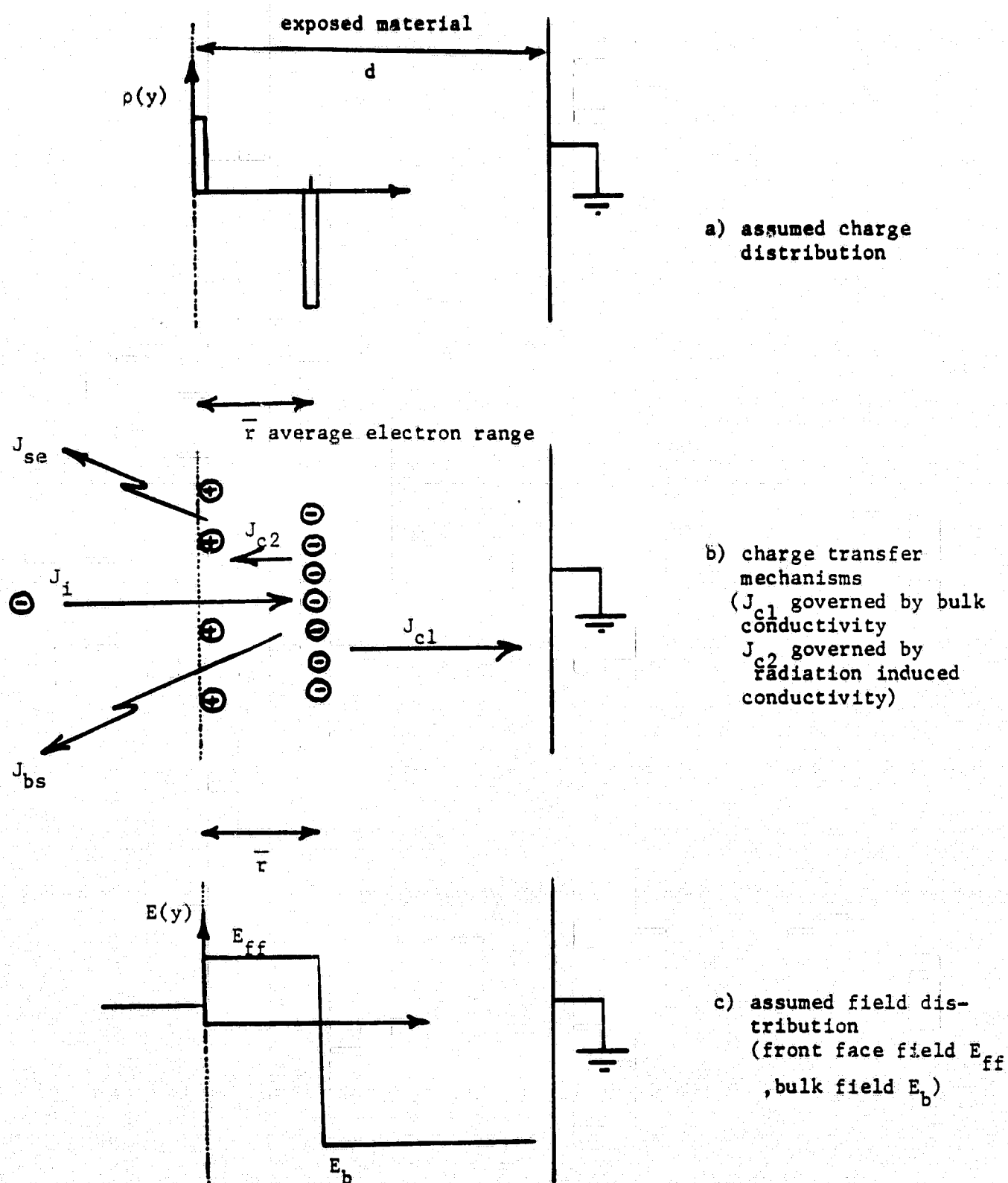


Fig. 3.6 Surface potential dynamics for Teflon.  
Beam energy 20 keV.

Fig. 3.7 Internal charging model geometry



the conductivity between these two layers, being dominated by the radiation induced component, is too small then breakdown fields could develop. Such a charge differential could continue to grow long after an external equilibrium has been established. These ideas have been refined in later work to include the details of electron deposition and beam induced conductivity profiles [Frederickson, 1979; Beers et al, 1979, Berkley, 1979].

The internal charging problem can be formulated from Gauss' law and the equation of continuity:

$$\partial E / \partial y = -q / \epsilon \quad (3.17)$$

$$\partial q / \partial t = \partial J_t / \partial y \quad (3.18)$$

where  $q$  = electron volume charge density  
(C/m<sup>3</sup>)

$J_t$  = total electron current density in  
the material in the neg.  $y$  direction

Following Beers et al [1979] we can isolate the electric field by combining eqs. 3.17 and 3.18.

$$\partial^2 E / \partial y \partial t = -1 / \epsilon \partial J_t / \partial y$$

integrating with  
respect to  $y$

$$\partial E / \partial t = -1 / \epsilon (J_t(y, t) - J_o(t)) \quad (3.19)$$

where  $J_t = J_p(y, t) + g(y, t) E(y, t)$

$J_p$  = primary beam current as determined by  
the electron deposition profile including backscatter

$g$  = conductivity as determined by the local  
dose rate

$J_o(t)$  = net external current density  
=  $J_i(1 - BS - SE)$

Both the primary beam current profile and the conductivity profile are influenced by the kinetic energy of the incident electrons which in turn is fixed by the surface potential and the beam energy (eq. 3.9). Equation 3.19 is therefore coupled to the surface potential described by eq. 3.16

The effect of covering the front surface with a thin (relative to the

range of the electrons in the covering) grounded metallized layer has been studied extensively [Gross et al, 1980; Oliveira and Gross, 1975; Gross et al, 1974]. A similar analysis is applicable to spacecraft charging conditions when photoemission from the illuminated specimen prevents the material from charging [Beers, 1979]. The steady state field under such conditions can be easily determined by requiring  $\partial q / \partial t = 0$ . Using eq. 3.18 we find the equivalent condition  $\partial J_t / \partial y = 0$  suggesting that

$$J_t = g(y)E(y) + J_p(y) = \bar{J} \quad (3.20)$$

where  $\bar{J}$  is some constant to be determined

The condition that both faces of the dielectric are at ground potential is used to find  $\bar{J}$  which then is used to determine the internal bulk field where  $J_p = 0$ .

$$\int_0^d E \, dy = 0$$

$$\bar{J} = \frac{\int_0^d J_p / g \, dy}{\int_0^d 1/g \, dy} \quad (3.21)$$

### 3.4 Internal Model Results

#### 3.4.1 Controlled Beam

By adjusting the beam energy, the kinetic energy at the surface can be fixed making  $J_p$  and  $J_o$  in eq. 3.19 constants in time. The resulting equation is easily solved:

$$E(y,t) = -(J_p(y) - J_o)/g(y) \quad (3.22)$$

$$+ (E(y,0) + (J_p - J_o)/g(y)) \exp(-g(y)t/\epsilon)$$

The final solution is independent of the initial field in the material at the

start of controlled irradiation.

Most spacecraft charging experiments are not performed with beam control; however eq. 3.22 can be applied to a steady state analysis for which  $J_0$  is constant and approximately equal to zero. For Teflon this occurs at an incident kinetic energy of 2.1 keV which, using eqs. 2.13, 2.11 and 2.17, implies an average radiation induced conductivity of  $1.5 \times 10^{-13} (\Omega\text{cm})^{-1}$  in the front irradiated volume for a beam density of  $1 \text{ nA/cm}^2$ . The resulting time constant is approximately 1.4 sec suggesting that these fields quickly assume a steady state value independent of the earlier charging history:

$$E(y) = -J_p(y)/g(y) \quad y < \bar{r} \quad (3.23)$$

where  $\bar{r}$  = average electron range

In the non-irradiated bulk region the dark conductivity is approximately  $10^{-18} (\Omega\text{cm})^{-1}$  giving a time constant of  $2.2 \times 10^5 \text{ sec}$  ( $\approx 61 \text{ hrs}$ ). The bulk field is essentially frozen at its initial value

$$E(y) = E(0,y) \quad y \gg \bar{r}$$

Under emission-limited charging conditions we have found

$$E(y) = (BE - KE_2)/(d - \bar{y}) \quad y \gg \bar{r} \quad (3.24)$$

For a non-charging beam ( $J_0 \equiv 0$ ) Beers et al have calculated the steady state field profile based on eq. 3.23 and illustrated in Fig. 3.8.

### 3.4.2 General Front Face Field

A unique front face field, first suggested by Beers et al [1979] for any beam energy, current density and material thickness, is a consequence of the assumptions inherent in the model. The magnitude of the internal field at the front face can be calculated at equilibrium as follows:

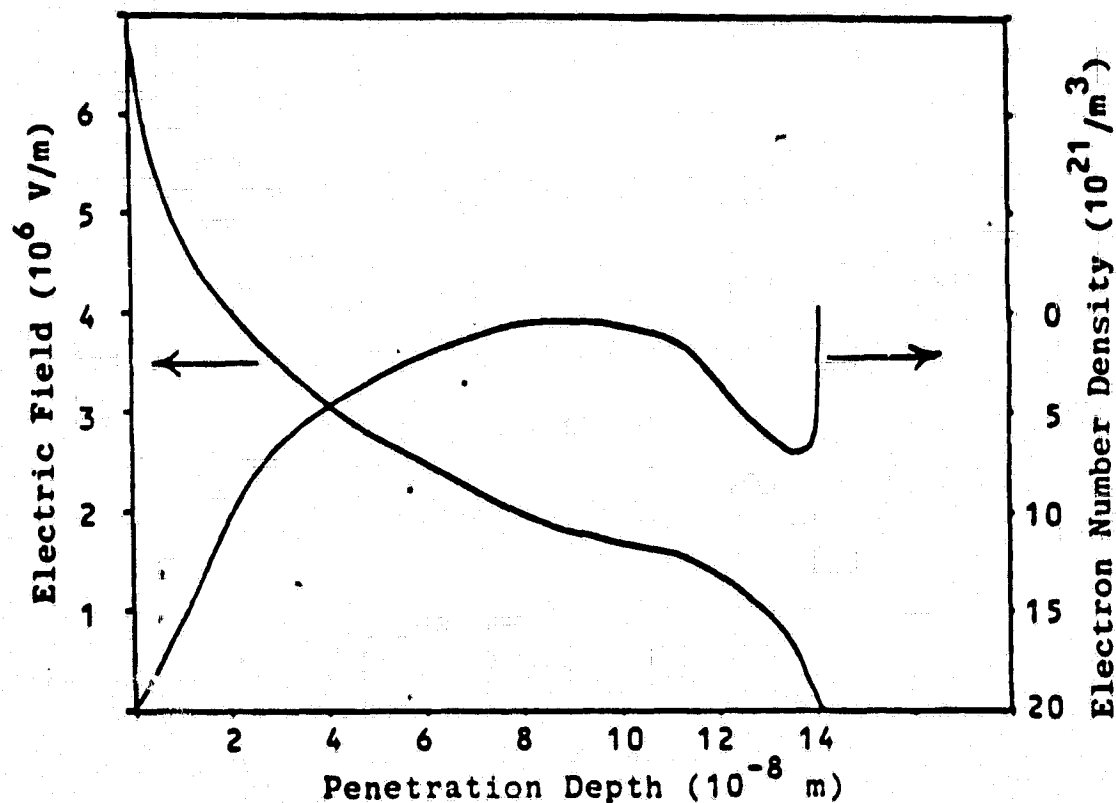


Fig. 3.8

SATURATION ELECTRIC FIELD IN TEFLON  
FOR NON-CHARGING NORMALLY INCIDENT BEAM

(from Beers et al, [1979])

MATERIAL	EQUILIBRIUM FRONT FACE FIELD (V/cm)
Teflon	$0.11 - 5.5 \times 10^4$
Mylar	$52.0 - 61. \times 10^4$
Kapton	$1.8 - 92. \times 10^4$

Table 3.1 Range in equilibrium front face fields for the values of radiation induced conductivity coefficients in Table 2.2 (from Beers et al, [1979])

from eq. 3.19  $\partial E / \partial t = -1/\epsilon (J_p + gE - J_o)$  (3.25)

at the surface  $J_p = J_1(1 - BS)$

and in general  $J_o = J_1(1 - BS - SE)$

thus  $\epsilon \partial E_{ff} / \partial t + gE_{ff} = -J_1 SE$

at equilibrium  $E_{ff} = -J_1 SE/g$  (3.26)

where  $E_{ff}$  = front face field

Using eqs. 2.7, 2.12, 2.13, 2.17 and 3.26 we find

$$|E_{ff}| = \frac{J_1^{1-\Delta} K KE_2^{(0.358\Delta-0.725)}}{G(2.08 \times 10^{13})^\Delta} \quad (3.27)$$

where for Teflon  $KE_2 = 2.1 \text{ keV}$

$$G = 1.7 \times 10^{-16} (\Omega \text{cm})^{-1}$$

$$\Delta = 0.7$$

$$K = 1.58$$

If the assumption is made that  $\Delta = 1$  it is found that  $E_{ff}$  is fixed only by material constants. Table 3.1 lists the computed bounds for the front face field using detailed dose profile calculations and the range of radiation-induced conductivity coefficients in Table 2.2 (assuming  $\Delta = 1$ ) [Beers et al, 1979]. Using an average uniform dose based on the equations presented in Chapter 2 the magnitude is bounded between  $5.7 \times 10^2 - 2.8 \times 10^4 \text{ V/cm}$  for Teflon. Using eq. 3.27 with  $\Delta = 0.7$  and a current density of  $1 \text{ nA/cm}^2$  the equilibrium field is  $6.1 \times 10^3 \text{ V/cm}$  with a current density dependence of  $(J_1/1 \text{ nA/cm}^2)^{0.3}$ .

It should be noted that all of these estimates are less than the expected breakdown threshold, the largest occurring in Kapton. The discrepancy in the results derived here and those obtained by Beers et al [1979] appear to be due to the assumed range-energy relationship (eq. 2.11) at the low energy end.

### 3.4.3 Grounded Front Face Results

The steady state field can be determined from eq. 3.20 once the primary electron current has been established. For thick samples we find from eq. 3.21 that

$$J_p(y) \gg \bar{J} \quad \text{for } y < \bar{r}$$

$$\text{thus} \quad E(y) \approx -J_p(y)/g(y) \quad (3.28)$$

where  $g(y)$  is dominated by the radiation induced conductivity

The front face field can be calculated as in section 3.5.2. Using eq. 2.1 for the backscatter coefficient we find at the front surface:

$$J_p = J_1(1 - BS) \approx 0.9 J_1$$

$$\text{therefore at steady state} \quad |E_{ff}| = 0.9 J_1/g$$

$$= (4.8 \times 10^{-14}) \Delta_{KE}^{0.358} \Delta_{J_1}^{(1-\Delta)} 0.9/g \quad (3.29)$$

Whereas in eq. 3.27 the value of KE was fixed at the second unity emission energy, the value of KE in eq. 3.29 is equal to the beam energy since the front surface is held at ground potential.

For  $J_1 = 1 \text{ nA/cm}^2$ ,  $KE = 20 \text{ keV}$  and  $\Delta = 0.7$  the front face field is equal to  $1.1 \times 10^4 \text{ V/cm}$  (roughly twice that found for a floating front face). Note there is a weak dependence on both the beam current density ( $J_1/1 \text{ nA/cm}^2$ )<sup>0.3</sup> and the beam energy ( $BE/20 \text{ keV}$ )<sup>0.25</sup>.

In the non-irradiated bulk of the material the average field strength will be reduced by a factor  $\bar{r}/d$  from that found in the irradiated volume. For a  $50 \mu\text{m}$  thick sample under the above conditions the bulk field should be approximately  $1.7 \times 10^3 \text{ V/cm}$  with a beam energy dependence of  $(BE/20 \text{ keV})^{1.61}$ .



To summarize the grounded front surface results, the front face field is increased by roughly a factor of 2 while the bulk field is decreased by a factor of  $2 \times 10^3$  when compared to the sample calculations made for a floating front surface. Beers et al [1979] have calculated an upper limit for the front face fields for  $\Delta = 1$  as seen in Fig. 3.9. The results are independent of current density and use a detailed dose profile calculation. Note for both Mylar and Kapton the upper estimates are comparable to the material breakdown threshold at beam energies greater than 5 keV.

#### 3.4.4 Experimental and Numerical Results

Experiments performed by Gross et al [1977] have addressed the question of internal charge deposition and migration. The charge centroid was found to be equal to the average electron range at the start of irradiation and it subsequently approached the extrapolated range if time was allowed for internal charge migration. As the net stored charge increased a corresponding increase in the final charge centroid depth was noted, reflecting the higher internal field. This dependence is weak being approximately proportional to the logarithm of the bulk field.

The charge centroid was found to be sensitive to beam current densities greater than  $5 \text{ nA/cm}^2$  decreasing with increasing current density while the net injected charge was held constant. Such behaviour supports the use of a non-linear radiation induced conductivity as outlined in section 2.5.4.

Beers et al [1980] have developed the necessary computer codes to solve numerically the complete internal charging history for a one dimensional model (eq. 3.19) and have presented steady state results for both Kapton and Teflon (Figs. 3.10 and 3.11 respectively). The extremes in the internal electric field appear at the front face of the material or in its bulk. The behaviour of both of these quantities have been discussed in the preceding sections.

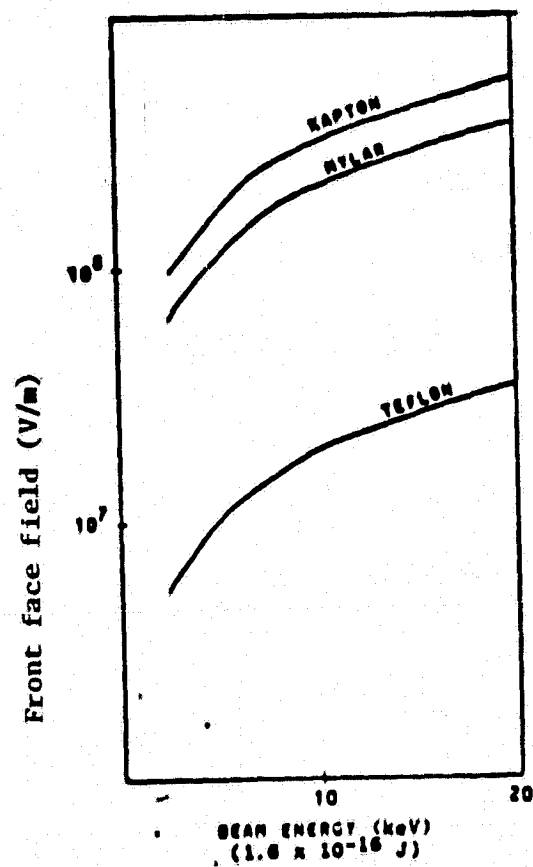


Fig. 3.9 Front face field at equilibrium for both surfaces held at ground potential. Minimum value of G from Table 2.2 . (from Beers et al, [1979])

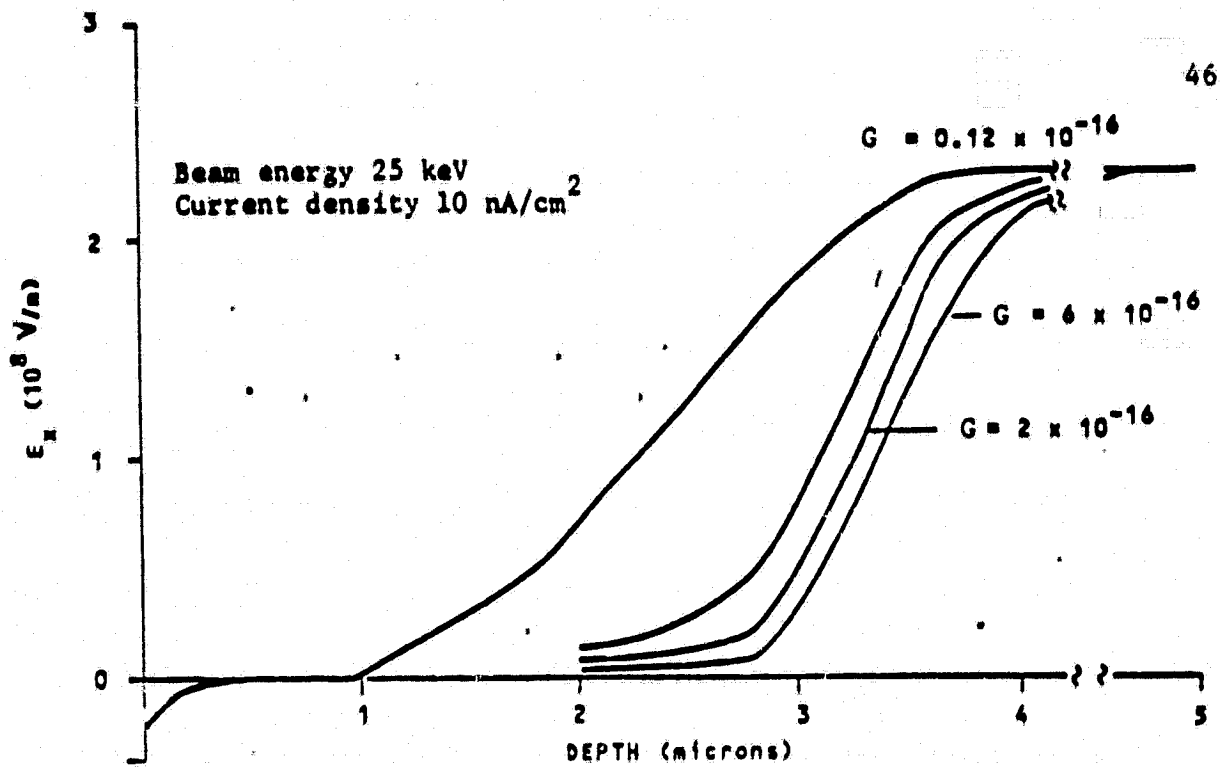


Fig. 3.10 Equilibrium electric field profile in Kapton.  
(from Beers et al, [1980])

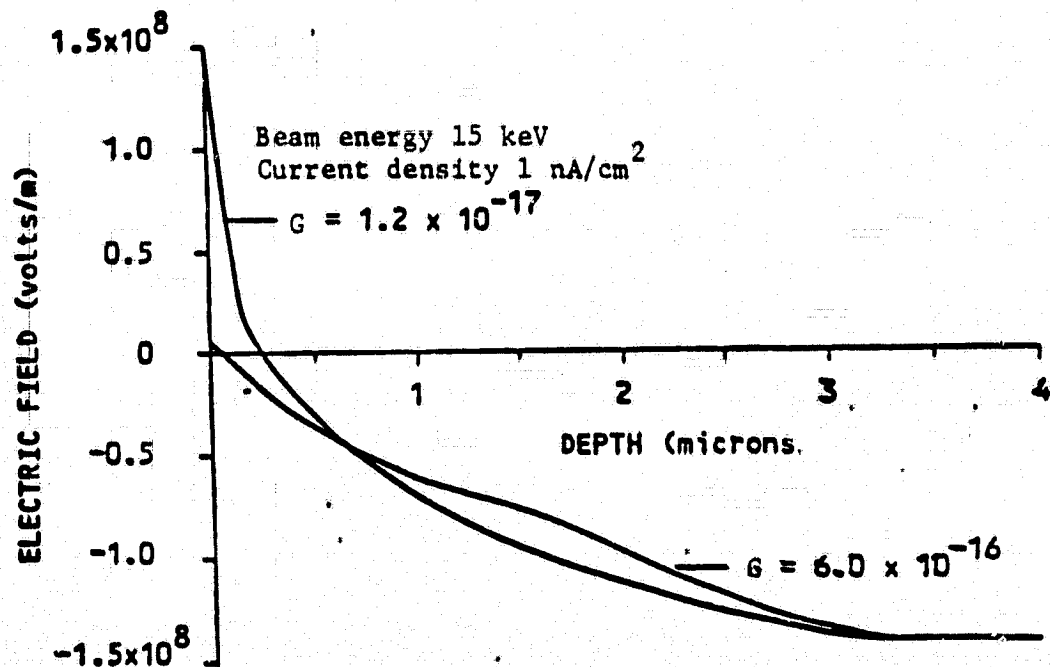


Fig. 3.11 Equilibrium electric field profile in Teflon.  
(from Beers et al, [1979])

#### 4. TWO-DIMENSIONAL SIMULATION DESCRIPTION

A fully three-dimensional description such as the NASA charging analyzer program NASCAP [Katz et al, 1979] can describe the charging of an arbitrary body exposed to a general electron/ion environment. Unfortunately a penalty must be paid for such flexibility in terms of cost and complexity.

In this study our attention has focused on structures that can be composed of long, uniform parallel dielectric strips above an infinite conducting ground plane. Under such conditions the accumulation of charge can be described in only two dimensions thus achieving considerable savings in both cost and effort while isolating the effect of the metal-dielectric edge in the charging process. The two-dimensional model described in this section is a direct extension of the one-dimensional work described in Chapter 3 to include those effects associated with the deflection of the incident beam by the developing charge distribution.

The basic geometry, symbol definition and coordinate system are given in Fig. 4.1. The results obtained, although idealized, should still be applicable to the central portion of any long uniform strip. Many laboratory simulations of spacecraft charging [Balmain and Hirt, 1980; Purvis et al, 1979; Yadlowsky et al, 1980] have been performed that can be adequately represented in this manner.

##### 4.1 External Charging Model

The external charging model specifying the accumulation of net charge in the dielectric as a function of time is described by the equation of charge continuity

$$\partial q / \partial t = -\nabla \cdot J_{\text{net}} \quad (4.1)$$

where  $q$  = volume charge density

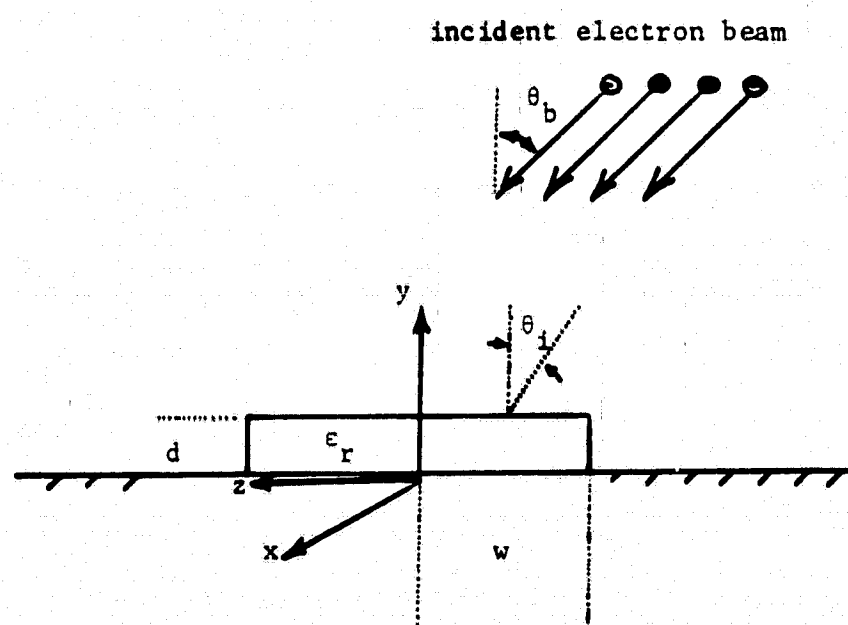


Fig. 4.1 Model geometry

As was indicated in Section 3.1 the voltage and external electric fields are relatively insensitive to the internal charge distribution for thick samples. For the purposes of the external model we shall consider the charge to be deposited at a constant height  $d$ , equal to the material thickness, above the ground plane. Using eq. 3.7 for the net current density, we can write eq. 4.1 in the following difference form:

$$\rho(z, T+t) = (J_i - J_{bs} - J_{se} - J_c)t \quad (4.2)$$

where all currents refer to the component in the negative  $y$  direction (the question of tangential conduction current effects is addressed in Section 4.3)

$\rho$  = net surface charge density

In general all of the currents are functions of time and position  $z$  because they are determined by the growing charge distribution. The problem is therefore to relate the net current at the surface to the net charge residing on the surface.

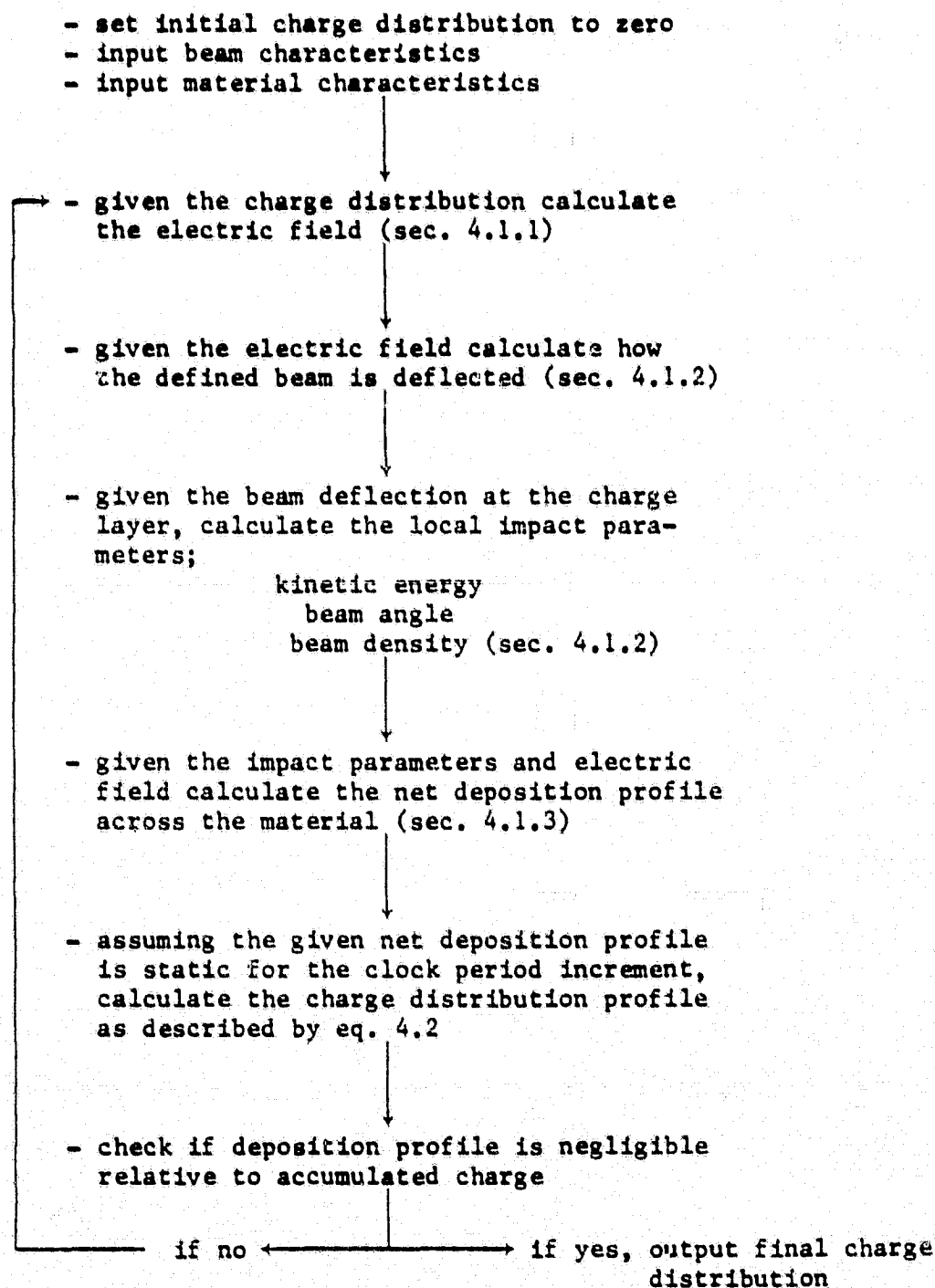
A solution outline is given in Fig. 4.2 in the form of a flowchart. Details on each stage of the chart are given in subsequent subsections.

#### 4.1.1 Derivation of the Electric Field from an Arbitrary Surface Charge Distribution

The charge layer responsible for the unknown field is assumed to be located in the dielectric at a constant height above an infinite ground plane. In general, the effect of the dielectric is to reduce the effective charge layer due to the polarization of the material. From Jordan and Balmain [1968] if the material is homogeneous the potential at a given observation point  $\bar{r}$  (see Fig. 4.3) due to this polarization is given by

$$\Phi_p(\bar{r}) = \oint_s \rho_p / 4\pi\epsilon_0 R \, da \quad (4.3)$$

Fig. 4.2 Flow Chart: External Charging Model



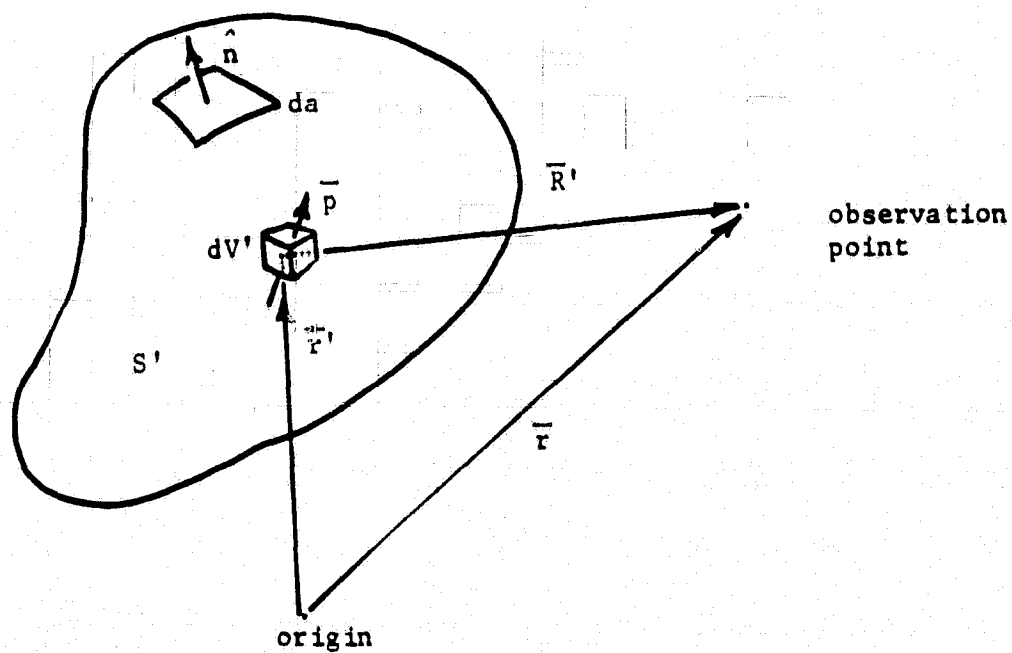


Fig. 4.3 Definition of symbols in eq. 4.3



$$\text{where } \rho_p = \bar{P} \cdot \hat{n}$$

$$\bar{P} = \text{polarization}$$

Equation 4.3 suggests that the dielectric can be replaced by a surface charge equal to  $\rho_p$ . In addition we can replace the ground plane by the appropriate image charges to obtain a simple volume charge distribution in free space. The final potential is calculated using the resulting charge distribution in free space and the familiar Green's function:

$$\Phi_{\text{total}} = \int_V \rho / 4\pi\epsilon_0 R \, dV \quad (4.4)$$

where  $\rho$  = equivalent charge in free space

This sequence of steps is illustrated in Fig. 4.4. Comparing Figs. 4.4(a) and 4.4(d) we find

$$\epsilon_0(E_1 - E_2) = -(\rho_p + \rho_s) \quad (4.5)$$

$$\epsilon_0(E_1 - \epsilon_r E_2) = -\rho_s$$

therefore

$$(\rho_p + \rho_s) / \rho_s = \frac{(1 - E_1/E_2)}{(\epsilon_r - E_1/E_2)} \quad (4.6)$$

where  $\rho_p + \rho_s$  = equivalent charge in free space

$\rho_s$  = actual net free charge in the dielectric

Unfortunately,  $E_1$  and  $E_2$  cannot be determined until the equivalent charge in free space has been determined. In the simulation the ratio  $E_1/E_2$  from the previous iteration is used to calculate the effective charge density. The procedure is initiated by assuming  $|E_1/E_2| \ll 1$  which yields the conventional result: the effective free space charge is  $1/\epsilon_r$  the actual charge in the dielectric.

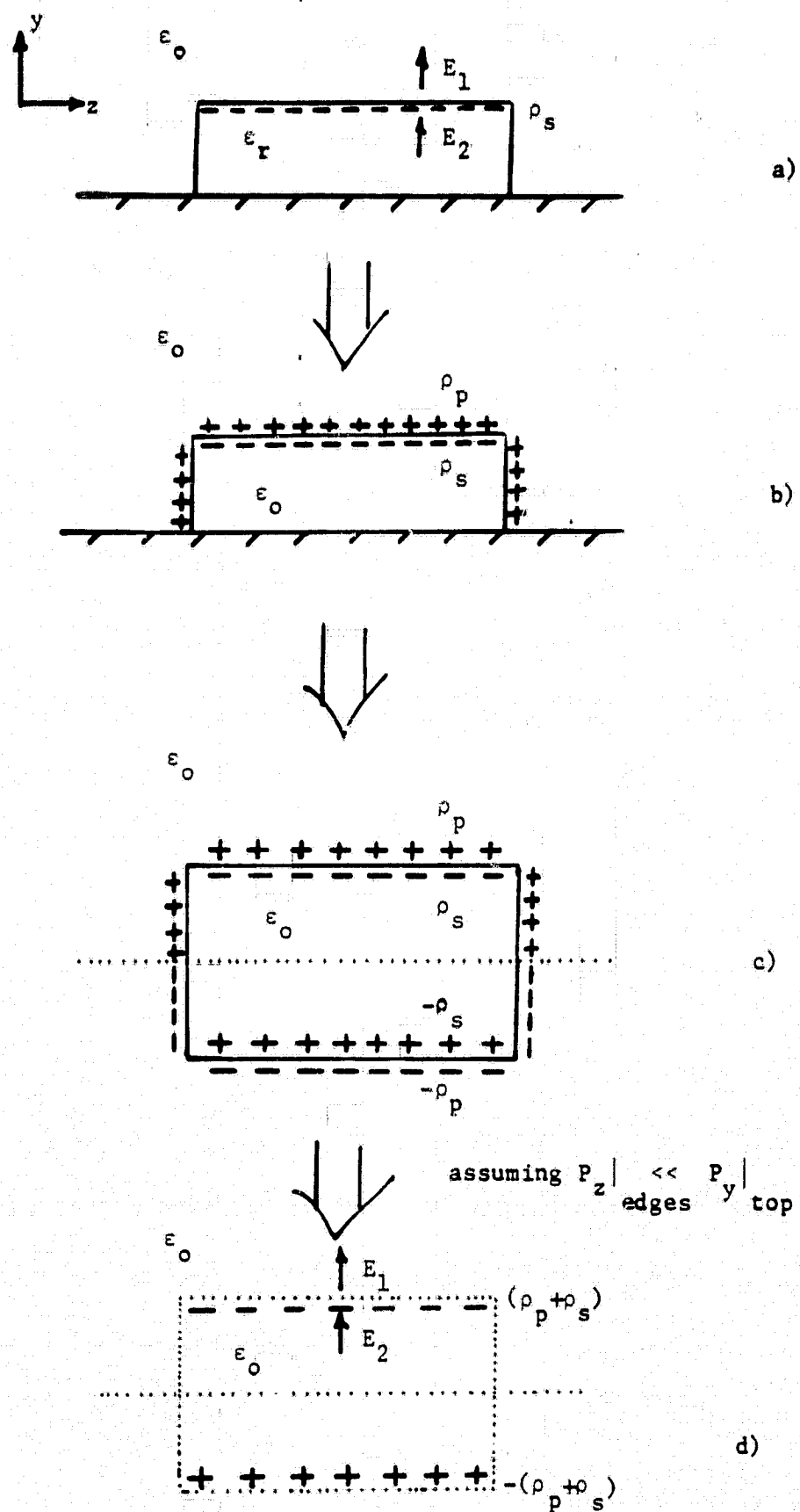


Fig. 4.4 Development of the equivalent charge in free space

The charge distribution in Fig. 4.4(d) suggests that eq. 4.4 can be simplified to two surface integrals on planes located at  $y = \pm d$ .

$$\begin{aligned}\phi &= \int_{-L}^L \int_{-W}^W \frac{\rho(z)}{4\pi\epsilon_0} \left( \frac{1}{\sqrt{(x-x')^2 + (y-d)^2 + (z-z')^2}} \right. \\ &\quad \left. - \frac{1}{\sqrt{(x-x')^2 + (y+d)^2 + (z-z')^2}} \right) dx' dz' \\ &= \frac{1}{4\pi\epsilon_0} \int_{-W}^W \rho(z') \ln \left( \frac{(x-x') + \sqrt{(x-x')^2 + (y+d)^2 + (z-z')^2}}{(x-x') + \sqrt{(x-x')^2 + (y-d)^2 + (z-z')^2}} \right) \Bigg|_{x'=-L}^{x'=L} dz'\end{aligned}$$

where  $W, L$  are the half width and half length of the material

if  $(x \pm L)^2 \gg (y \pm d)^2 + (z - z')^2$  we find

$$\phi \approx \frac{1}{4\pi\epsilon_0} \int_{-W}^W \rho(z') \ln \left( \frac{(y+d)^2 + (z-z')^2}{(y-d)^2 + (z-z')^2} \right) dz'$$

assuming  $\rho(z') = A + Bz'$  where  $A, B$  are constants

$$\begin{aligned}\phi &= \frac{1}{4\pi\epsilon_0} \left( (A + Bz) \left( s \ln \left( \frac{s^2 + (y-d)^2}{s^2 + (y+d)^2} \right) + \right. \right. \\ &\quad \left. \left. 2(y-d) \operatorname{atan}\left(\frac{s}{y-d}\right) - 2(y+d) \operatorname{atan}\left(\frac{s}{y+d}\right) \right) - \right. \\ &\quad \left. \frac{1}{2}B \left( ((y-d)^2 + s^2)(\ln(s^2 + (y-d)^2) - 1) - \right. \right. \\ &\quad \left. \left. ((y+d)^2 + s^2)(\ln(s^2 + (y+d)^2) - 1) \right) \right) \Bigg|_{s=z-w}^{s=z+w}\end{aligned} \quad (4.7)$$

The electric fields are related to the scalar potential by

$$\vec{E} = -\nabla \phi$$

which yields

$$E_y = \frac{1}{4\pi\epsilon_0} (2(A + Bz) (\operatorname{atan}(\frac{s}{y+d}) - \operatorname{atan}(\frac{s}{y-d})) - B((y+d) \ln((y+d)^2 + s^2) - (y-d) \ln((y-d)^2 + s^2))) \Bigg|_{s=z-w}^{s=z+w} \quad (4.8)$$

$$E_z = \frac{1}{4\pi\epsilon_0} ((A + Bz) \ln(\frac{(y+d)^2 + s^2}{(y-d)^2 + s^2}) + 2B ((y+d) \operatorname{atan}(\frac{s}{y+d}) - (y-d) \operatorname{atan}(\frac{s}{y-d}))) \Bigg|_{s=z-w}^{s=z+w} \quad (4.9)$$

The actual charge distribution  $\rho$  cannot in general be represented in the form  $A + Bz$ . The fields can, however, be found by the superposition of solutions for each segment of a piecewise linear approximation to the actual charge distribution. The piecewise linear model is chosen to be continuous and to have a mean square error less than a set fraction of the average charge density. Figure 4.5 shows an example of the segmented approximation chosen to satisfy a mean square error constraint and the original charge distribution it represents. The position of the segments are chosen in such a fashion as to shift the end points between successive iterations thus minimizing the accumulative effect of discontinuities in the slope on the charging model.

To summarize, the actual charge distribution is transformed using eq. 4.6 to give an equivalent charge in free space which is then approximated by a continuous piecewise linear function. The total electric field is then found by summing the contributions of each segment calculated using eqs. 4.8 and 4.9.

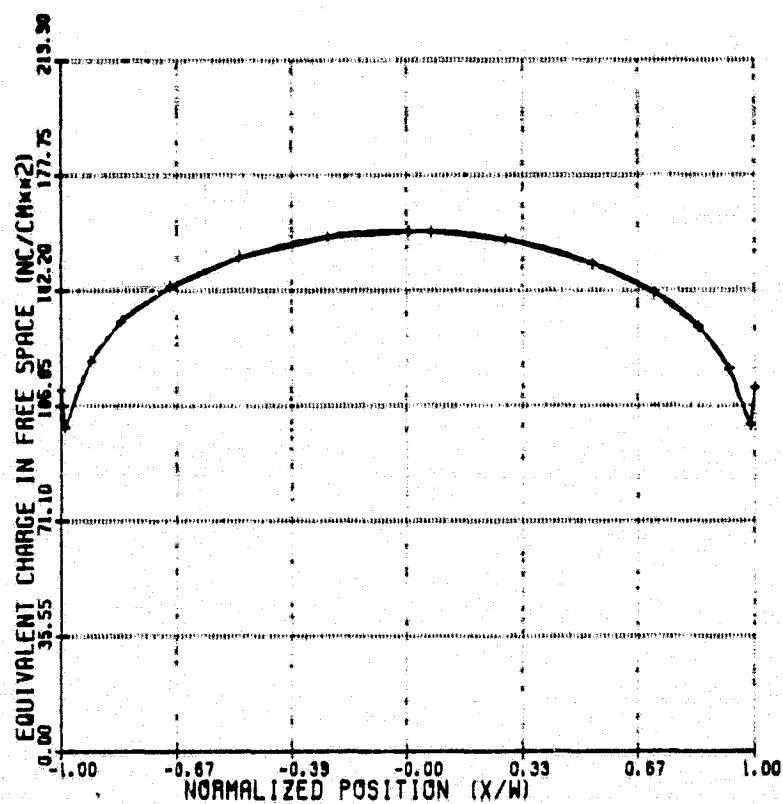


Fig. 4.5 A charge distribution and typical piecewise linear approximation to it (end points of the segments are marked with a "+").

#### 4.1.2 Incident Current Profile

As the surface potential reaches a level comparable to the beam accelerating voltage the electric field above the material strongly influences the incident beam profile. An understanding of the beam dynamics can be obtained by tracing individual electron trajectories.

The necessary equations of motion are:

$$\begin{aligned} d^2z/dt^2 &= -|e/m| E_z(z,y) \\ d^2y/dt^2 &= -|e/m| E_y(z,y) \end{aligned} \quad (4.10)$$

It is assumed that  $\bar{E}$  is constant in time for the duration of the trajectory. This coupled system of equations was numerically solved using a third order Runge-Kutta method with adaptive time increment. The formulation is suited for second order differential equations for which a first derivative is not involved. The related difference equations for the z component are [Weber 1967]:

$$z(T+t) = z(T) + t(\dot{z}(T) + 1/4 (k_z^0 + k_z^1))$$

$$\dot{z}(T+t) = \dot{z}(T) + 1/4 k_z^0 + 3/4 k_z^1$$

where  $\dot{z} = dz/dt$

$t$  " a time increment

$$k_z^0 = -|e/m|t E_z(z(T), y(T))$$

$$k_z^1 = -|e/m|t E_z(z^*, y^*)$$

$$z^* = z(T) + 2/3 \dot{z}(T) + 2/9 k_z^0 t$$

(a similar set of equations is used for the y-component).

The neglected terms are of the order  $t^4$ . A measure of the local error can be obtained by introducing  $k_z^2$ .

$$k_z^2 = -|e/m|t E_z(z(T+t), y(T+t))$$

The error in  $z$  and  $\dot{z}$  are given by:

$$\text{Error}(z) = t(-1/4 k_z^0 + 1/4 k_z^1)$$

$$\text{Error}(\dot{z}) = 1/2 k_z^0 - 3/2 k_z^1 + k_z^2$$

The method, incorporating an adaptive time increment procedure to maximize  $t$  subject to local error estimate constraints on  $z, \dot{z}, y, \dot{y}$ , requires only two function evaluations per coordinate per iteration. A further check on the global accuracy of the trajectory subroutines was performed at charging equilibrium wherein the conservation of energy condition (eq. 3.9) was verified across the surface.

The trajectories are terminated on a plane defined by the upper surface of the material using an iterative selection of the final time increment.

By sampling the material's surface with test electrons we are able to deduce the incident beam profile. The impact parameters, namely the angle of incidence and the kinetic energy of the incident electrons as functions of position are obtained directly from the trajectory calculations. The incident current density is obtained by comparing the relative deflection of neighbouring trajectories as indicated in Fig. 4.6. If we assume neighbouring electrons with the same initial velocity and a slight lateral displacement do not cross, then the net current through the upper and lower surface will be equal. Because there is no charge accumulation in the volume  $V$ , it follows that

$$J_{y1}/J_{y2} = s_2/s_1 \quad (4.11)$$

Equation 4.11 is used to relate the incident current density  $J_1$ , to be used in eq. 4.2, to the beam current density via the calculated trajectories.

#### 4.1.3 Net Charge Accumulation

The net current density, as indicated in eq. 4.2, represents the

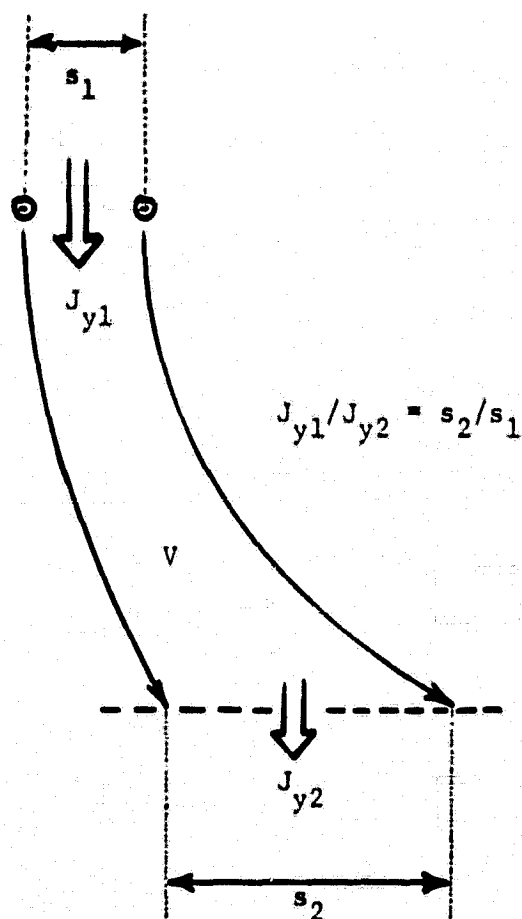


Fig. 4.6 Calculation of the incident current density due to beam spreading.



difference between incoming and outgoing currents. The outgoing currents include the backscatter current, the secondary emission current and the bulk conduction current. Although each has been described in Chapter 2 the functional forms used in the simulation will be summarized here.

$$J_{bs} = 0.1 \text{ KE}^{-0.2} J_1 \quad \text{for Teflon and Kapton}$$

$$J_{se} = 1.55 \text{ KE}^{-0.725} J_1 \exp(2(1 - \cos\theta)) \quad \text{for Teflon}$$

$$= 0.68 \text{ KE}^{-0.725} J_1 \exp(2(1 - \cos\theta)) \quad \text{for Kapton}$$

$$J_c = 5 \times 10^{-18} \left( \frac{2 + \cosh(4.68 \times 10^{-3} E^{1/2})}{3} \right) E \quad \text{for Kapton}$$

$$= 0 \quad \text{for Teflon}$$

where  $E$  = y component of electric field (V/cm)

$\text{KE}$  = incident kinetic energy (keV)

In keeping with the discussion in Chapter 3, all of the results for Teflon are assumed to be secondary emission limited.

#### 4.2 Internal Charging Model

The results presented in Chapter 3 indicate that the maximum internal fields at equilibrium occur at the front face and in the non-irradiated bulk of the material. The bulk fields can be obtained directly from the external charging model as they are outside the free charge distribution. The front face field can be estimated assuming a uniform dose rate throughout a volume defined by the mean electron range. The proposed charge distribution is illustrated in Fig. 4.7. The net charge as used by the external model is  $-(\rho_1 + \rho_2)$  where  $\rho_1$  is a surface-depletion charge due to secondary emission and  $\rho_2$  is a charge layer due to the primary electrons. The external surface electric field  $E_1$  can be calculated from the external model. The internal fields  $E_2$  and  $E_3$  are functions of  $\rho_1$  and  $\rho_2$  as follows:

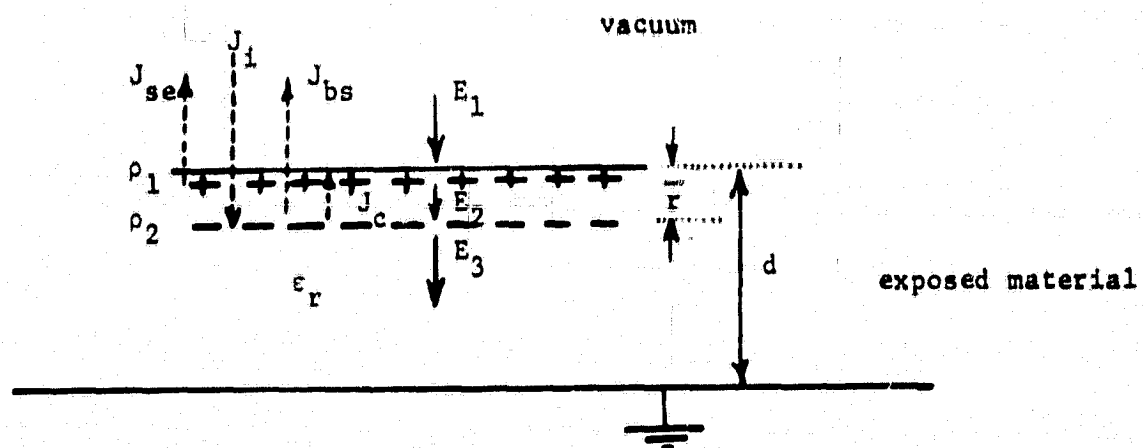


Fig. 4.7 Internal charging model for Teflon.  
A bulk conduction current to ground is included  
for Kapton.

$$\begin{aligned}\epsilon_r E_2 - E_1 &= \rho_1 / \epsilon_0 \\ E_3 - E_2 &= \rho_2 / \epsilon_0 \epsilon_r\end{aligned}\quad (4.12)$$

Balancing the currents out of the first charge layer  $\rho_1$ , we find

$$\begin{aligned}d\rho_1/dt &= J_{se} - J_c = J_{se} - gE_2 \\ d\rho_1/dt &= (J_{se} - gE_1/\epsilon_r) - (g/\epsilon_0 \epsilon_r)\rho_1\end{aligned}\quad (4.13)$$

Over the period of a time increment in the external charging model  $E_1$  will be approximately constant and eq. 4.13 reduces to an ordinary differential equation with constant coefficients which can be easily solved.

$$\begin{aligned}\rho_1(t) &= (J_{se} - gE_1/\epsilon_r)\epsilon_0 \epsilon_r / g + \\ &(\rho_1(0) - \epsilon_0 \epsilon_r / g (J_{se} - gE_1/\epsilon_r)) \exp(-g s / \epsilon_0 \epsilon_r)\end{aligned}\quad (4.14)$$

where  $T \leq s \leq T + t$

$\rho_1(0)$  = charge at the beginning of the iteration

The steady state solution is

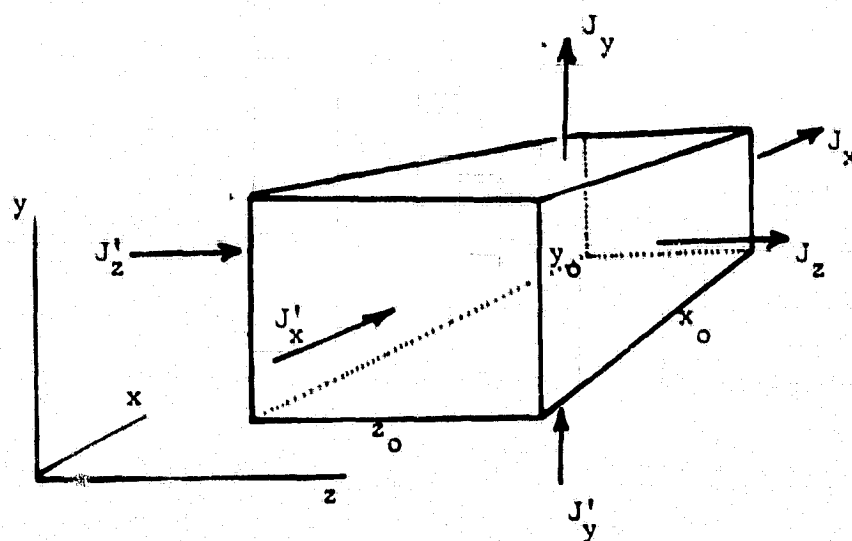
$$\rho_1 = (J_{se} - gE_1/\epsilon_r)\epsilon_0 \epsilon_r / g \quad (4.15)$$

$$E_2 = J_{se} / g = |E_{ff}| \quad (4.16)$$

Note the field between the two charge layers  $E_2$  is independent of the external field and is equal to the expression obtained for the front face field in the one-dimensional analysis (eq. 3.27).

#### 4.3 Transverse Conduction Current

The possibility of strong tangential fields near the sample edge suggests the inclusion of transverse currents and subsequent free charge transfer in the model. A three-dimensional analysis can be developed based on Fig. 4.8



$$-\partial q / \partial t = (J_x - J'_x) y_0 z_0 + (J_y - J'_y) x_0 z_0 + (J_z - J'_z) y_0 x_0$$

Fig. 4.8 Three-dimensional current balance in volume element  $x_0 y_0 z_0$ .

and eq. 4.1. If  $q$  is the charge contained in the volume  $x_0 y_0 z_0$  in Fig. 4.8 then

$$\begin{aligned} -dq/dt = & (J_x - J_x') y_0 z_0 + (J_y - J_y') x_0 z_0 \\ & + (J_z - J_z') y_0 x_0 \end{aligned}$$

For an infinite strip  $J_x = J_x' = 0$ . The change in the free charge per unit surface area is

$$-dp/dt = (J_y - J_y') + (J_z - J_z') y_0 / z_0 \quad (4.17)$$

$$\text{where } \rho = q / x_0 z_0$$

Assuming that the non-irradiated volume is blocking the transverse currents must be confined to a shallow surface layer with a thickness approximately equal to the electron range. Equation 4.17 can therefore be written

$$\partial \rho / \partial t = J_y' - J_y + g \bar{r} (E_z - E_z') / z_0 \quad (4.18)$$

$$\text{where } (E_z - E_z') / z_0 = \partial E_z / \partial z$$

$$\bar{r} = \text{average electron range}$$

$$\text{assuming } \partial E_z / \partial z > E_z / g = \partial g / \partial z$$

Tangential currents were not included in the general model as considerable uncertainty persists concerning the transfer of charge from the material edge. It was felt that the edge could be characterized by two extremes: infinite edge resistance and zero edge resistance. Infinite edge resistance is used to describe the boundary condition that  $J_z = 0$  at the edge. Zero edge resistance is used to describe the boundary condition that  $\partial J_z / \partial z = 0$  (i.e. no charge accumulation occurs at the edge due to surface tangential currents). Results have been obtained for both extremes. No attempt was made to model an inherent surface conductivity.

## 5. SIMPLIFIED ANALYSIS

The charging behaviour of the central portion of the dielectric strip when exposed to a normally incident uniform electron beam can be predicted using approximate field expressions. The approximations are valid when trajectory displacements from the centre are small compared to the half width of the material and are based on an assumed uniform charge distribution. The results are sufficiently accurate to be useful in practice and also provide data for later comparison with the fully numerical approach in Chapter 6.

### 5.1 Central Fields of a Uniform Charge Distribution

The following expressions are obtained from eqs. 4.7, 4.8 and 4.9 assuming  $y \gg d$  and a uniform charge distribution (i.e.  $A = \rho_0$ ,  $B = 0$ )

$$\phi = -\frac{\rho_0 d}{\pi \epsilon_0} \left( \text{atan}\left(\frac{z-w}{y}\right) - \text{atan}\left(\frac{z+w}{y}\right) \right) \quad (5.1)$$

$$E_y = -\frac{\rho_0 d}{\pi \epsilon_0} 2w \frac{(z^2 - y^2 - w^2)}{(y^2 + (z-w)^2)(y^2 + (z+w)^2)} \quad (5.2)$$

$$E_z = \frac{\rho_0 d}{\pi \epsilon_0} 4w \frac{yz}{(y^2 + (z-w)^2)(y^2 + (z+w)^2)} \quad (5.3)$$

It is apparent from these equations that if the equilibrium condition is governed by the external fields, as is the case for emission-limited charging, an equilibrium state can be defined for an arbitrary material thickness by the steady state dipole moment per unit area  $\rho(z)d$  which produces a unique set of external equilibrium fields. The steady state charge density is thus found to be inversely proportional to the material thickness as implied in eq. 3.5 for a given equilibrium surface potential.

Equations 5.1, 5.2 and 5.3 can be further simplified if we restrict our attention to the region where  $z/w \ll 1$ . Ignoring terms of the order  $(z/w)^2$  we find

$$\phi = 2 \rho_0 d / \pi \epsilon_0 \operatorname{atan} w/y \quad (5.4)$$

$$E_y = \rho_0 d 2w / \pi \epsilon_0 1/(y^2 + w^2) \quad (5.5)$$

$$E_z = \rho_0 d 4w / \pi \epsilon_0 yz/(y^2 + w^2)^2 \quad (5.6)$$

The equation of motion in the  $y$  direction, using eq. 5.5, is found to be independent of the  $z$  coordinate. If we assume that  $(\dot{y})^2 \gg (\dot{z})^2$  (i.e. a paraxial approximation) we find

$$\dot{y} = \sqrt{2BE/m - 2|\phi(y)e/m|} \quad (5.7)$$

Equation 5.7 can be integrated numerically to find the vertical component of the trajectory as a function of time. The equation of motion in the  $z$  direction is more complicated but can again be treated numerically once  $y(t)$  is known. In general it takes the form

$$\ddot{z} = f(t) z \quad (5.8)$$

where  $f(t)$  is a function of time defined by eqs. 5.6 and 5.7

$$z(0) = z_0, \dot{z}(0) = 0$$

By simple substitution it is evident that if a solution to eq. 5.8 exists  $g_1(t)$  then a scalar multiple  $g_2 = \alpha g_1(t)$  will also satisfy it with the new initial conditions:  $g_2(0) = \alpha g_1(0)$ ,  $\dot{g}_2(0) = 0$ . Because the  $y$  component is independent of  $z$ , two neighbouring trajectories represented by  $g_1$  and  $g_2$  are simply related by scaling the  $z$  coordinate of the path as indicated in Fig. 5.1. The incident current density is therefore constant in the central region and can be determined by a single trajectory calculation as indicated

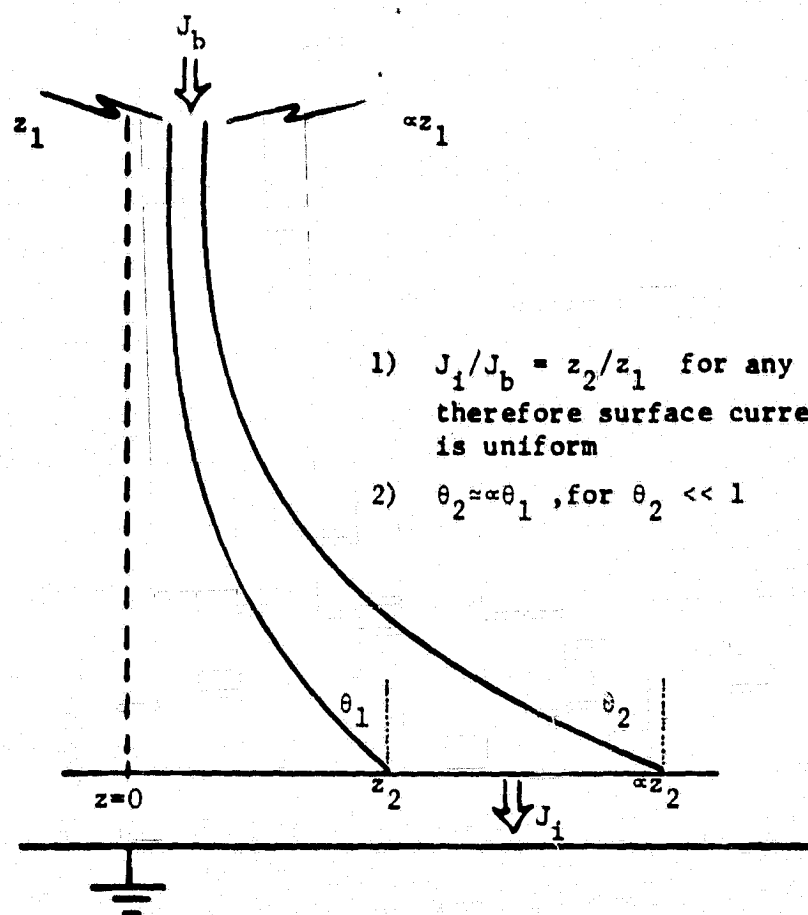


Fig. 5.1 Trajectory scaling results



in eq. 5.9.

$$J_1/J_b = \frac{g_1(0)(\alpha - 1)}{g_1(t_0)(\alpha - 1)} = \frac{g_1(0)}{g_1(t_0)} \quad (5.9)$$

for any scalar  $\alpha$

In addition since  $\dot{y}$  is fixed at the surface and  $\dot{z}$  is found to be proportional to  $z$ , the angle of impact for small angles will also be proportional to  $z$ .

Under symmetrical charging conditions the electrons incident at the centre of the sample will be directed normal to the surface. If the charging is emission-limited the central surface charge density can be calculated using eqs. 5.5 and 3.13.

$$\rho_0 = \pi \epsilon_0 (BE - KE_2) / (2d |e| \tan (w/d)) \quad (5.10)$$

where  $KE_2$  = unity emission energy for normal incidence

For  $w \gg d$  eq. 5.10 reduces to the expressions obtained in Chapter 3 (eqs. 3.5 and 3.13) describing a one-dimensional charging model.

The trajectories for different beam energies are closely related. For a surface potential (and hence a charge density) equal to specific fraction of the beam accelerating voltage the resulting trajectories will be invariant. If  $y_1, z_1$  describe a trajectory from a beam of energy  $BE_1$  onto a material with a surface potential equal to  $(k_0 BE_1/e)$  then a corresponding trajectory  $y_2, z_2$  exists for a beam energy  $BE_2$  and a surface potential  $(k_0 BE_2/e)$  such that (from eq. 5.5):

$$\text{given } (y_1^2 + w^2) \ddot{y}_1 = k_1$$

$$(y_2^2 + w^2) \ddot{y}_2 = k_1 BE_2 / BE_1 \quad (5.11)$$

where  $k_1$  = a constant

$$y_2(0) = y_1(0)$$

$$\dot{y}_2(0) = \sqrt{BE_2/BE_1} \dot{y}_1(0)$$

If we let  $y_2 = y_1(\sqrt{BE_2/BE_1} t)$  eq. 5.11 is satisfied along with the appropriate initial conditions. From eq. 5.6 and using  $y_2$  as above,  $z_2$  must be found such that:

$$\text{given } \ddot{z}_1/z_1 = f_1(t)$$

$$\ddot{z}_2/z_2 = BE_2/BE_1 f_1(\sqrt{BE_2/BE_1} t) \quad (5.12)$$

$$\text{where } z_2(0) = z_1(0), \dot{z}_2(0) = \dot{z}_1(0) = 0$$

Substituting  $z_2 = z_1(\sqrt{BE_2/BE_1} t)$  satisfies eq. 5.12. The resulting path  $y_2$ ,  $z_2$  is unaltered as both coordinates are affected by an identical time scaling. Using this result and calculating the incident current density as indicated in eq. 5.9 we are able to generate a universal set of curves describing the incident current density as a function of the surface potential, as can be seen in Fig. 5.2. The accuracy of the analysis becomes uncertain when the surface potential approaches the accelerating beam voltage as the paraxial approximation used is no longer applicable.

The angle of incidence at equilibrium as a function of beam energy is given in Table 5.1 for Teflon. The equilibrium trajectories are more strongly deflected for higher beam energies as the equilibrium surface potential represents a larger fraction of the accelerating beam voltage.

Table 5.2 presents the angle of incidence as a function of normalized coordinate  $z/w$ . The consistency of this value suggests a degree of width scaling is inherent in the equations of motion governed by eqs. 5.4, 5.5 and 5.6. If the trajectory  $y_1, z_1$  onto a sample of half width equal to unity is known, then it can be shown by direct substitution that  $y_2, z_2$  satisfy eqs. 5.5 and 5.6 for an arbitrary halfwidth  $w$  when

$$\begin{aligned} z_2 &= wz_1(t/w) \\ y_2 &= wy_1(t/w) \end{aligned} \quad (5.13)$$

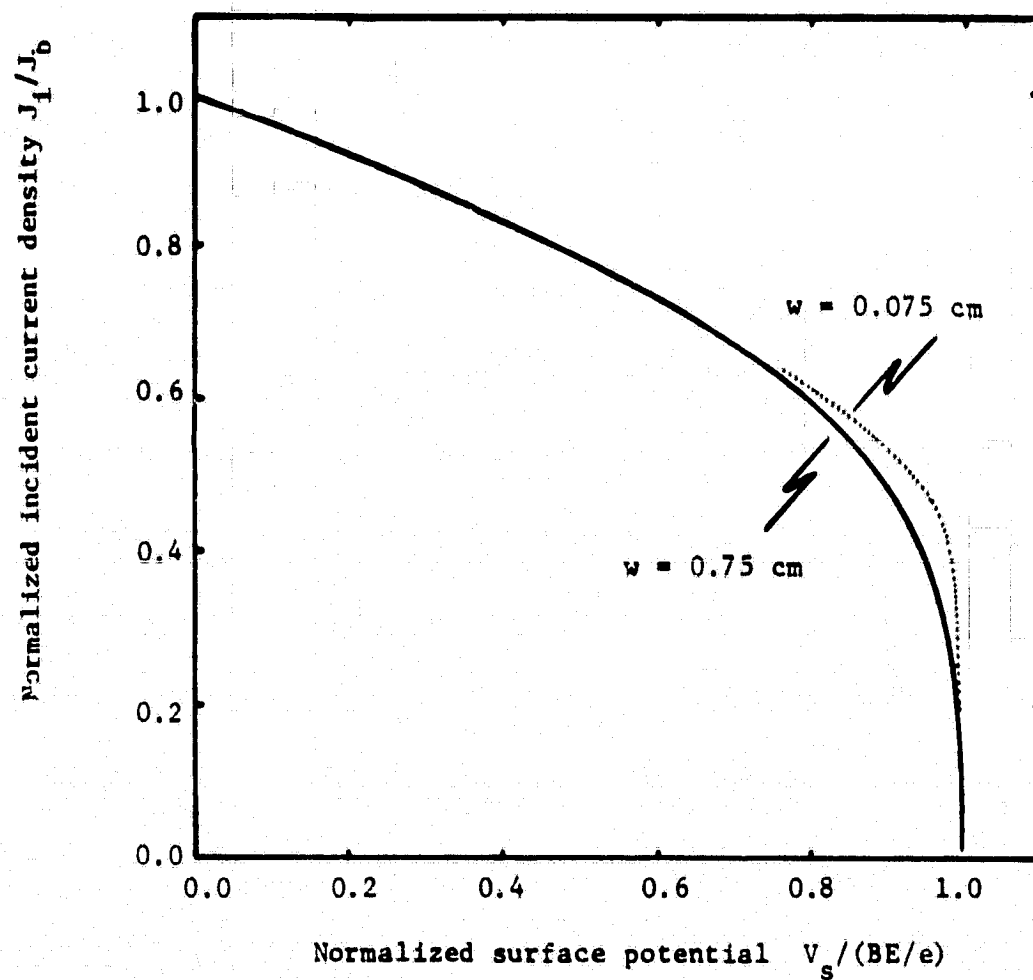


Fig. 5.2 Reduction of incident current density due to beam spreading

BEAM ENERGY (keV)	(eV <sub>s</sub> / BEAM ENERGY)	dθ <sub>1</sub> /dz (degrees/mm)
30	0.933	8.5
20	0.90	6.5
15	0.87	5.7
10	0.80	4.2
5	0.60	2.3

Table 5.1 Rate of change of the angle of incidence at steady state for Teflon (w = 0.75 cm).

MATERIAL HALFWIDTH (cm)	dθ <sub>1</sub> /d(z/w) (degrees)
0.75	42.7
0.375	42.2
0.1875	41.9

Table 5.2 Angle of incidence width scaling for Teflon at steady state (beam energy 15 keV).

with the following initial conditions:

$$\begin{aligned} z_2(0) &= wz_1(0) & y_2(0) &= y_1(0) = \infty \\ \dot{z}_2(0) &= \dot{z}_1(0) & \dot{y}_2(0) &= \dot{y}_1(0) \end{aligned}$$

If the material is very thin, we approximate the material's surface by the plane  $y = 0$  which implies

$$\begin{aligned} z_2/w \Big|_{y_2=0} &= z_1 \Big|_{y_1=0} \\ \dot{z}_2 \Big|_{y_2=0} &= \dot{z}_1 \Big|_{y_1=0} \\ \dot{y}_2 \Big|_{y_2=0} &= \dot{y}_1 \Big|_{y_1=0} \end{aligned} \tag{5.14}$$

At the material surface the energy of impact and hence the surface potential as well as the angle of impact can therefore be represented as universal functions of  $z/w$ .

The results in Fig. 5.2 were used to modify eq. 3.16 to account for the effect of beam spreading on the charging rates in Teflon.

$$\frac{tJ_b d}{\epsilon_0 \epsilon_r} = \int \frac{dV}{J_1/J_b (1 - BS - SE)} \tag{5.15}$$

where  $J_1/J_b$  is given in Fig. 5.2

The charging dynamics for beam energies from 5 - 25 keV based on eq. (5.15) and experimental data produced at Lewis Research Centre [Purvis et al, 1979] for Teflon are compared in Fig. 5.3. NASCAP predictions and Lewis Research Centre data are compared in Fig. 5.5 [Roche and Purvis, 1979]. Both numerical simulations, as well as those reported by Beers, [1980] tend to be slower than the Lewis Research Centre data. Purvis et al [1977] have also reported excessive leakage currents in Teflon implying an effective conductivity of

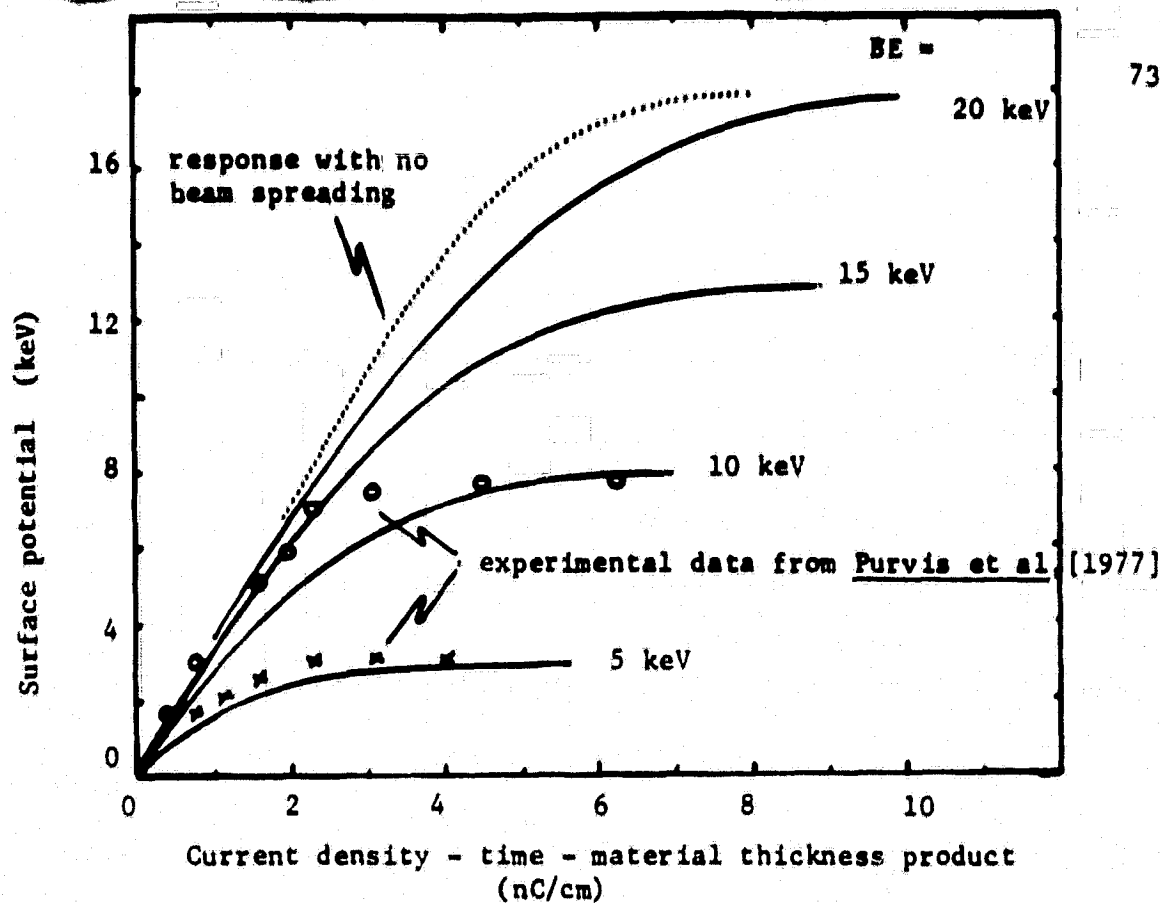


Fig. 5.3 Charging dynamics for Teflon with beam spreading.

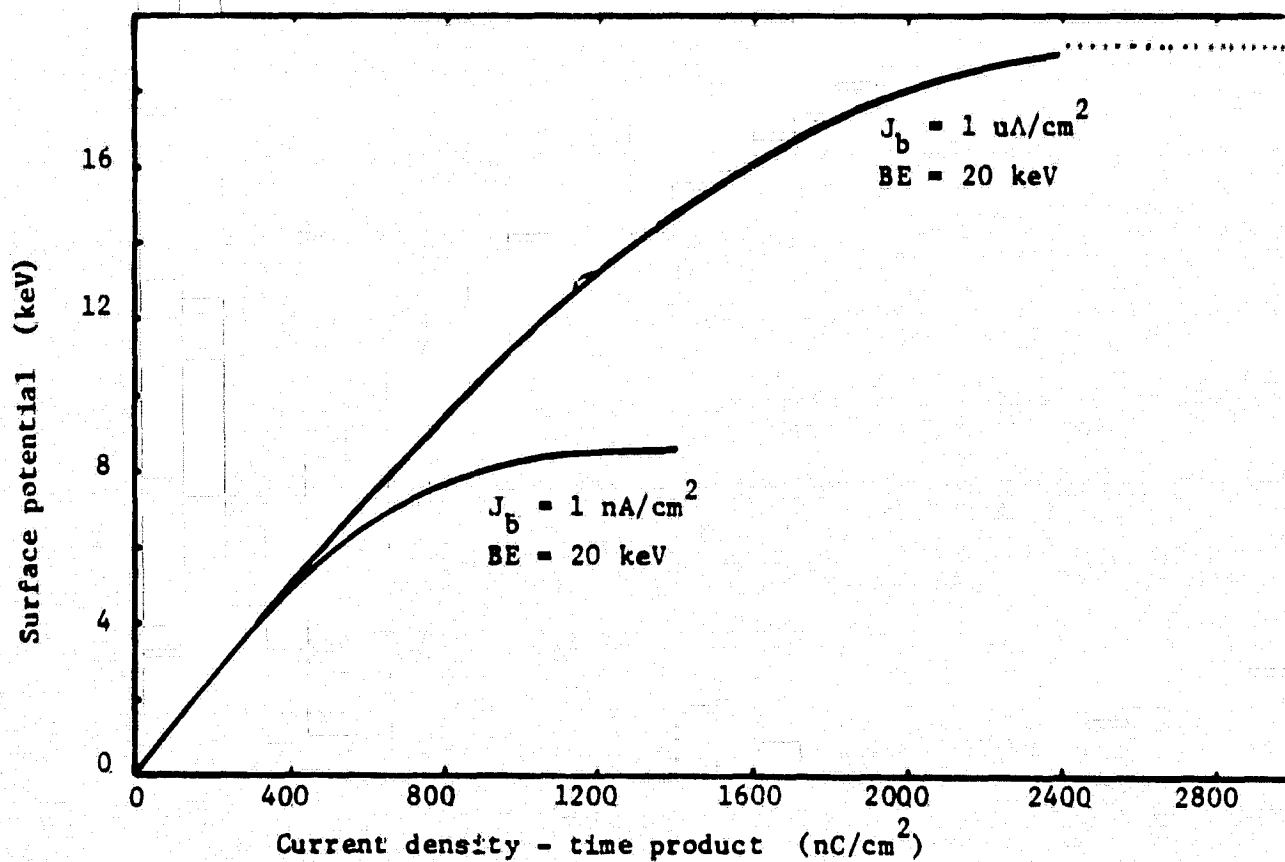


Fig. 5.4 Charging dynamics for Kapton with beam spreading.

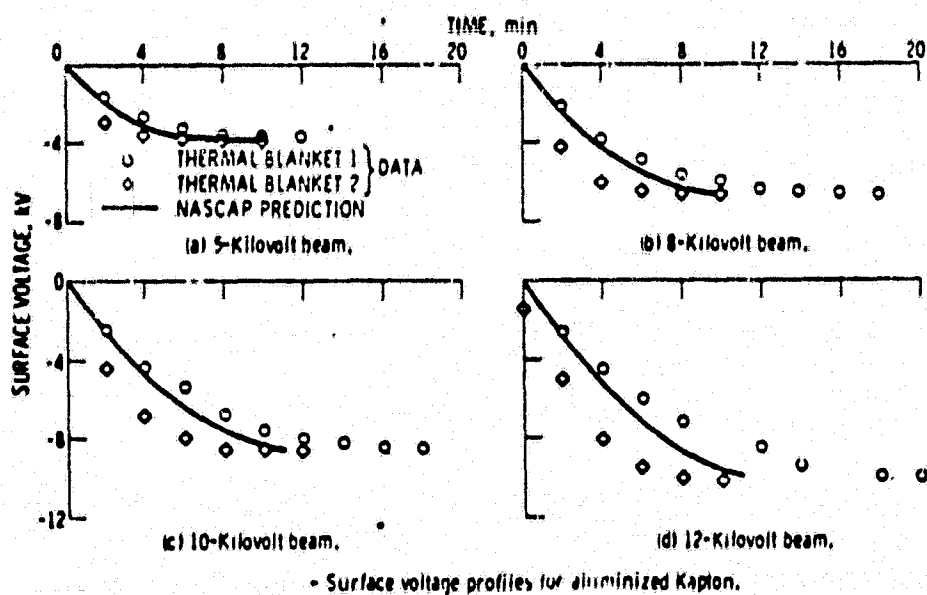
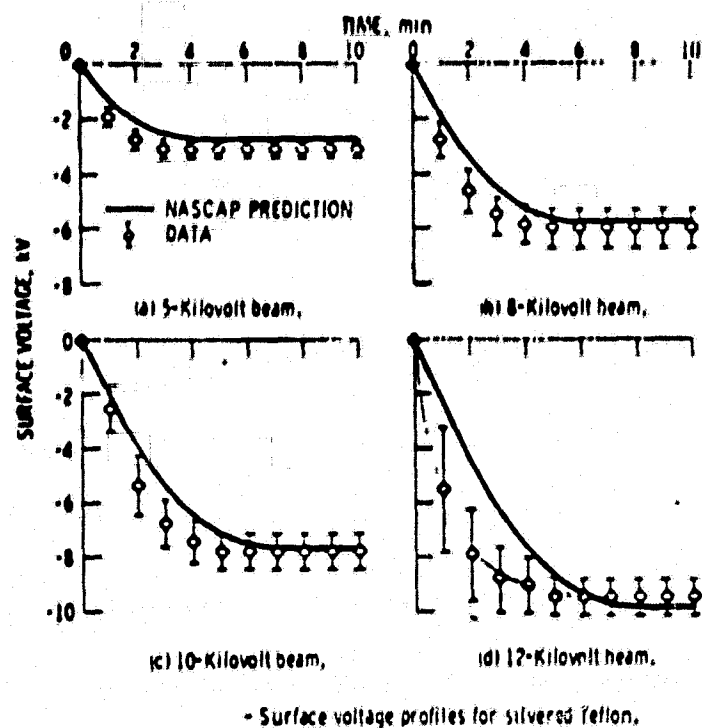


Fig. 5.5 Experimental data and NASACAP model results for Teflon and Kapton charging rates. Beam current density 1 nA/cm<sup>2</sup>. (from Roche and Purvis, [1979])

$10^{-16} (\Omega\text{cm})^{-1}$ . The authors list surface or edge leakage as possible parallel conducting paths to account for this observation.

Charging results incorporating beam spreading are presented in Fig. 5.4 for Kapton under conditions that support either emission or conduction-limited equilibrium. No dramatic departure is observed in the general qualitative behaviour of either curve from those already discussed.

Discharge studies [Balmain and Hirt, 1980] on 50  $\mu\text{m}$  thick Teflon irradiated by 20 keV electrons over a range of current densities  $0.5 - 50.0 \text{ nA/cm}^2$  have indicated typical waiting times between discharges range from 60.0 - 2.5 min. respectively. The corresponding range in the current density-time-thickness product is  $9.0 - 37.5 \text{ nC/cm}$ . Comparison with Fig. 5.3 suggests that discharges occur after the net charge accumulation process has reached a steady state.

## 5.2 Surface Fields

The electric fields above the surface of a charged dielectric are calculated to determine whether such fields could initiate a breakdown, particularly near the material edge, and to characterize the immediate environment in order to determine its effect on the emission processes. The tangential field is continuous in the vertical direction whereas the normal electric field is discontinuous at the surface as noted in eq. 4.12. Both fields reach a maximum in the neighbourhood of the edge.

For a uniform charge distribution the fields near the positive edge ( $z = w$ ) and near the surface ( $y = d$ ) can be calculated with the following definitions:

$$\Delta z = z - w$$

$$2w = z + w$$

$$\Delta y = y - d$$

$$2d = y + d$$



$$\begin{aligned} \text{where } \Delta_z &\ll w \\ \Delta_y &\ll d, \quad \Delta_y \geq 0 \\ d &\ll w \end{aligned}$$

The normal surface field outside the charge distribution can be calculated from eq. 4.8 and is plotted in Fig. 5.6 versus the horizontal displacement from the edge  $\Delta_z$  with the height above the surface  $\Delta_y$  as a parameter. The position and magnitude of the maxima can be determined to be

$$\Delta_z = \mp \sqrt{2d\Delta_y} \quad (5.17)$$

$$E_y = \rho_0/2\pi\epsilon_0(\pi/2 \pm d/w - \sqrt{2\Delta_y/d}) \quad (5.18)$$

The field strength is well behaved in that no singularity is encountered as the surface is approached. The actual charge distribution is not planar having a finite depth and an appropriate choice of  $\Delta_y$  must be made to account for this. Fortunately, for sufficiently thick samples the maximum field is insensitive to  $\Delta_y$ .

If we consider the charge distribution in Fig. 5.7 the edge normal field using eq. 4.8 is

$$\begin{aligned} E_y = & ((A + Bw)(d/w - \text{atan } \Delta_z/\Delta_y + \text{atan } \Delta_z/d) \\ & - Bd \ln((d^2 + \Delta_z^2)/w^2)) / 2\pi\epsilon_0 \end{aligned} \quad (5.19)$$

$$\text{where } A = (\rho_{\max} + \rho_{\min})/2 = \rho_{\text{avg}}$$

$$B = (\rho_{\min} - \rho_{\max})/2w$$

The normal electric field at the edge is reduced to zero when

$$\rho_{\min} = \rho_{\text{avg}}(1 - 1/(1 + 2\ln(w/d))) \quad (5.20)$$

For  $\rho_{\min}$  less than this value the zero crossing moves in from the edge towards the centre of the strip and the normal fields at the edge are reversed tending

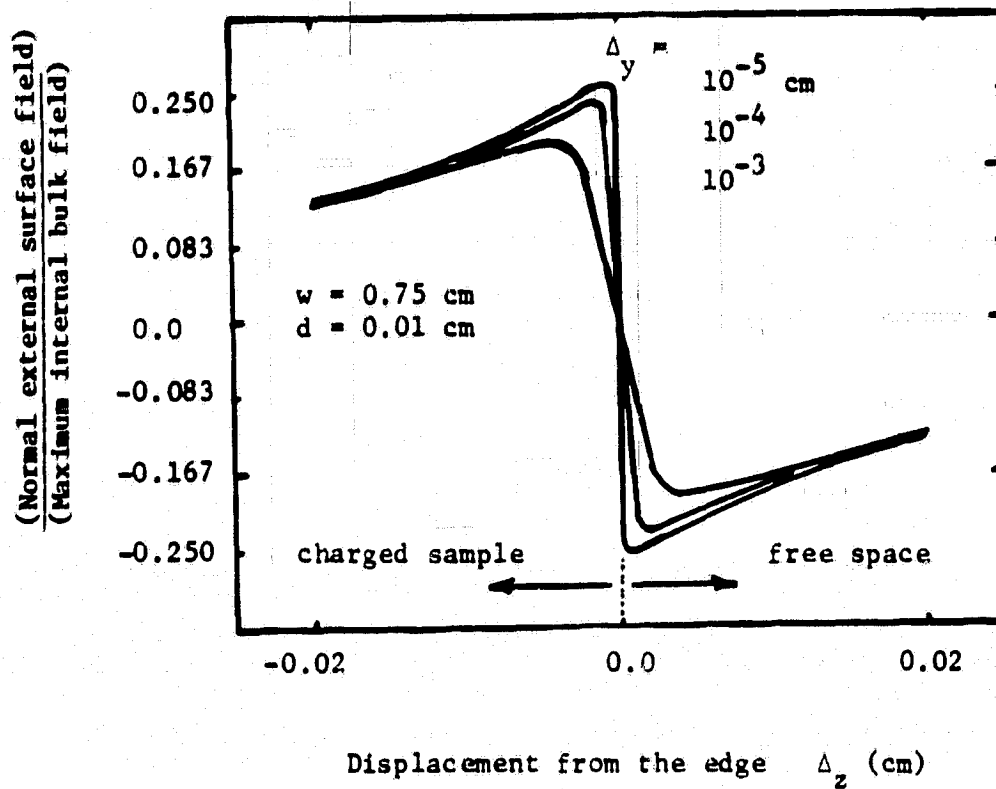


Fig. 5.6 Normal electric field near edge of uniformly charged sample.

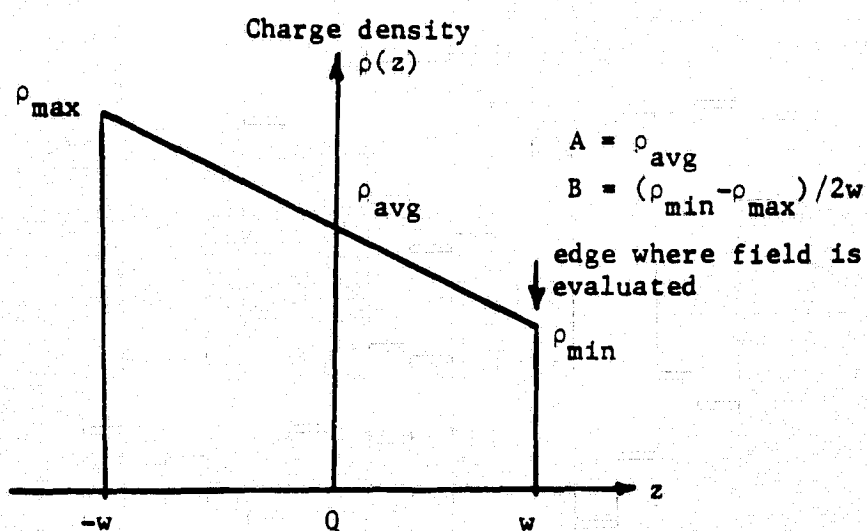


Fig. 5.7 Assumed charge distribution used to determine normal surface field sensitivity near edge.

to attract emission electrons back to the surface. For typical dimensions ( $w = 0.375$  cm,  $d = 0.01$  cm) the zero crossing coincides with the material edge when  $\rho_{\max}/\rho_{\min} = 1.28$ . If we increase the ratio to  $\rho_{\max}/\rho_{\min} = 3.0$  the surface normal field will be zero at  $\Delta_z = -0.165 \Delta_y$  (i.e. inside the edge). Since  $\Delta_y$  represents the actual depth of the volume charge distribution (of the order of microns) the section of material under field reversal is found to be very narrow for even large charge differentials. This coupled with strong edge tangential fields, to be described later in this section, suggest that the return of emission electrons to an isolated sample should be an insignificant effect.

For non-uniform specimens (where severe differential charging due to geometry or material composition could occur) the external fields can effectively eliminate the secondary emission and/or photo-emission process [Mandel et al, 1978]. This is particularly evident in the irradiation of strips of material possessing opposite charging characteristics (charging or non-charging) when placed alternately side by side. Figure 5.7 illustrates a subsection of such an array where the non-charging strips form gaps that are assumed to be at zero potential. The equipotential lines sketched above the surface suggest the development of a saddle point potential barrier representing a minimum energy requirement for an electron emitted from the gap to leave the surface. Since secondary emission and photo emission electrons tend to be low energy ( $\sim 10$  ev) these processes can be suppressed by a relatively low saddle point potential.

The potential above the centre of a grounded gap of width  $2w$  between two uniformly charged samples each of width  $2W$  can be calculated using eq. 5.1:

$$\phi(y) = -\rho_0 d / \epsilon_r (\text{atan}(w/y) - \text{atan}(w + 2W)/y) / (\pi/2) \quad (5.21)$$

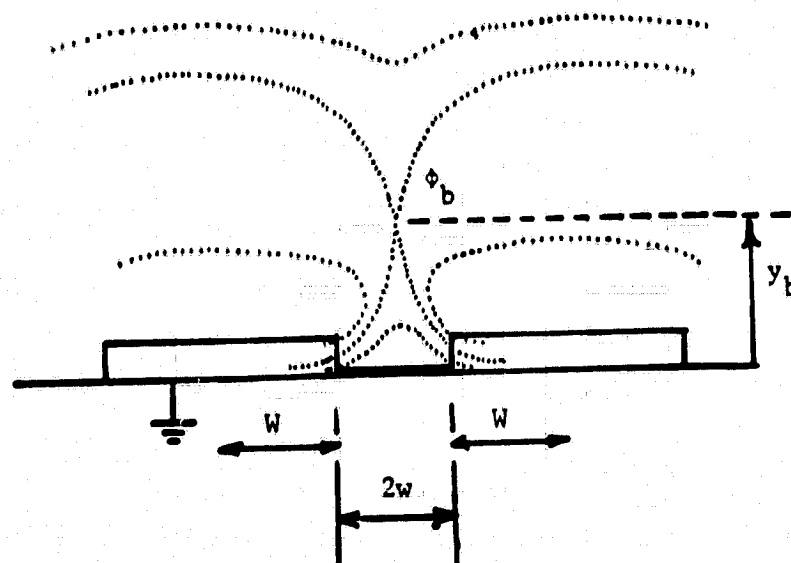


Fig. 5.8 Assumed geometry for potential barrier calculation.

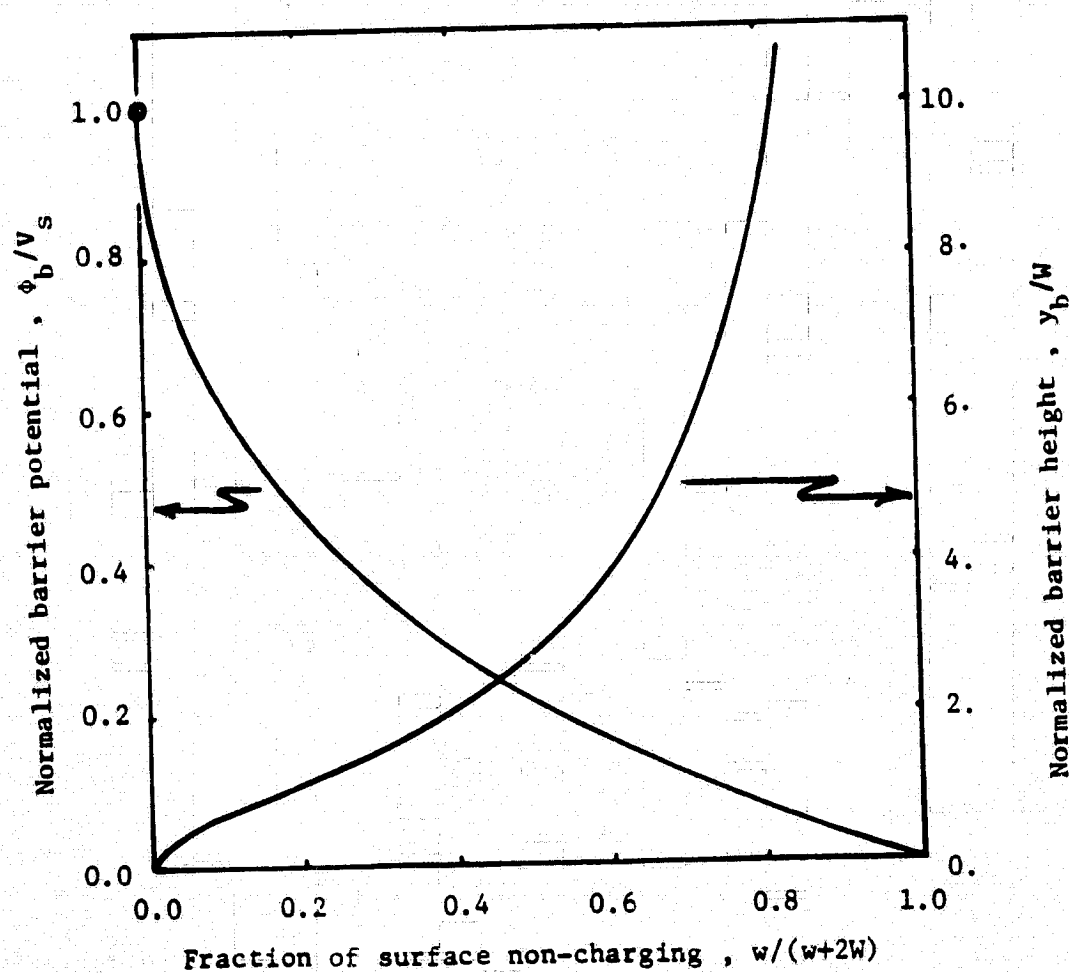


Fig. 5.9 Barrier potential dependence on geometry.

where  $\rho_0 d / \epsilon_0$  = surface potential at the centre of the charged elements

The saddle point is located by finding the root of the derivative of eq. 5.21

$$y_b = W \sqrt{2w/W + w^2/W^2} \quad (5.22)$$

where  $y_b$  = the height above the ground plane at which the saddle point is located

Substituting eq. 5.22 into eq. 5.21 the saddle point potential barrier can be calculated.

$$\phi_b = V(\text{atan } s - \text{atan } 1/s)/(\pi/2) \quad (5.23)$$

where  $\phi_b$  = potential barrier

$$s = \sqrt{1 + 2W/w}$$

$V$  = maximum surface potential

Equations 5.22 and 5.23 are plotted in Fig. 5.8. As the fraction of the total surface covered by the charging material is decreased the potential barrier is reduced in magnitude and moves away from the surface. Excellent agreement has been obtained between the above analysis and the NASCAP program results [Stannard et al, 1981].

The tangential field near the edge of a uniformly charged strip can be calculated using eq. 4.9 and has the following form:

$$E_z = \frac{\rho_0}{4\pi\epsilon_0} (\ln(\frac{2d^2 + \Delta_z^2}{\Delta_y^2 + \Delta_z^2}) - \ln(1 + (d/w)^2)) \quad (5.24)$$

Note as both  $\Delta_z$  and  $\Delta_y$  approach zero the tangential surface field has a logarithmic singularity. The maximum field is located directly above the edge ( $\Delta_z = 0$ ) and is given by

$$E_z = \rho_0 / 2\pi\epsilon_0 (\ln(2d/\Delta_y) - 1/2 \ln(1 + (d/w)^2)) \quad (5.25)$$

If we assume that instead of a planar charge layer there exists a uniform volume charge distribution of depth  $r$ , then the maximum tangential field can be obtained by integrating eq. 5.25 with respect to  $\Delta y$ . The resultant edge field at the centre of the charge distribution is

$$E_z = \rho_0 / 2\pi\epsilon_0 (\ln 4d/r + 1 - 1/2 \ln(1 + (d/W)^2)) \quad (5.26)$$

For sufficiently thick samples eqs. 5.26 and 5.25 are the same if we choose  $\Delta y = r/5.5$ . Since the details of the internal charge distribution are not known we have adopted the convention that all "surface" fields will be evaluated at  $\Delta y = 0.01 d$ . Rescaling of our results for an alternative charge distribution can be accomplished using eq. 5.25.

## 6. TWO-DIMENSIONAL NUMERICAL RESULTS AND DISCUSSION

The numerical results have been chosen to illustrate the charging response to a variety of geometries and beam characteristics. The Teflon simulations were assumed to be emission-limited and therefore independent of beam current density. A standard current density of  $50 \text{ nA/cm}^2$  was selected for these runs. Data was accumulated at 160 points across the surface. Trajectory calculations were made with a nearest-neighbour spacing ranging between 0.25% and 5.0% of the total sample width, typically requiring 50 trajectories per iteration, with a maximum resolution being obtained in the neighbourhood of the material edges. Standard runs required 8 min. of CPU time on the University of Toronto Computing Services' IBM 3033. The piecewise linear charge approximation was chosen to have a root mean square error less than 1.5% of the average charge density.

Under symmetrical charging conditions the expected solution symmetry was not incorporated into the charging model. Instead the full surface was represented so that asymmetric discrepancies can be used as a measure of the model's reliability.

The net charge density refers to the net negative charge in the sample. The surface charge density refers to the accumulation of an assumed positive charge layer on the material surface due to secondary emission. The surface fields refer to fields calculated a distance  $0.01 d$  above an assumed planar (zero-thickness) distribution of net charge.

### 6.1 Beam Energy Dependence for Teflon

The equilibrium net charge profiles for Teflon irradiated with beam energies ranging from 5 to 25 keV in 5 keV steps are given in Fig. 6.1 (material half width 0.75 cm, material thickness 100  $\mu\text{m}$ ). In Fig. 6.2 the equivalent charge in free space as described by eq. 4.6 is presented. In general, the internal normal bulk field is much larger than the

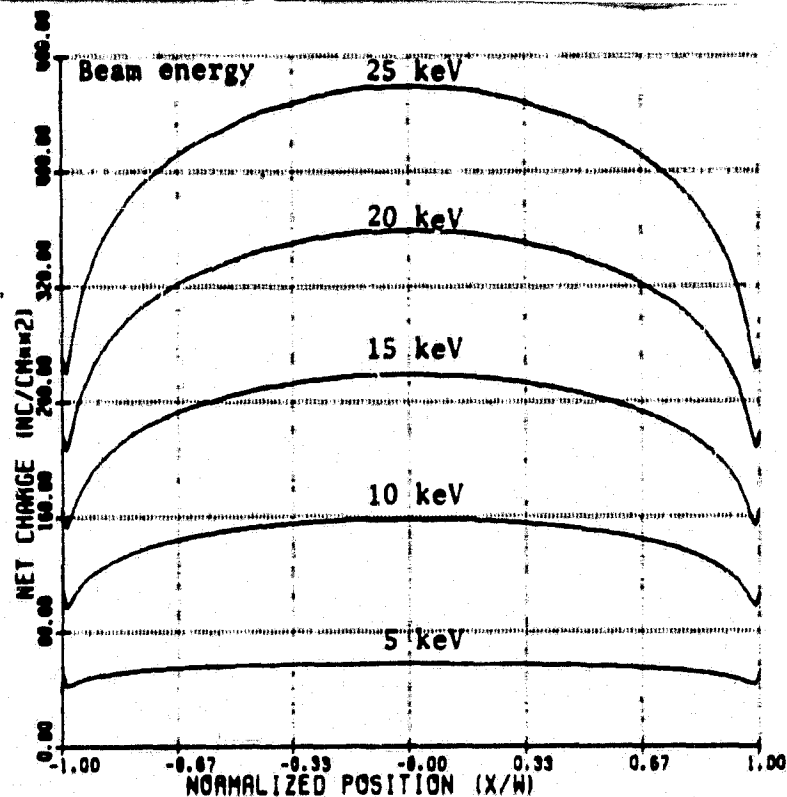
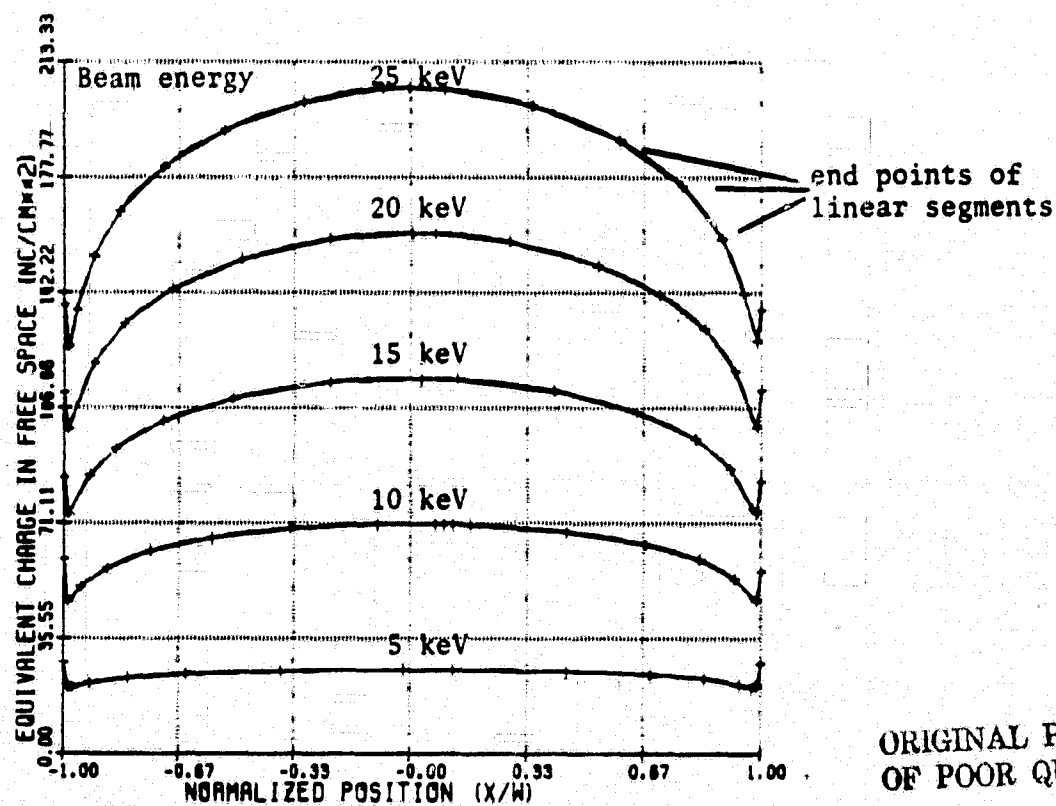


Fig. 6.1 Equilibrium surface charge density distributions for Teflon.



ORIGINAL PAGE IS  
OF POOR QUALITY

Fig. 6.2 Equilibrium equivalent surface charge distributions in free space and piecewise linear approximations used in field calculations.



external normal surface field and the equivalent charge is therefore approximately equal to  $1/\epsilon_r$  of the actual charge. The scales in Figs. 6.1 and 6.2 differ by a factor of  $1/\epsilon_r$  in order to facilitate this comparison. The crosses in Fig. 6.2 represent the end points of the linear segments used to approximate the effective charge density for the purpose of making field calculations.

The charging dynamics are illustrated by comparing intermediate stages in the evolution of the net charge in Figs. 6.3, 6.4 and 6.5 for beam energies of 20, 10 and 5 keV respectively. The vertical scales in these figures were chosen to be nearly inversely proportional to the beam energy. To a first approximation the curves for beam energies greater than 10 keV have the same shape indicating that a rather simple beam energy scaling of the equilibrium charge distribution is applicable to the entire surface. A more quantitative analysis in Fig. 6.6 suggests that the equilibrium charge density across the sample is proportional to  $(BE-k)$  where  $k$  is a function of position on the surface. At the centre  $k$  is equal to the second total emission crossover energy at normal incidence (2.1 keV for Teflon) as suggested by eq. 3.13. The value of  $k$  is approximately constant over central portion of the surface and reaches a minimum of 1.05 keV near the edges.

The charging dynamics at the edges differ considerably from those at the centre where the net charge density monotonically approaches a steady state in a manner consistent with eq. 5.15. At the edges the charge density overshoots its equilibrium value. This is illustrated in Fig. 6.7 where the temporal behaviour of the charge density at the centre and edges is explicitly presented for a 20 keV charging beam. Comparison with the predicted centre response from Fig. 5.3 indicates excellent agreement. The overshoot at the edges tends to increase with increasing beam energy.

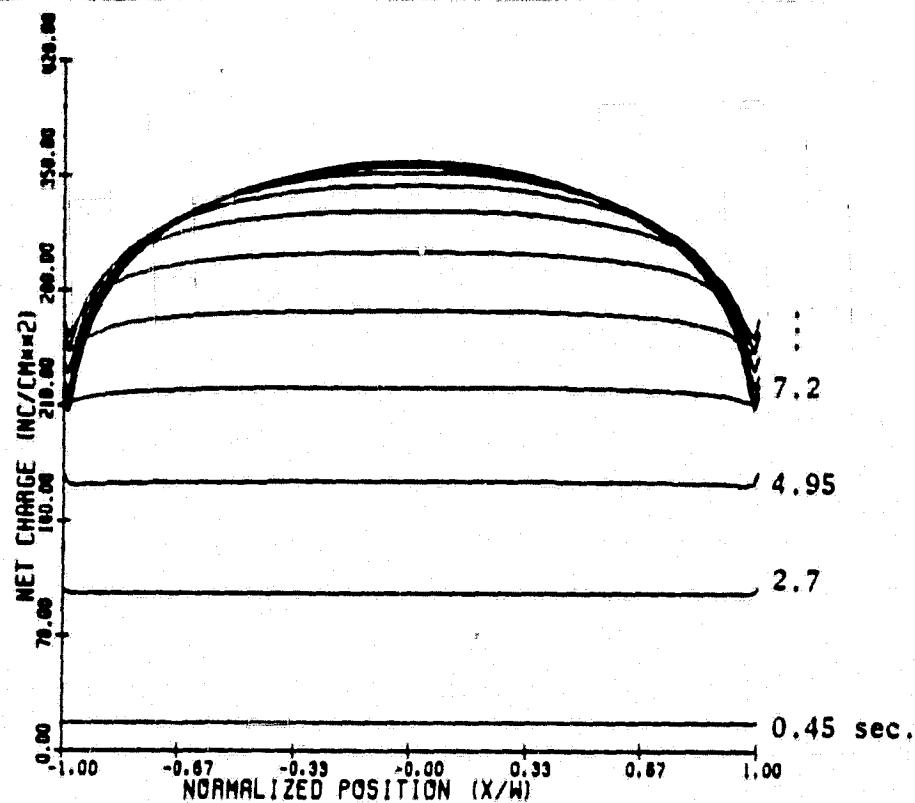


Fig. 6.3 Charging dynamics for Teflon. Beam energy 20 keV.  
Beam density 50 nA/cm².

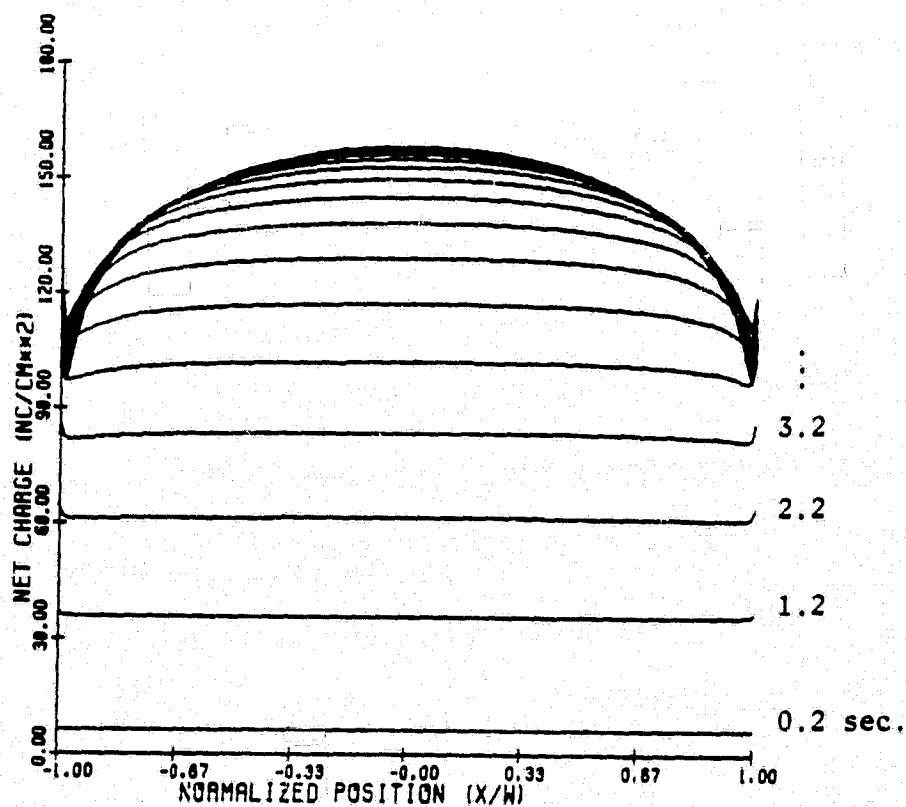


Fig. 6.4 Charging dynamics for Teflon. Beam energy 10 keV.  
Beam density 50 nA/cm².

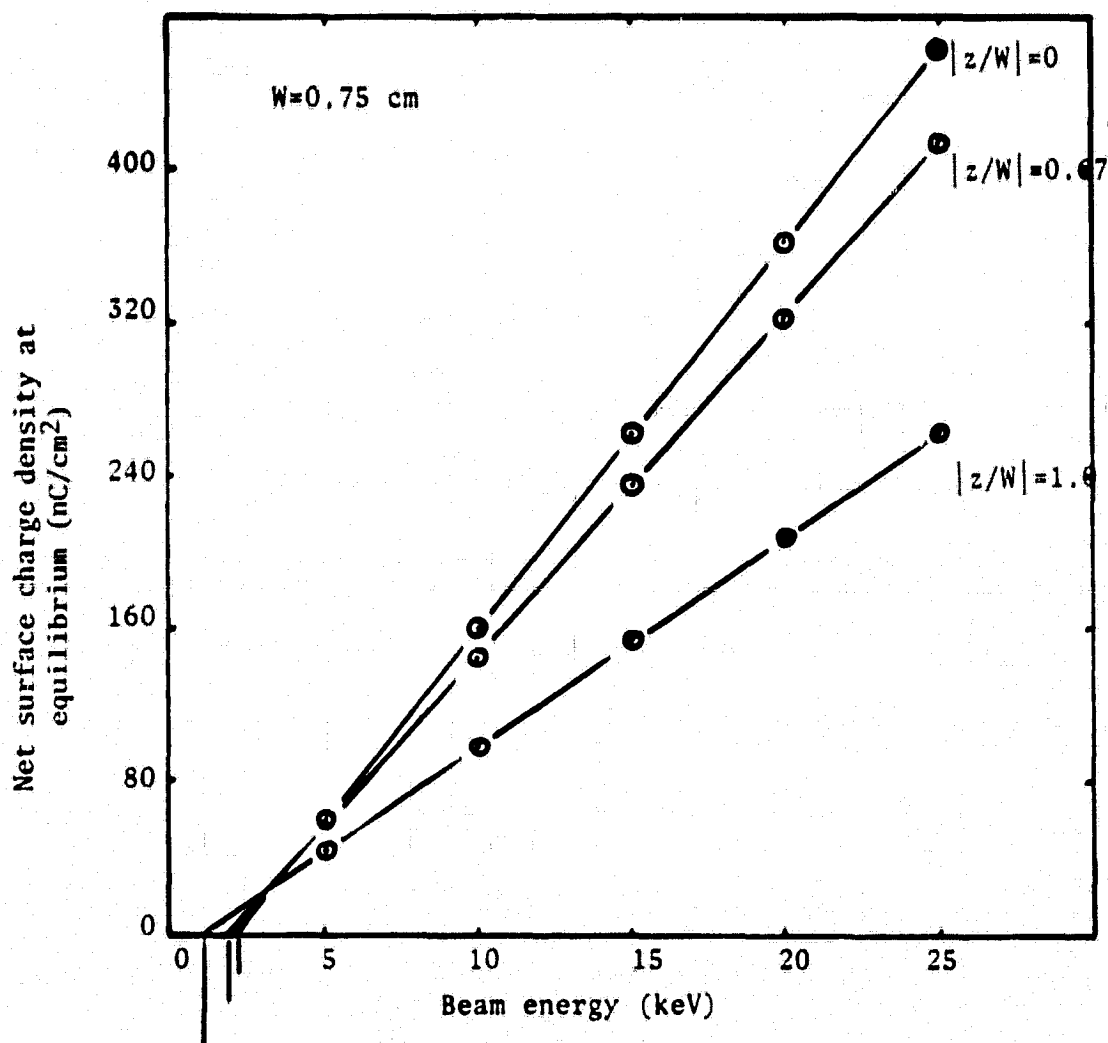


Fig. 6.6 Charge density vs. beam energy at three points on the exposed Teflon strip.

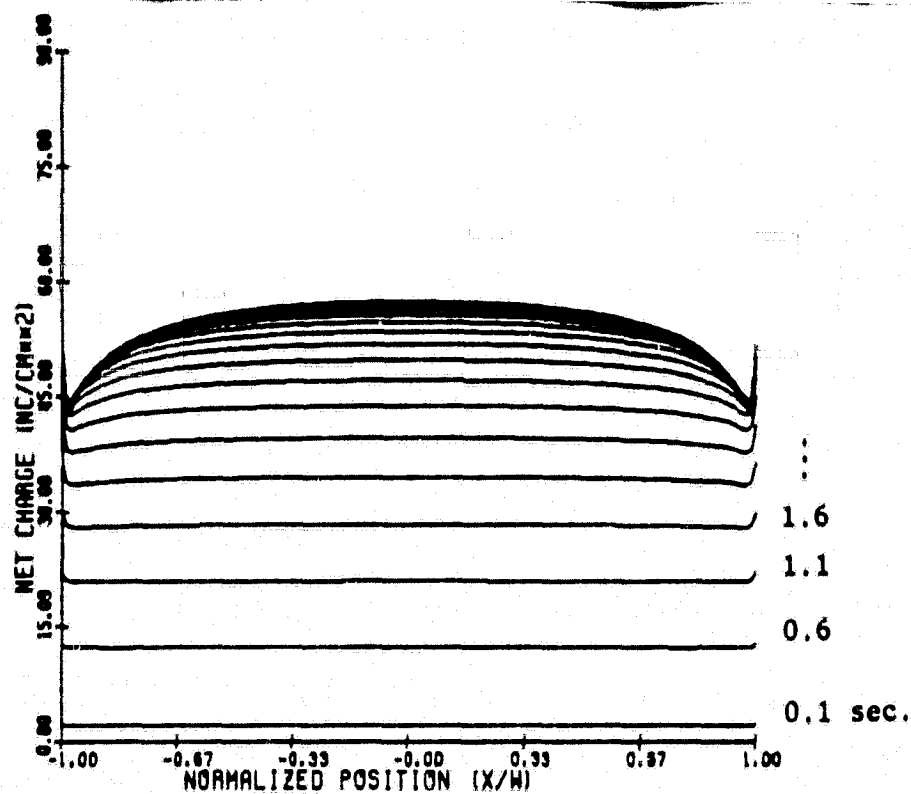


Fig. 6.5 Charging dynamics for Teflon. Beam energy 5 keV.  
Beam density 50 nA/cm<sup>2</sup>.

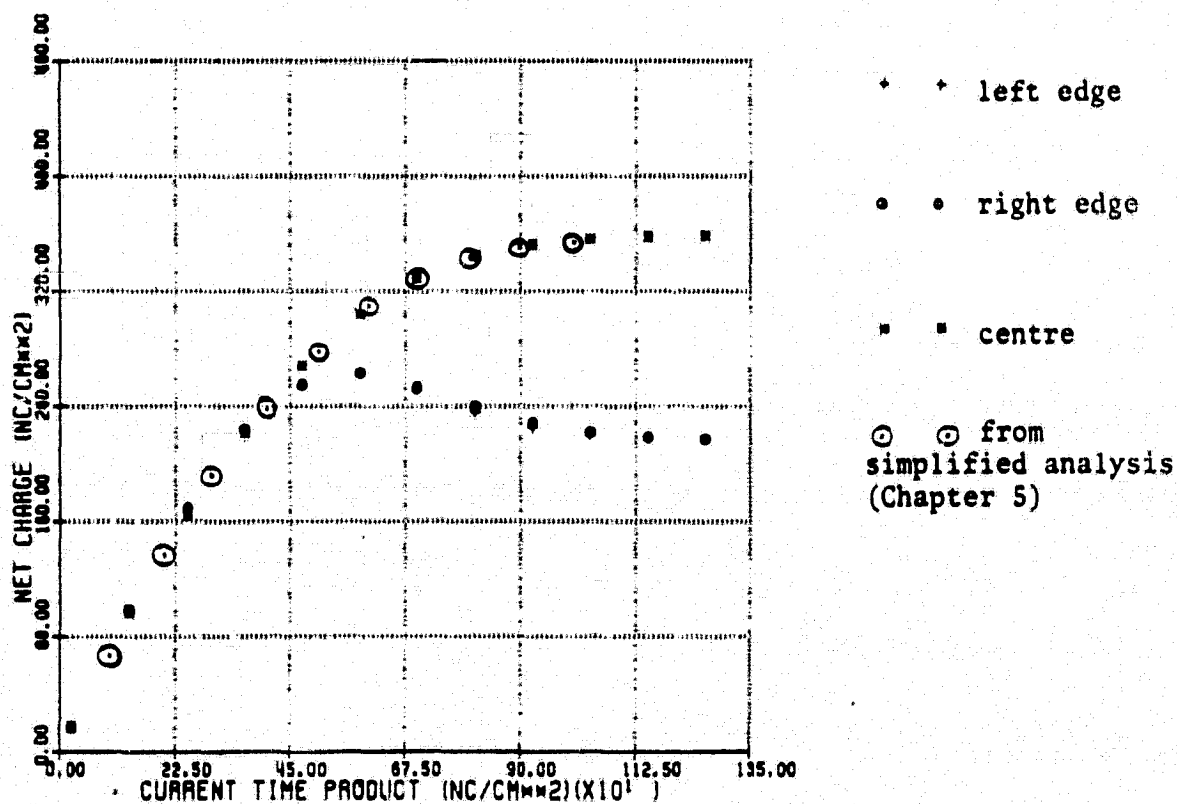


Fig. 6.7 Explicit time response at centre and edge of sample.  
Beam energy 20 keV.

A possible explanation for this behaviour is presented in a discussion of the necessary equilibrium conditions later in this section.

The steady state surface potential distribution for each beam energy is presented in Fig. 6.8. At higher beam energies the equilibrium surface potential becomes less uniform as the surface charges to a larger fraction of the beam accelerating voltage and the beam is more strongly deflected. Surface potentials measured by Robinson [1977] and Stevens et al [1978] are also presented in Fig. 6.8. Considering the uncertainty in the experimental points as well as the differences between the physical and model geometry the agreement is quite good.

The angle of impact in Fig. 6.9, as suggested in Chapter 5, displays a near linear central region, particularly for the lower beam energies, which increases in slope for increasing beam energies. In general the slope is larger than that found in Table 5.1; the reason may be that the non-uniform charge distribution tends to increase the tangential fields and enhance the degree of beam spreading.

The angle of impact is closely associated with the surface potential through the current balance in eq. 3.10 and the conservation of energy expressed in eq. 3.9

$$KE + |eV| = BE$$

for emission-limited equilibrium

$$J_1(1 - BS - SE) = J_c \approx 0$$

therefore

$$BS(KE, \theta) + SE(KE, \theta) = 1 \quad (6.1)$$

where  $KE, \theta$  and  $V$  are unknown

An explicit relationship between the equilibrium kinetic energy and the angle of impact is given in Fig. 6.10 for a

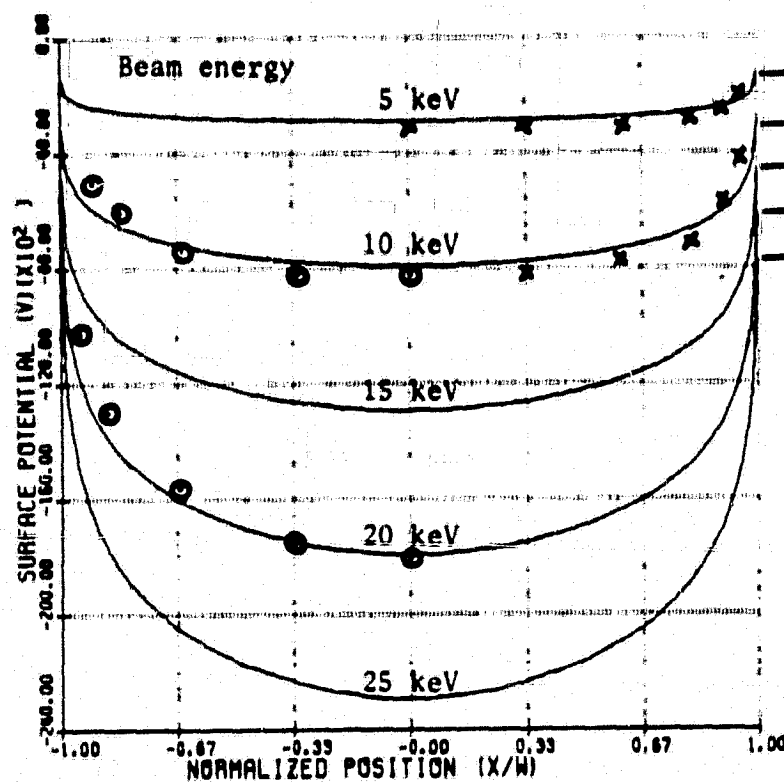


Fig. 6.8 Equilibrium surface potential distributions for Teflon.

- ✕ experimental data points from Stevens et al., [1978]  
(experiment: Teflon strips 0.013 cm thick, halfwidth 5.0 cm)
- experimental data points from Robinson, [1977]  
(experiment: circular Teflon samples 0.013 cm thick defined by an aperture 2.5 cm in diameter cut in a 1.3 mm aluminum plate placed in contact above the material)

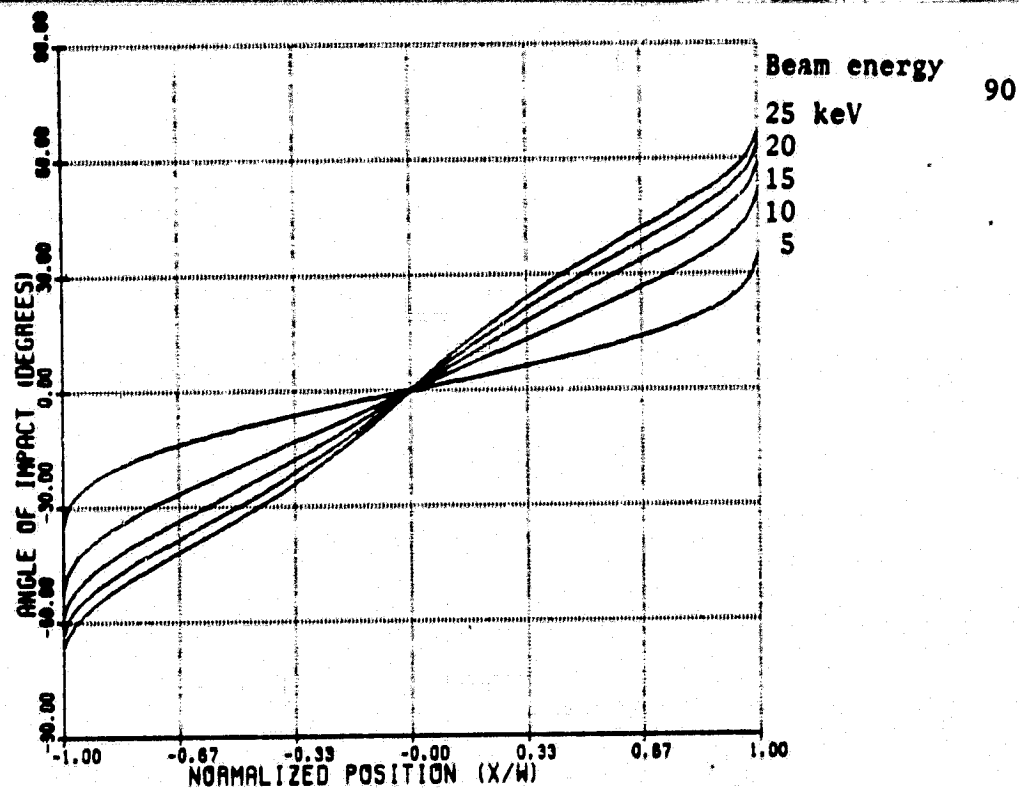


Fig. 6.9 Angle of incidence at equilibrium.

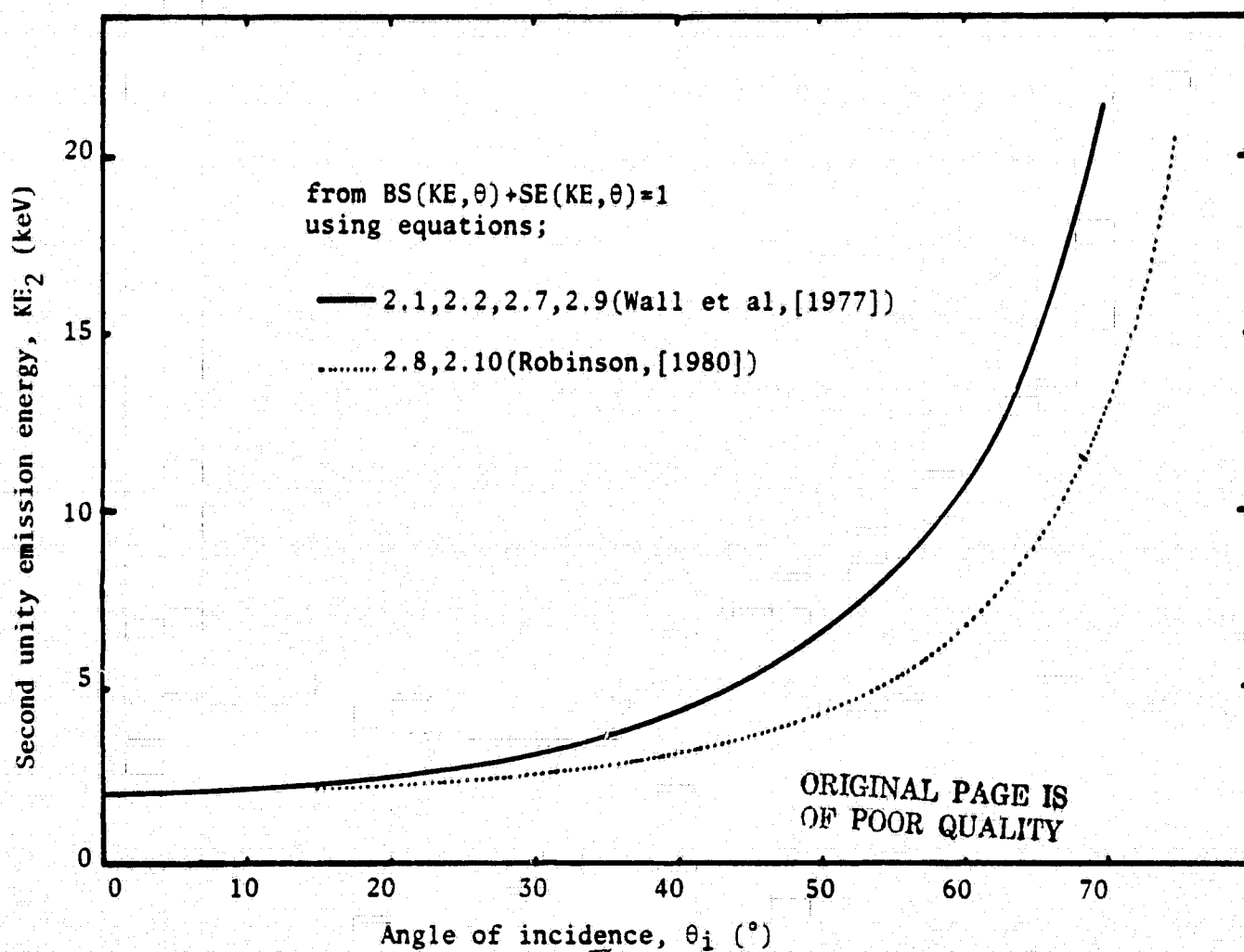


Fig. 6.10 Unity emission energy vs. angle of incidence at equilibrium for Teflon.

C-2

total emission coefficient as described by Wall et al [1977] (eqs. 2.1, 2.2, 2.7 and 2.9) and as described by Robinson and Budd [1980] (eqs. 2.8 and 2.10). Had the angular dependence suggested by Robinson (eq. 2.10) been used in the computer simulation the central region of the sample would have been more uniform. Figs. 6.8 and 6.9 compare favourably with the predicted relationship in Fig. 6.10.

The charging dynamics can be explained in terms of the relationship between the surface potential and the angle of impact. As the sample begins to charge the beam is largely undeflected and a uniform charge distribution is developed. However, as the surface potential approaches the accelerating beam voltage the angle of impact at the edges reaches a level (approximately  $50^\circ$ ) where the associated local equilibrium potential begins to drop significantly, forcing a loss of charge primarily through an increase in the secondary emission coefficient from the edge. This loss of charge enhances the tangential fields thereby maintaining a large angle of incidence. As a result the charge density at the edge collapses as the potential at the centre nears the beam voltage. Since a 5 keV beam charges Teflon to a maximum surface potential of approximately 3 kV (representing only 60% of the accelerating voltage) an overshoot does not develop and the resulting charge and surface potential distributions are more uniform.

The external normal surface field, external tangential surface field and the internal normal bulk field distributions are given in Figs. 6.11, 6.12 and 6.13 respectively. The maxima obtained by the external normal surface fields are in general less than that required for dielectric breakdown. The edge surface tangential field and the central internal normal field are comparable both exceeding  $10^6$  V/cm for the 20 keV and 25 keV beams. For a strip width of 1.5 cm the tangential field maxima are 60% smaller than the peak internal bulk field.



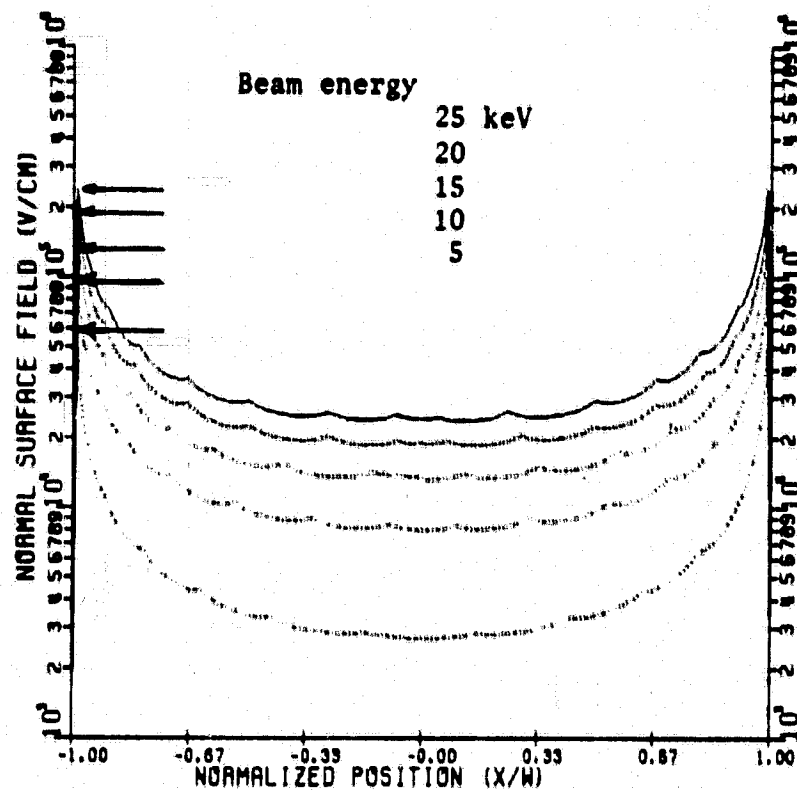


Fig. 6.11 External normal surface field distributions at equilibrium.

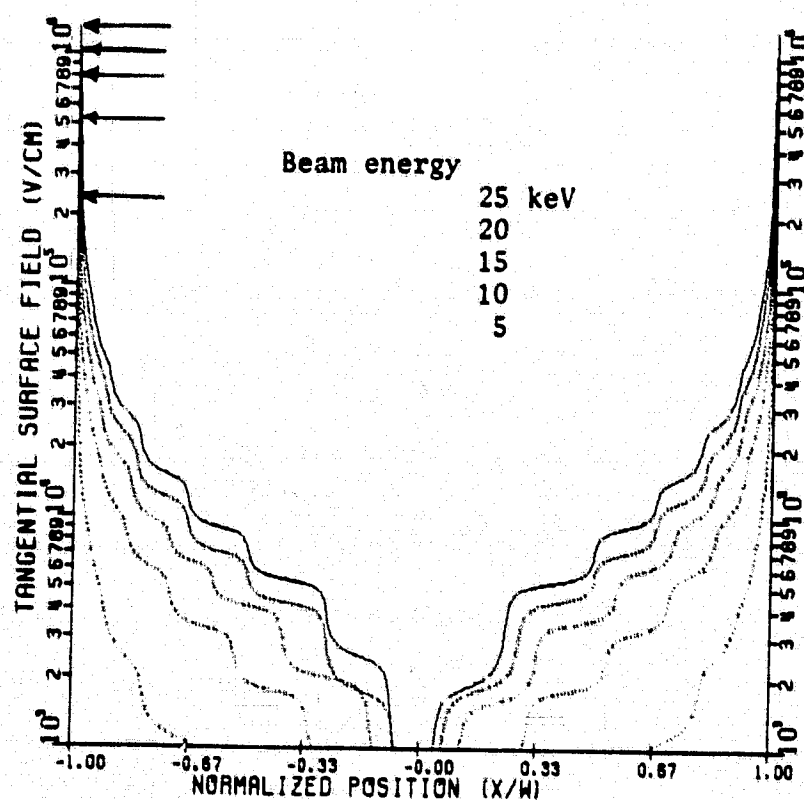


Fig. 6.12 External tangential surface field distributions at equilibrium.

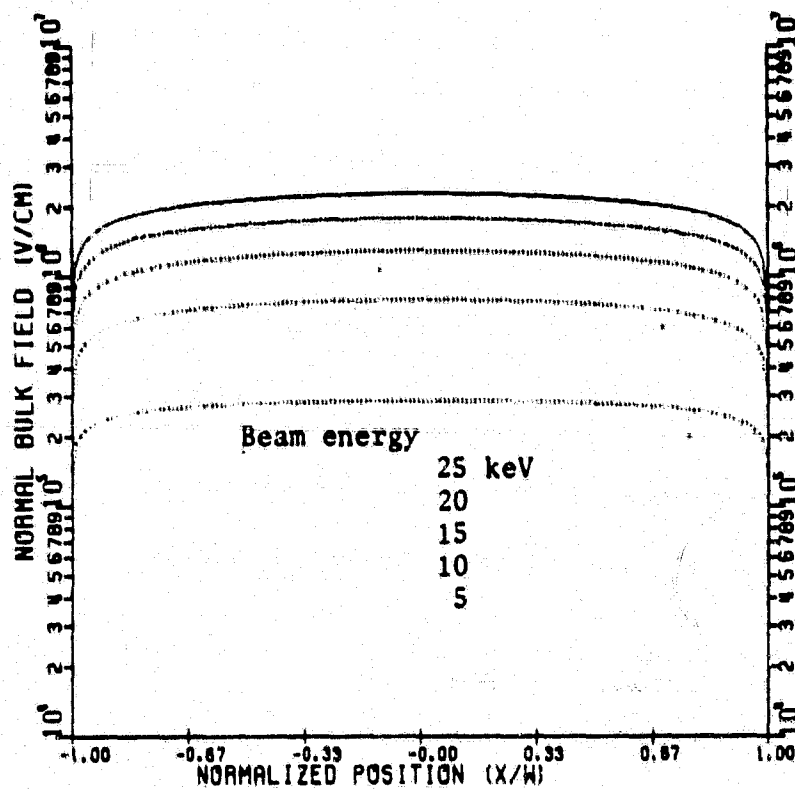


Fig. 6.13 Internal normal bulk field distributions at equilibrium.

The strong peak in the tangential field has a half-maximum width of the order of the sample's thickness. As indicated by eq. 5.25 the peak tangential field is influenced by the assumed internal volume charge distribution and is therefore subject to some uncertainty. In many experimental setups the sample is also covered by a grounded metal aperture plate which could enhance the peak surface tangential component at the edge.

The tangential field calculated at  $y = d/2$  (halfway through the material) is approximately  $1/5$  the magnitude of the surface tangential component. The undulations in the surface fields are due to the discontinuities in the slope of the piecewise linear charge representation. The actual quantities plotted in Figs. 6.11, 6.12 and 6.13 are the magnitude of the various field components. The direction of the tangential field should be understood to be towards the centre of the strip and passes through a zero at that point.

The paths traced by low energy secondaries emitted from the surface charged to equilibrium by a 20 keV beam are approximated in Fig. 6.14. The electrons are assumed to be emitted normal to the surface with an energy of 1.0 eV. A small fraction (approximately 7%) are found to be turned back to the ground plane. Experiments performed by Cuchanski [1978], in which an electron microscope was used to image the secondary emission occurring from a charged dielectric, indicated a band near the grounded metal edge from which no secondaries reached the detector. The band measured approximately 9% of the sample radius in good agreement with the predicted behaviour. The blowoff electrons during the discharge event cannot be inferred from Fig. 6.14 due to severe space charge limiting that has been ignored in this treatment [Stettner, 1980; Katz, 1980]. Measurements made by Balmain and Hirt [1980] indicate that the fraction of the released charge returning to the ground plane is increased to approximately 50% during the discharge event.

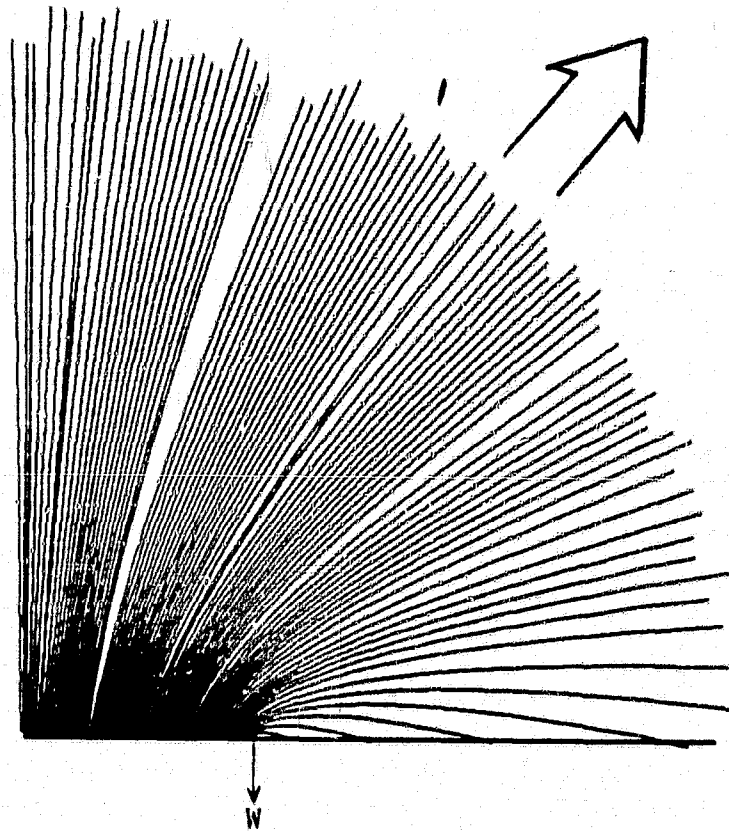


Fig. 6.14 Trajectories of electrons emitted normally from the surface at equilibrium with low kinetic energy ( $\sim 1$  eV) (charging beam density 20 keV)

Figures 6.15, 6.16 and 6.17 indicate the incident current density profile, the dose rate profile and incident trajectories taken at steady state for the sample charged by a 20 keV beam. The normalized current density has a broad minimum of 0.53 at the centre of the strip and maxima at the edges of 0.7. The central current density is in good agreement with the simplified analysis presented in Fig. 5.2. The dose rate is remarkably flat considering the variation in its constitutive parameters: angle of incidence, surface potential and current density, as given by the formula

$$\dot{D} \propto J_1 / \cos\theta \text{ KE}^{-0.358}$$

which is derived from eqs. 2.12, 2.13 and 2.14.

The internal front face field is presented in Fig. 6.18. The equilibrium field is governed by the relationship (eq. 3.26)

$$E_{ff} = -J_{se}/g$$

It was demonstrated (eq. 3.27) that this quantity is a rather weak function of incident current density and impact energy so the uniformity of the two-dimensional results should not be too surprising. The magnitude of the field agrees quite well with that predicted in Chapter 3 when the degree of beam spreading is taken into account.

$$|E_{ff}| = (J_1)^{0.3} 6.1 \times 10^3 \text{ V/cm}$$

$$J_1 = J_b \cdot 0.53 \text{ where } J_b = 50 \text{ nA/cm}^2$$

therefore the one-dimensional prediction is

$$E_{ff} = 1.64 \times 10^4 \text{ V/cm}$$

The surface charge layer required by Gauss' Law to match the internal front face field and the external normal surface field in Fig. 6.18 and Fig. 6.11

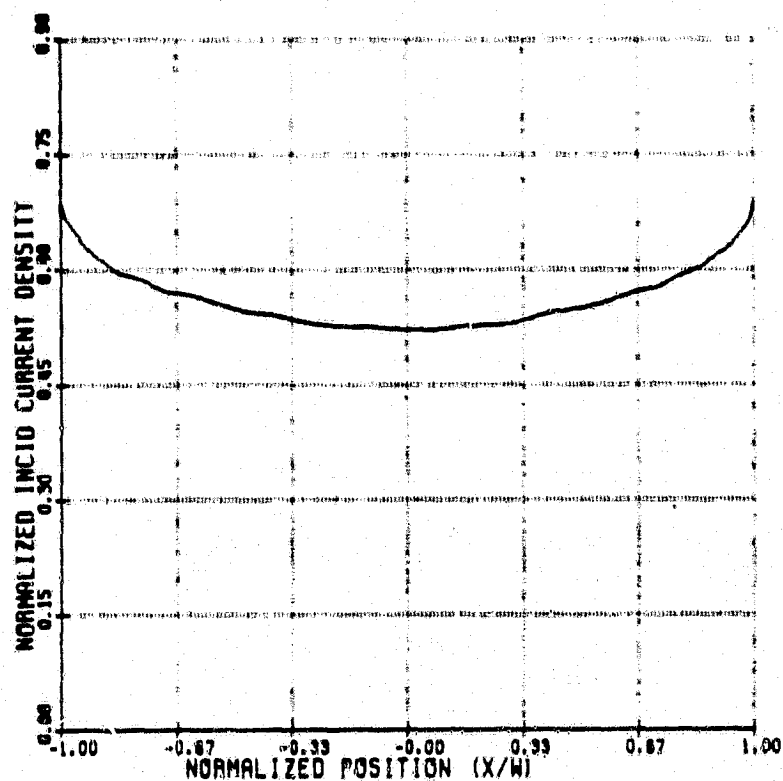


Fig. 6.15 Reduction in incident current density due to beam spreading at equilibrium. Beam energy 20 keV.

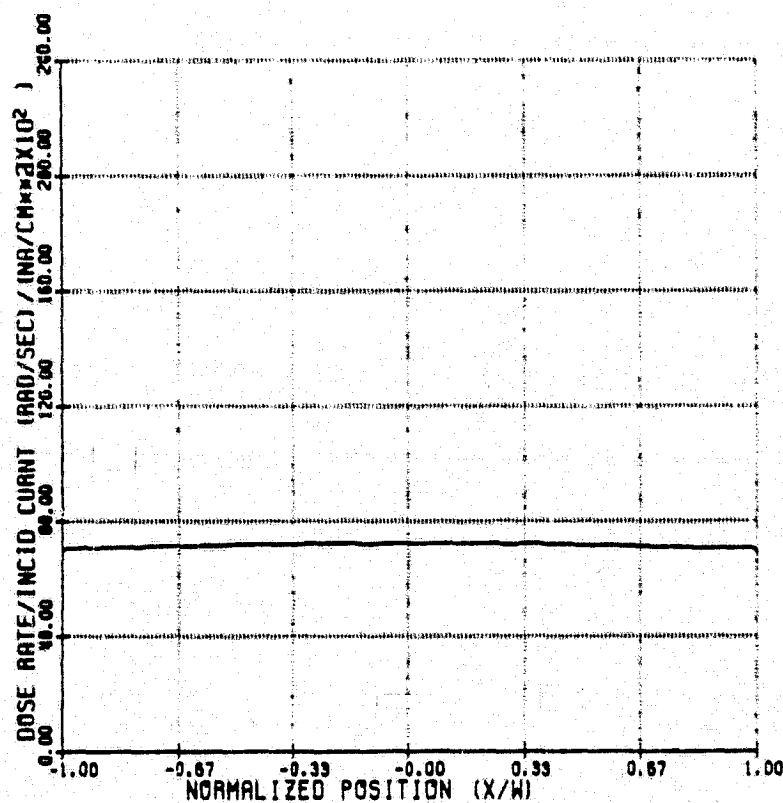


Fig. 6.16 (Dose rate/beam current density) distribution at equilibrium for Teflon charged by a 20 keV beam.

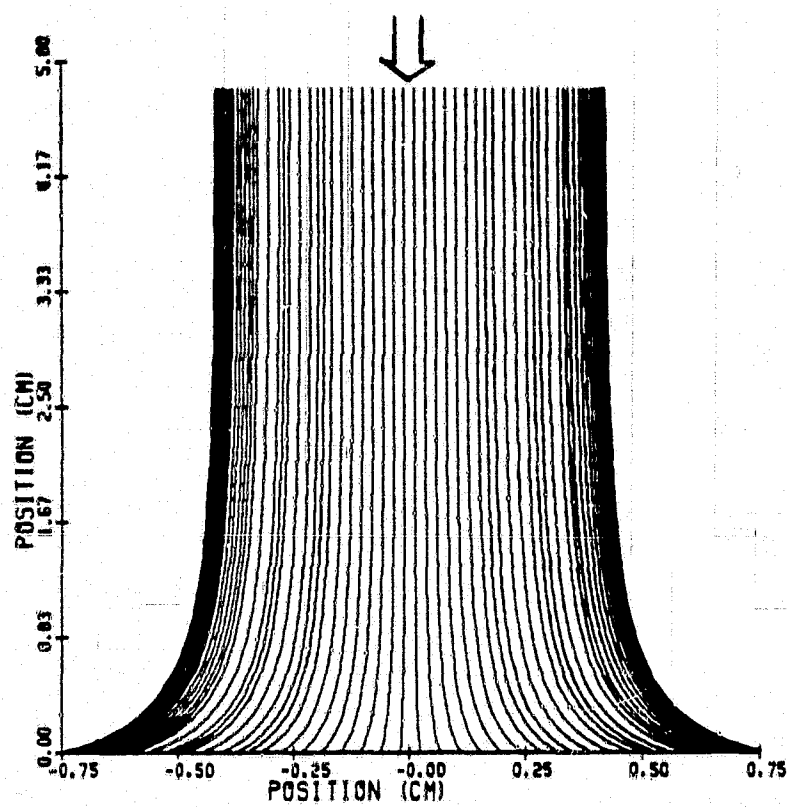


Fig. 6.17 Charging electron trajectories at equilibrium on Teflon. Beam energy 20 keV.

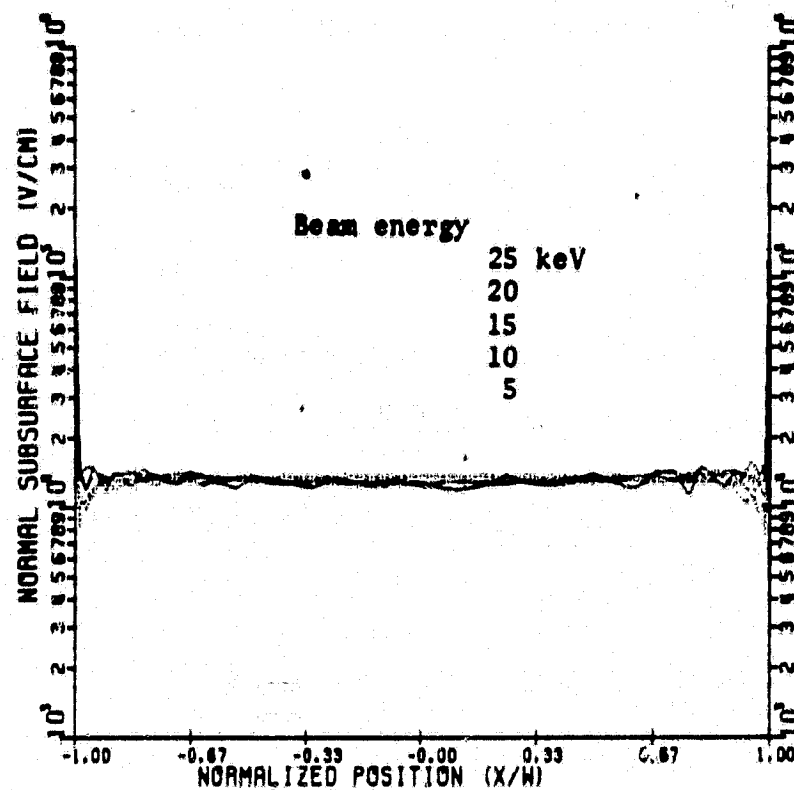
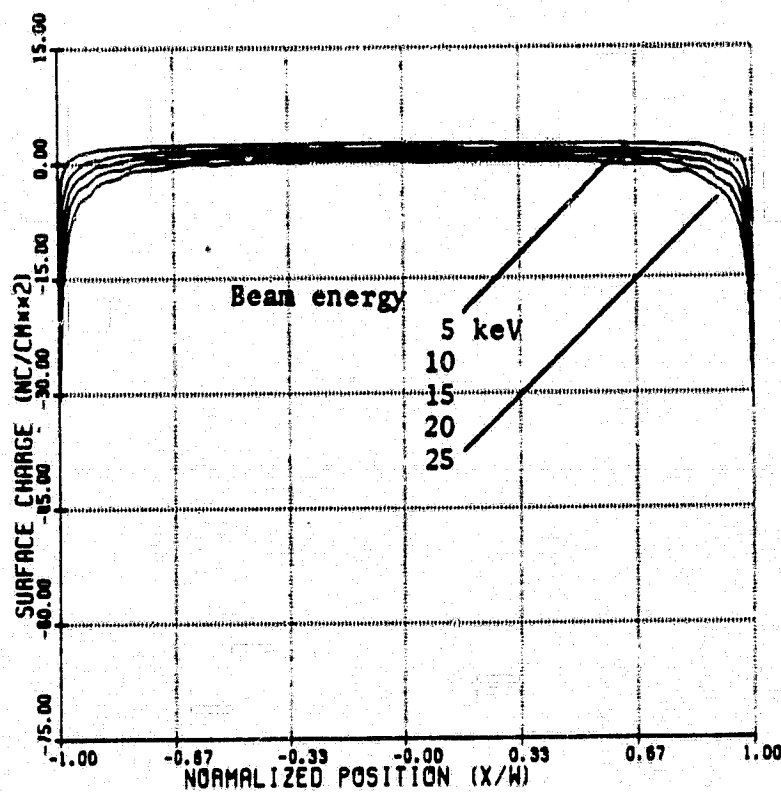


Fig. 6.18 Internal front face field  $E_{ff}$  for Teflon at equilibrium.



front face charge layer  $\rho_1$

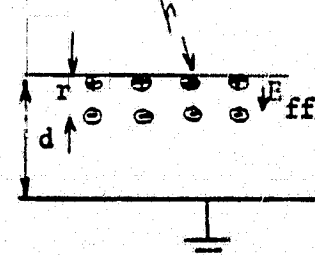


Fig. 6.19 Front face charge density  $\rho_1$  at equilibrium



respectively is presented in Fig. 6.19. In general a small positive surface charge is required becoming negative at the edge due to the observed maxima in the external normal surface field.

The average charge density at steady state is plotted against the equilibrium surface potential at the centre of the strip in Fig. 6.20. The upper curve is obtained from the one-dimensional model which produced a capacitance per unit area of  $\epsilon_0 \epsilon_r / d$ . The lower curve is based on the two-dimensional charging model results. The temporal evolution of the average charge density is plotted against the central surface potential in Fig. 6.21a. The charge-voltage relationship is found to follow the one-dimensional curve until near steady state when charge is lost from the edges. Comparable experimental data [Stevens et al, 1977] is reproduced in Fig. 6.21b. If the low voltage portion of Stevens' data is extrapolated to the steady state voltage we find (for an area of  $300 \text{ cm}^2$ ,  $d = 127 \text{ um}$  and  $\epsilon_r = 2.25$ ) good agreement with the one-dimensional curve in Fig. 6.20. The experimental results however, indicate an equilibrium average charge density that is lower than the computer simulation results by a factor of  $1/1.5$ . Such a discrepancy could be attributed to a change in the dielectric permittivity due to the high internal fields. Interestingly if we take data for the charging dynamics of Teflon [Purvis et al, 1977] in Fig. 5.4 and scale the time axis by a factor of 1.5 as would be appropriate for the proposed change in  $\epsilon_r$ , we again obtain a much improved agreement with the numerical results as indicated in Fig. 6.22. Note that at a lower beam energy (hence a lower internal field strength) reasonable agreement already exists in the charging dynamics (Fig. 5.4).

## 6.2 Material Width Dependence for Teflon

The equilibrium net charge density profiles in Fig. 6.23 were obtained for Teflon with half widths  $W$  equal to 1.5, 1.5/2, 1.5/4 and 1.5/8

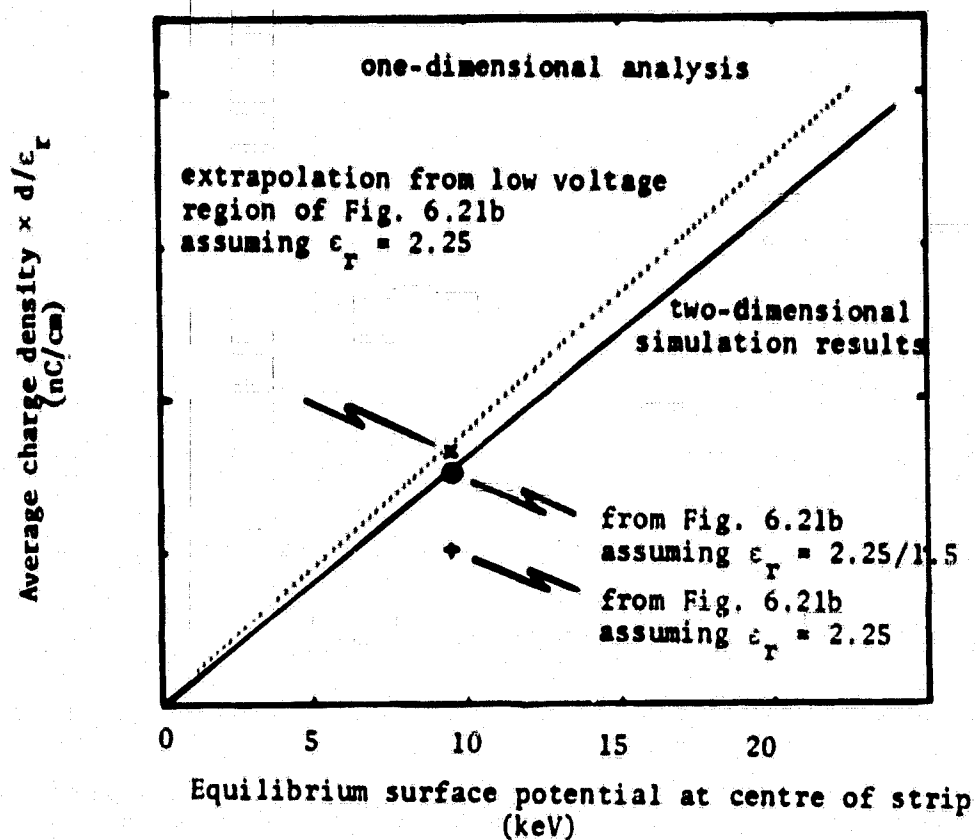


Fig. 6.20 Average charge density at equilibrium vs. central surface potential. Assuming  $\epsilon_r = 2.25$

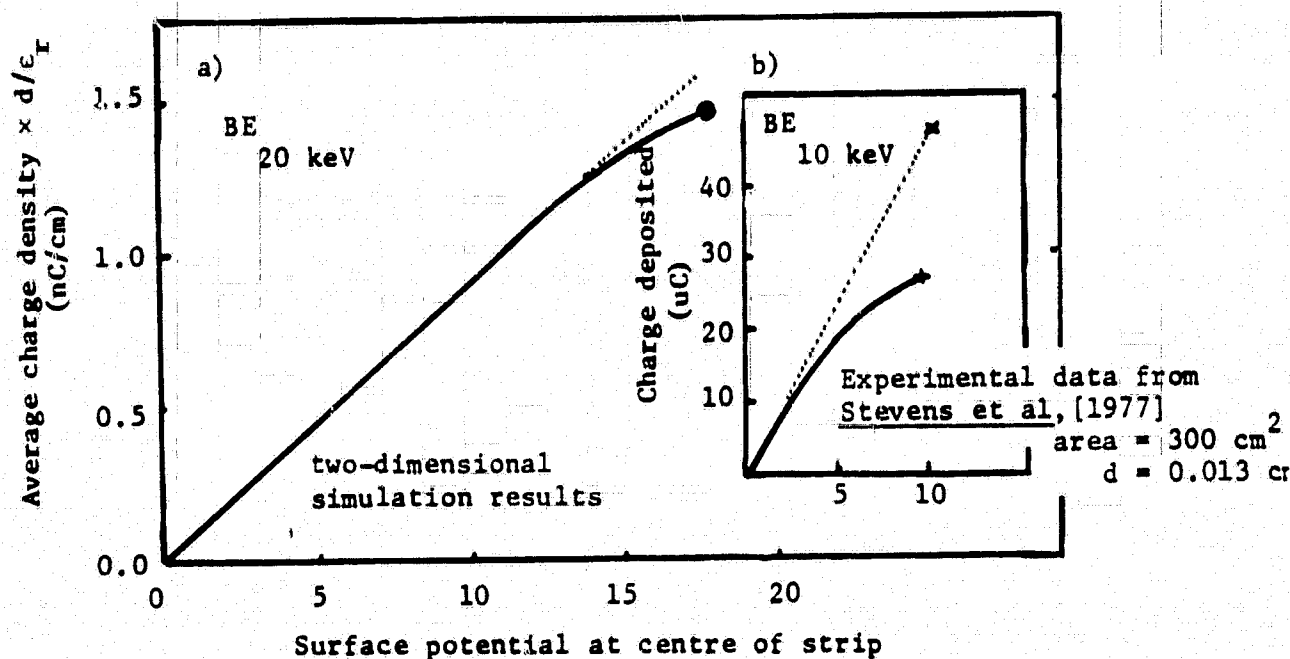


Fig. 6.21 Charging dynamics for Teflon.

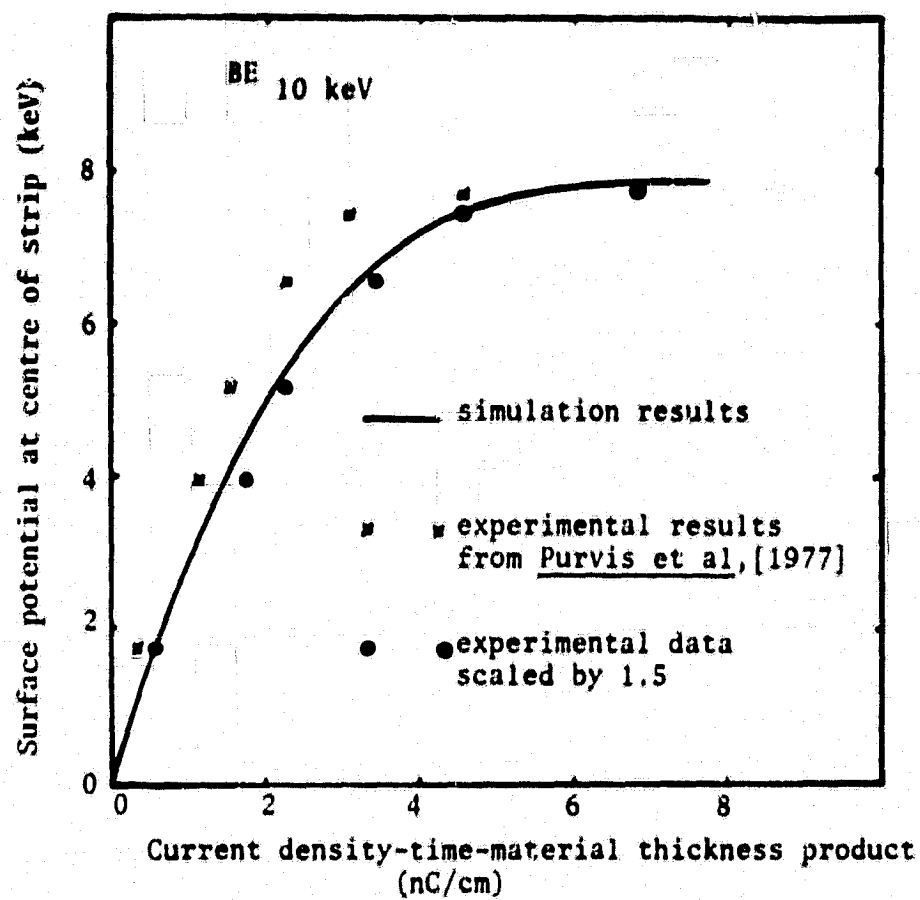


Fig. 6.22 Charging dynamics.

(material thickness 100  $\mu\text{m}$ , beam energy 20 keV). In the centre the charge distribution is nearly independent of the sample half width when plotted against the normalized co-ordinate  $z/W$ . At the edges the narrower strips collect significantly greater charge density.

The surface potential distribution when normalized to the width of the sample is also found to be insensitive to the sample width as indicated in Fig. 6.24a. The close agreement between experimental results and the simulation results in Fig. 6.8 where the range in half width was 0.75 to 5.0 cm tends to support this form of width scaling. Further experimental evidence presented in Fig. 6.24b confirms the scaling on strips of Teflon thermal control tape [Aron and Staskus, 1979]. The behaviour of the surface charge distribution is also consistent with measurements indicating that the total charge released during a discharge event is proportional to the exposed area [Balmain and Dubois, 1979].

Equation 6.2 is an approximate empirical expression fitting the behaviour of the surface potential distribution for arbitrary beam energy and arbitrary sample width.

$$V = V_0 (1 - \exp(-\sqrt[4]{(4.6)^4 (1.185 - |z/W|)^4 - k(W)})) \quad (6.2)$$

where

$$|z/W| \leq 1.0$$

$k(W)$  = a correction factor to match the edge characteristic

$V_0$  = equilibrium surface potential from eq. 3.13

from Fig. 6.24 we find

$$k(W) = 0.5120, 0.4945, 0.4464, 0.350$$

for

$$W = 1.5, 1.5/2, 1.5/4, 1.5/8 \text{ cm respectively.}$$

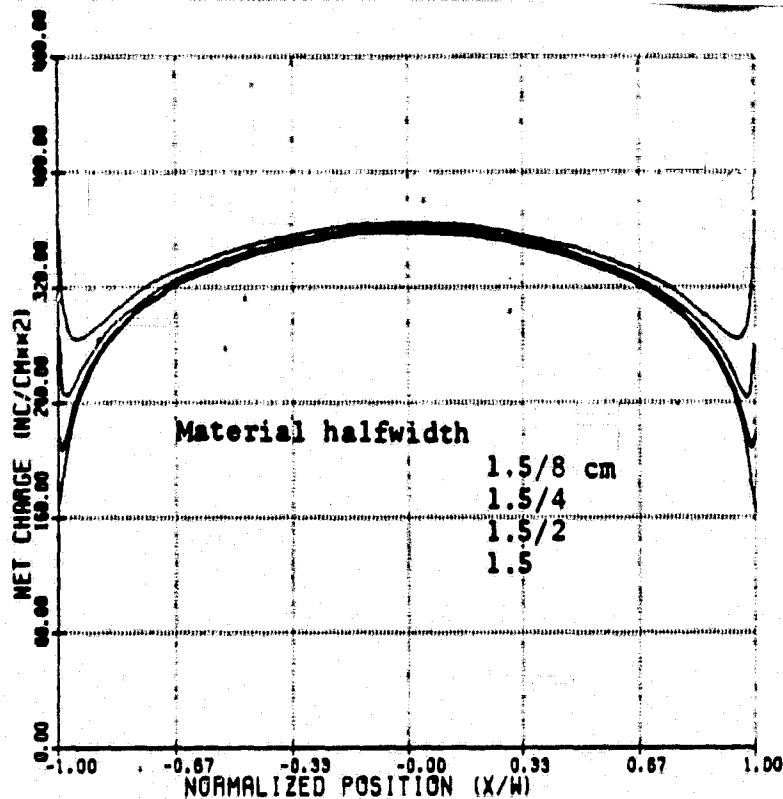
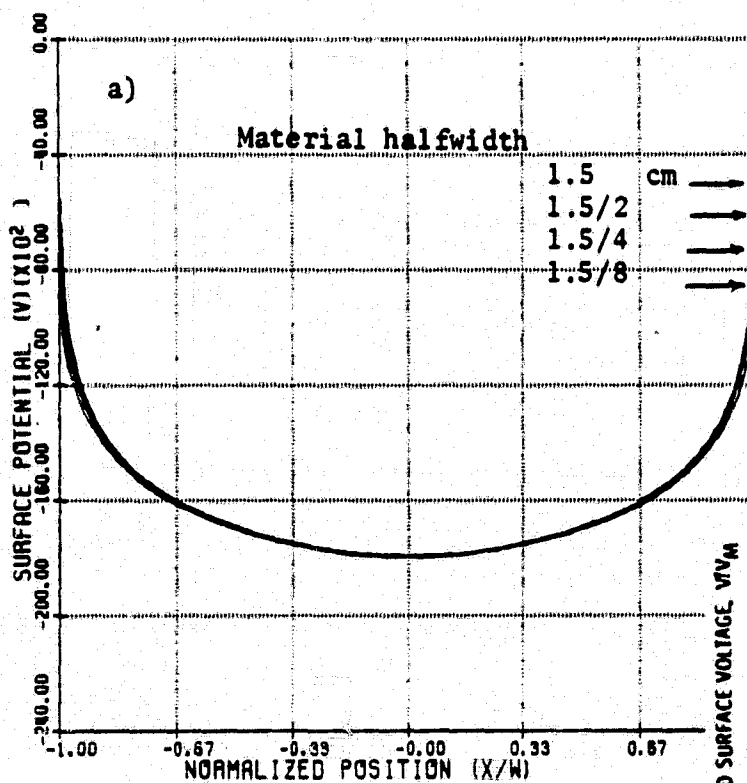


Fig. 6.23 Equilibrium surface charge density distributions for Teflon.



ORIGINAL PAGE IS  
OF POOR QUALITY

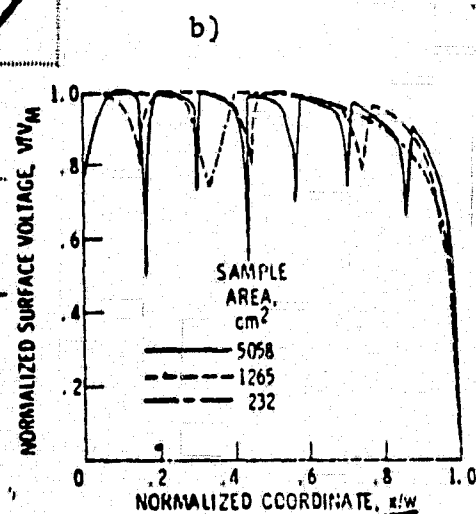


Fig. 6.24a Equilibrium surface potential profiles for Teflon.

Fig. 6.24b Experimental data from  
Aron and Staskus, [1979]

- Equilibrium surface-voltage  
profiles - normalized.

For  $|z/W| < 0.9$  eq. 6.2 can be simplified to a function of a single normalized parameter  $z/W$

$$V = V_0 (1 - \exp(-4.6(1.185 - |z/W|))) \quad (6.3)$$

where

$$|z/W| < 0.9$$

Similar width scaling is found in comparing the angle of incidence as a function of the normalized coordinate for each sample width. This result could have been deduced directly from the equilibrium surface potential curves since the angle of incidence at equilibrium is fixed once the surface potential and beam energy are specified (using Fig. 6.10). The angle of incidence for each strip is therefore practically the same as that presented in Fig. 6.9 for a 20 keV beam. Slight shifts between the curves at the edges were found in accordance with the noted divergence in the surface potentials in Fig. 6.24.

The bulk field, being approximately equal to the surface potential divided by the material thickness, is also found to obey the same width scaling. A representative curve can be found in Fig. 6.13 for the 20 keV beam.

The external surface fields are presented in Figs. 6.25 and 6.26. Near the centre of the samples they are found to be inversely proportional to the strip width. The front face fields are the same as those shown in Fig. 6.18.

### 6.3 Beam Angle Dependence for Teflon

The equilibrium net charge profiles in Fig. 6.27 were obtained for Teflon by charging with electron beams incident at  $0^\circ$ ,  $15^\circ$ ,  $30^\circ$  or  $45^\circ$  relative to the surface normal (material half width 0.75 cm, material thickness 100  $\mu\text{m}$ , beam energy 20 keV). The beam originates from the left

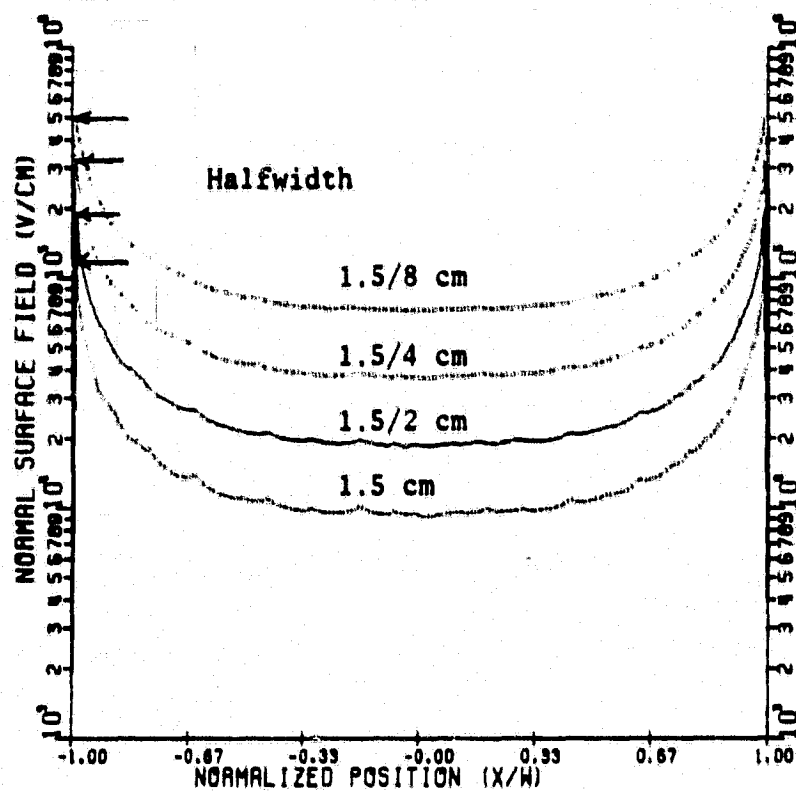


Fig. 6.25 External normal surface field distribution for Teflon at equilibrium.

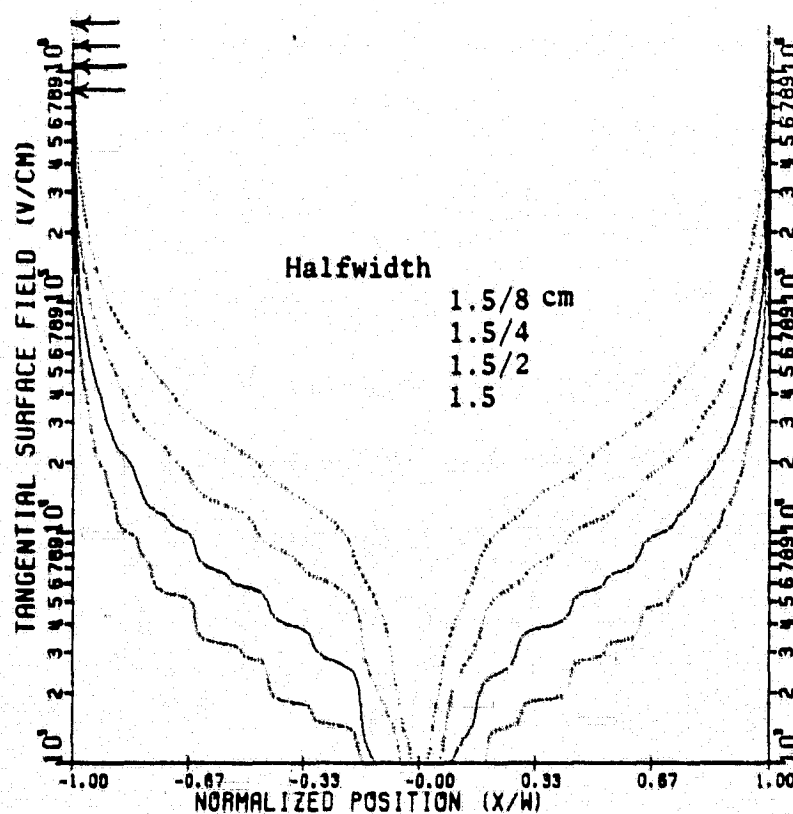


Fig. 6.26 External tangential surface field distribution for Teflon at equilibrium.

of the specimen tending to deposit a larger charge density at the edge nearest to its source. The central maximum tends to shift towards the near edge and the maximum charge density tends to increase with increasing beam angle.

The charging dynamics for a beam angle of  $45^\circ$  are illustrated in Fig. 6.28. The explicit time dependence for the centre and edges is given in Fig. 6.29. Note the beam current density of  $50 \text{ nA/cm}^2$  refers to the current component in the  $y$  direction (i.e. normal to the exposed surface not perpendicular to the beams direction). At the near edge the charge density had not reached an equilibrium value when the simulation was terminated as the rate of charge accumulation indicated by the final slope in Fig. 6.29 was still 4% of the beam current.

The surface potential distribution is presented in Fig. 6.30. The maximum is found to move to the near edge as the beam angle is increased. The magnitude of the maximum remains constant and indicates the position on the sample where the incident electrons impact the surface at  $0^\circ$ . The angle of incidence is presented in Fig. 6.31 for each case. At the near edge  $\partial\phi_1/\partial z$  increases with increasing beam angle. For a beam angle of  $45^\circ$   $\partial\phi_1/\partial z$  reaches  $117^\circ/\text{mm}$  compared to an average of  $8^\circ/\text{mm}$  for a beam angle of  $0^\circ$ .

The maximum internal bulk field as suggested by the surface potential does not change in magnitude though it moves towards the near edge for increasing beam angles. Over a large fraction of the sample the bulk field is reduced.

The external surface electric fields (Figs. 6.32 and 6.33) are found to be enhanced at the near edge and reduced at the far edge. The maximum tangential component was increased by a factor of 3 between the  $0^\circ$  and  $45^\circ$  charging beams to  $3.0 \times 10^6 \text{ V/cm}$ . A similar increase in the maximum



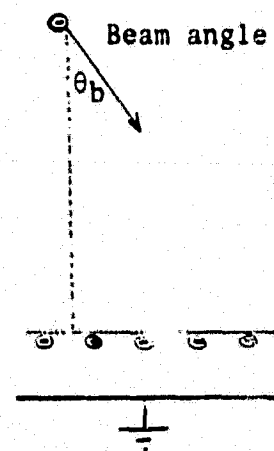
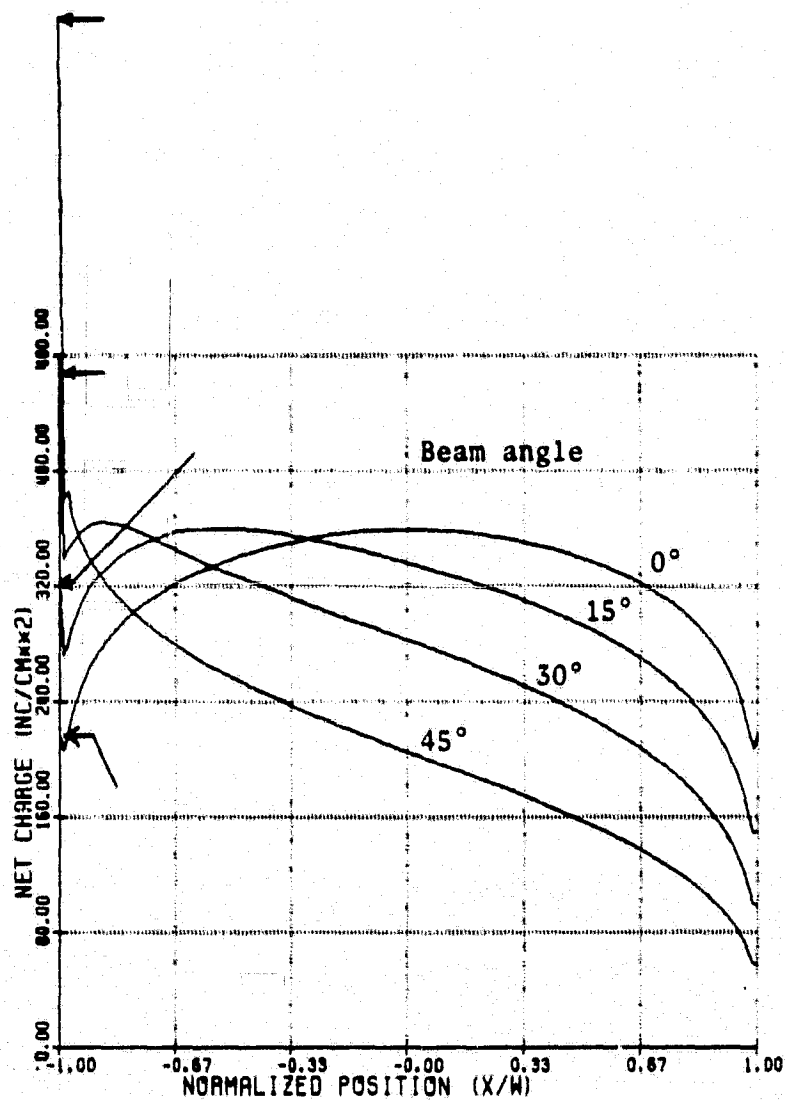


Fig. 6.27 Equilibrium surface charge density distributions for Teflon. Maxima are marked with arrows.

Fig. 6.29 Explicit time response at centre and edges of sample.  
Beam angle  $45^\circ$ . Beam density  $50 \text{ nA/cm}^2$ .

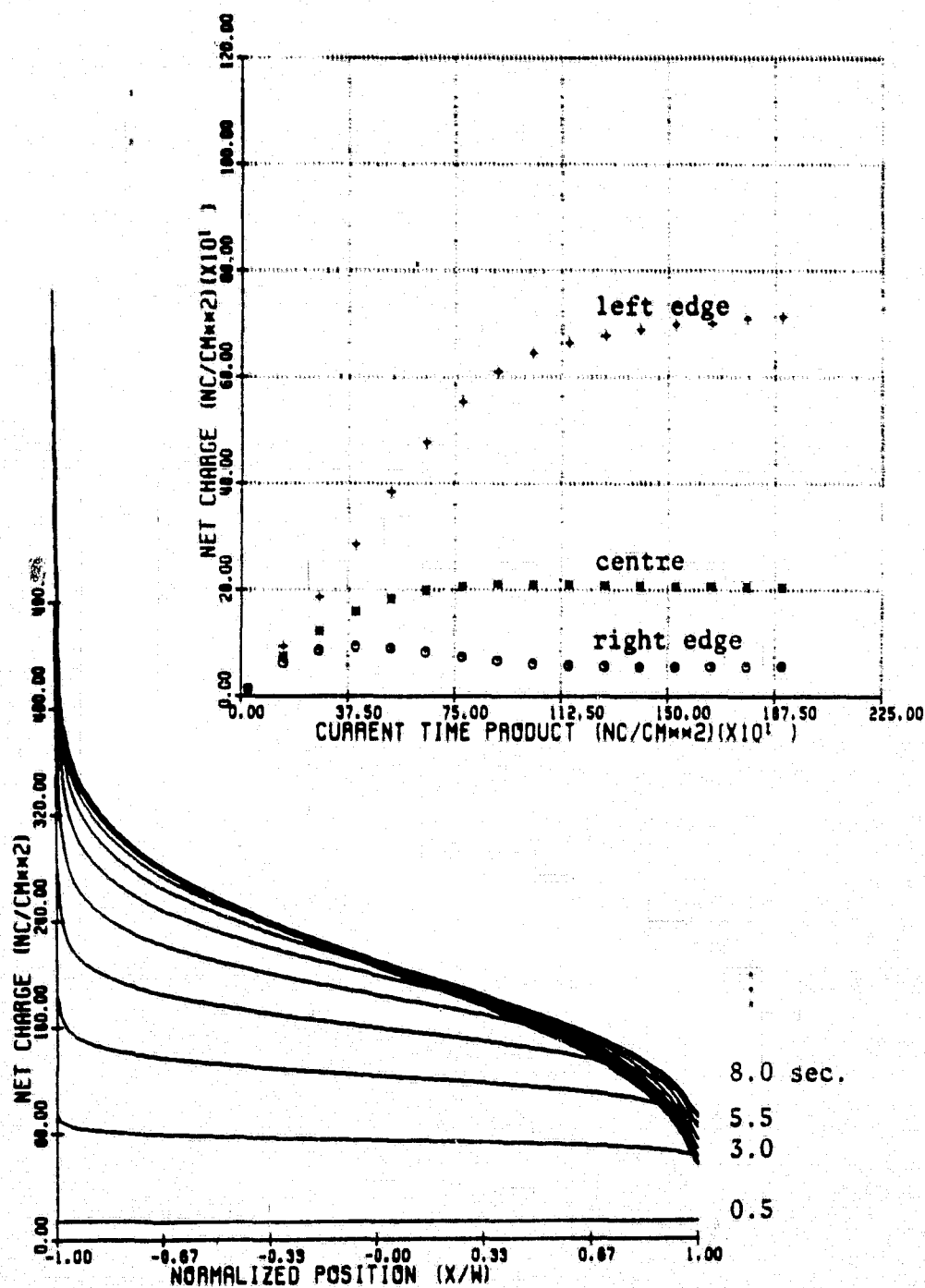


Fig. 6.28 Charging dynamics. Beam angle  $45^\circ$ . Beam density  $50 \text{ nA/cm}^2$ .

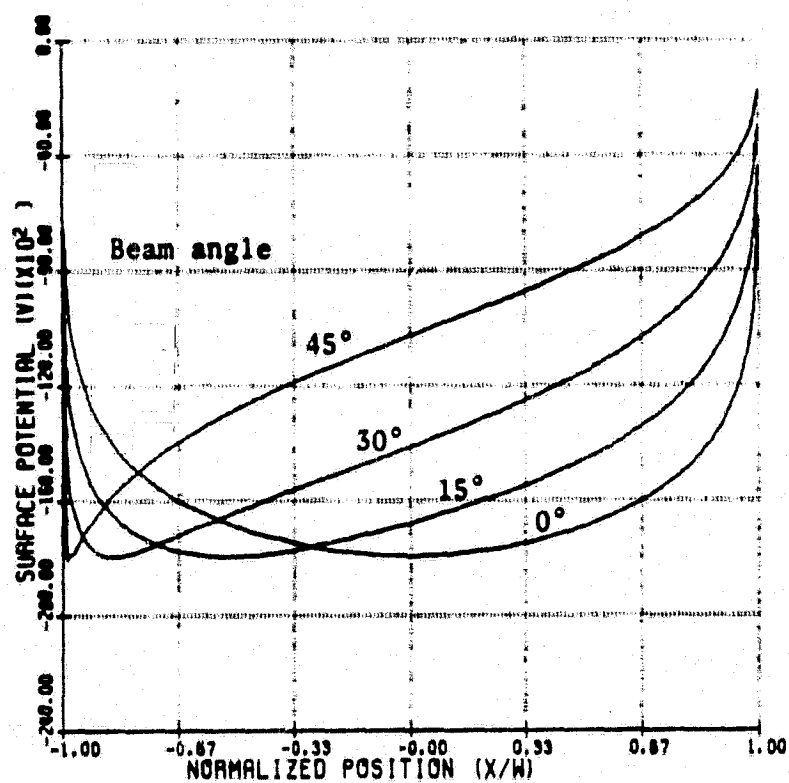


Fig. 6.30 Equilibrium surface potential distributions.

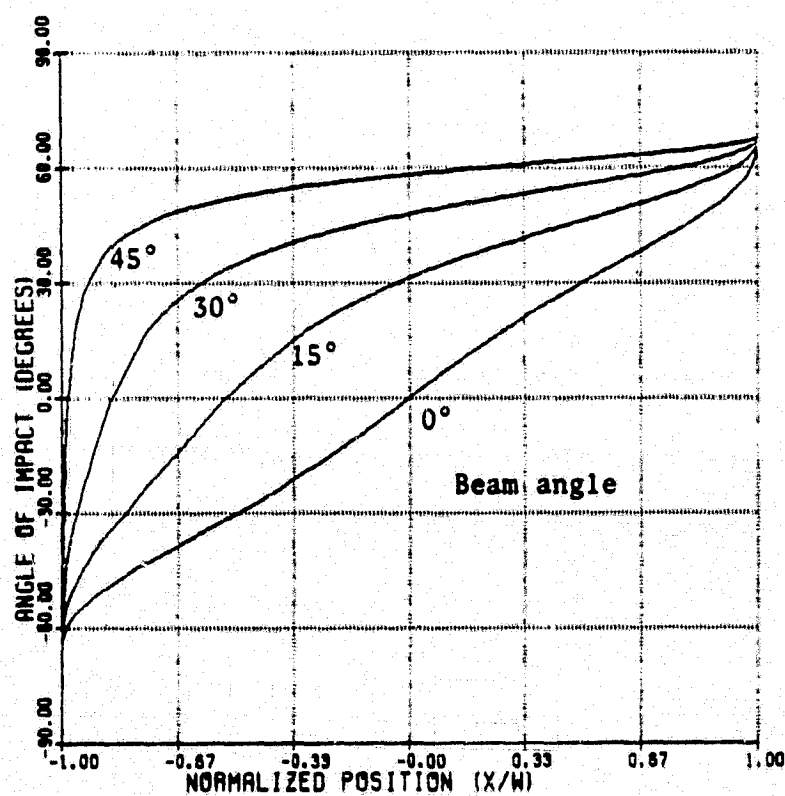


Fig. 6.31 Angle of incidence distributions at equilibrium.

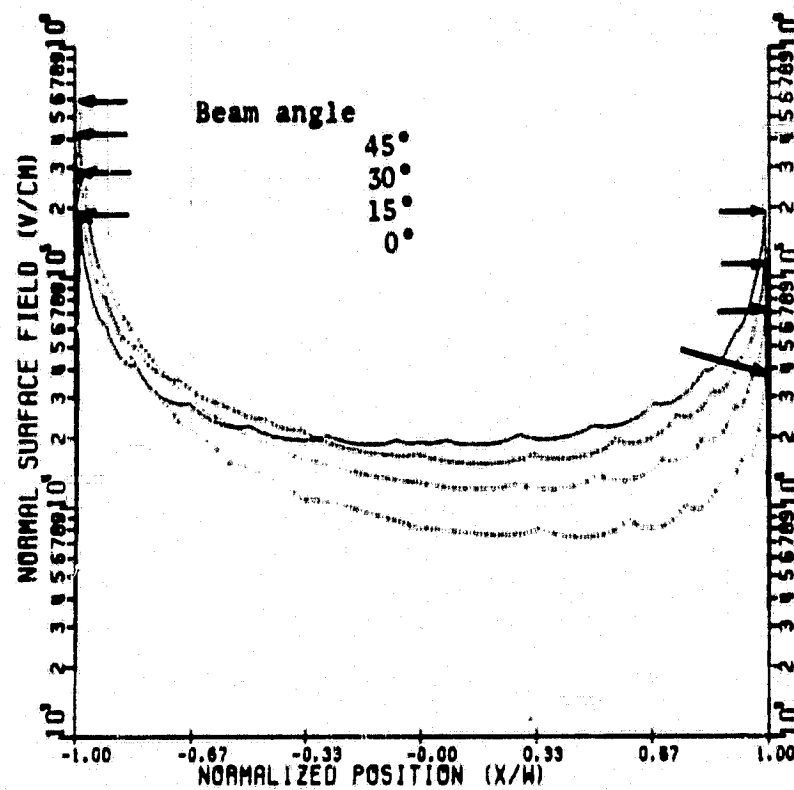


Fig. 6.32 External normal surface field distributions at equilibrium.

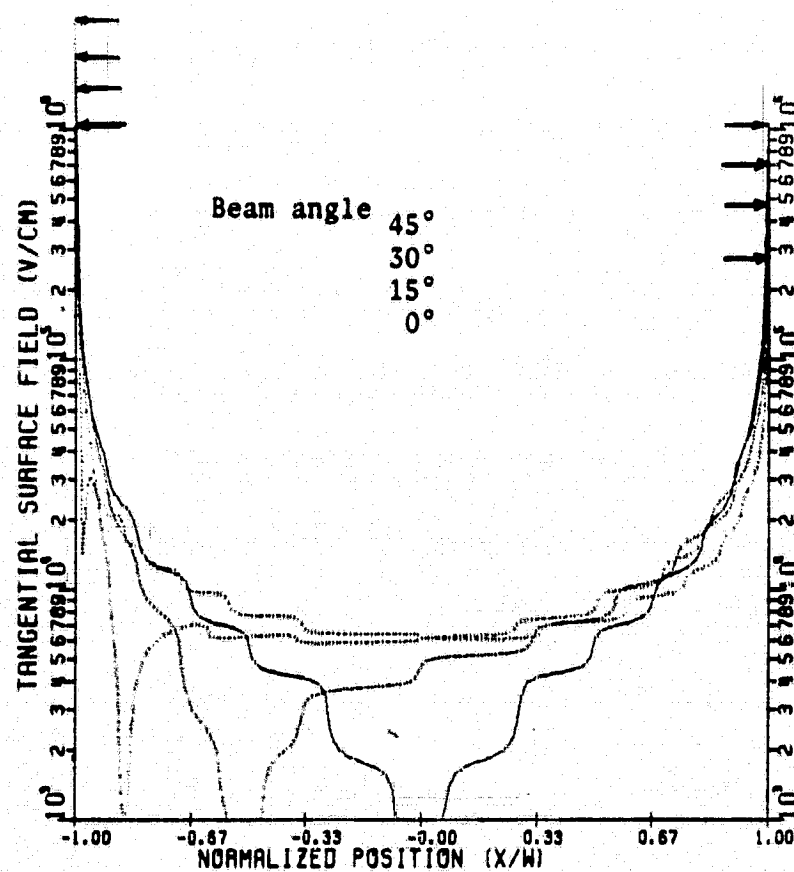


Fig. 6.33 External tangential surface field distributions at equilibrium.

ORIGINAL PAGE IS  
OF POOR QUALITY

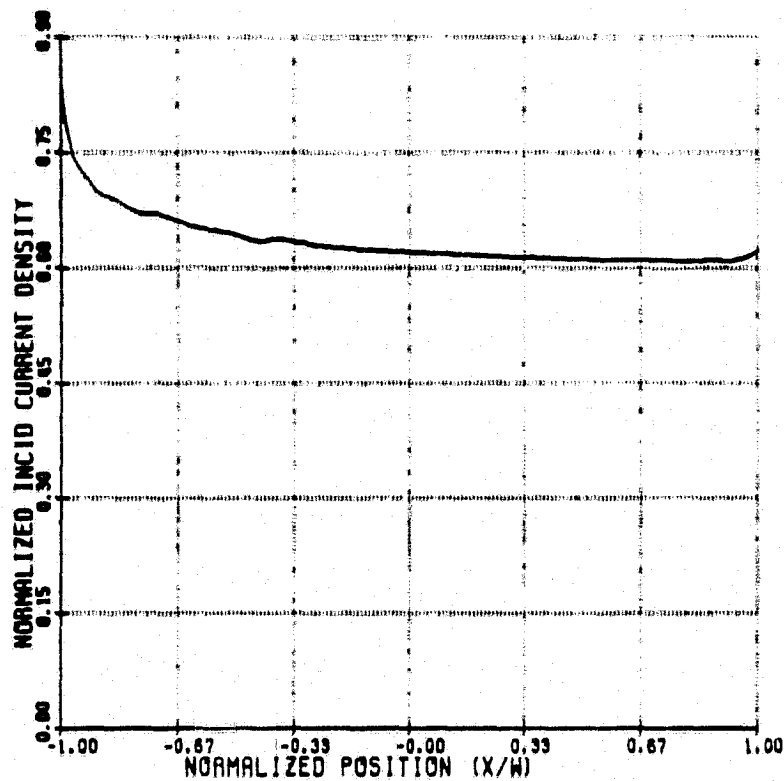


Fig. 6.34 Reduction in incident current density at equilibrium due to beam spreading. Beam angle  $45^\circ$ .

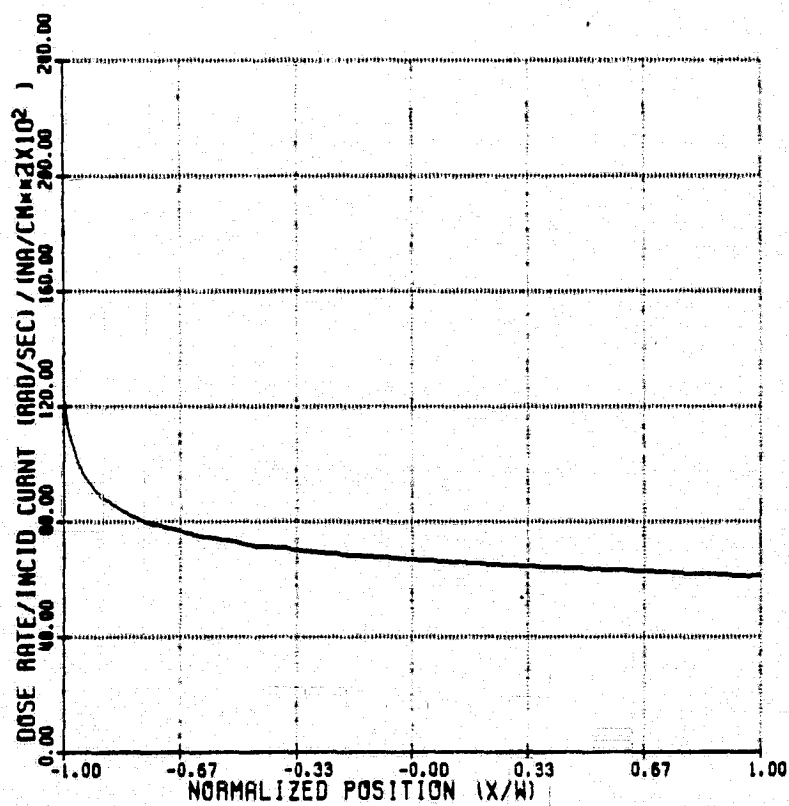


Fig. 6.35 (Dose rate/beam current density) distribution at equilibrium. Beam angle  $45^\circ$ .

normal component resulted in a field strength of  $6 \times 10^5$  V/m for a  $45^\circ$  charging beam.

The front face field is found to be remarkably flat with no discernible difference between the  $45^\circ$  and  $0^\circ$  beams.

The incident current density and dose rate profiles at equilibrium for a beam angle of  $45^\circ$  are presented in Figs. 6.34 and 6.35 respectively.

#### 6.4 Material Thickness Dependence for Teflon

The equilibrium net charge profiles in Fig. 6.36 were obtained for Teflon with material thicknesses of 100, 50 and 25  $\mu\text{m}$  (material half width 0.75 cm, beam energy 15 keV). The dipole moment per unit area  $\rho(z)d$ , as suggested in section 5.1, is independent of the thickness. The surface potential and angle of incidence are also invariant.

The tangential surface field (Fig. 6.39) is increased at the edge for a decrease in the material thickness. The external normal surface field (Fig. 6.38) shows no appreciable change. The internal bulk field (Fig. 6.37) is inversely proportional to the material thickness as would be expected for a constant surface potential.

The front face field displayed no appreciable change from that presented in Fig. 6.18.

#### 6.5 Non-conventional Charging Geometries for Teflon

##### 6.5.1 Grounded Central Slot

The effect of a grounded gap between two adjacent strips of Teflon has been investigated for gap widths of 0.283 mm and 0.660 mm. The geometry modelled is presented in Fig. 6.40. (material half width 0.75 cm, material thickness 100  $\mu\text{m}$ , beam energy 20 keV). Except for the peaks in the charge density at the inner edges the equilibrium charge distributions in Fig. 6.41 are similar to those found for a uniform material.

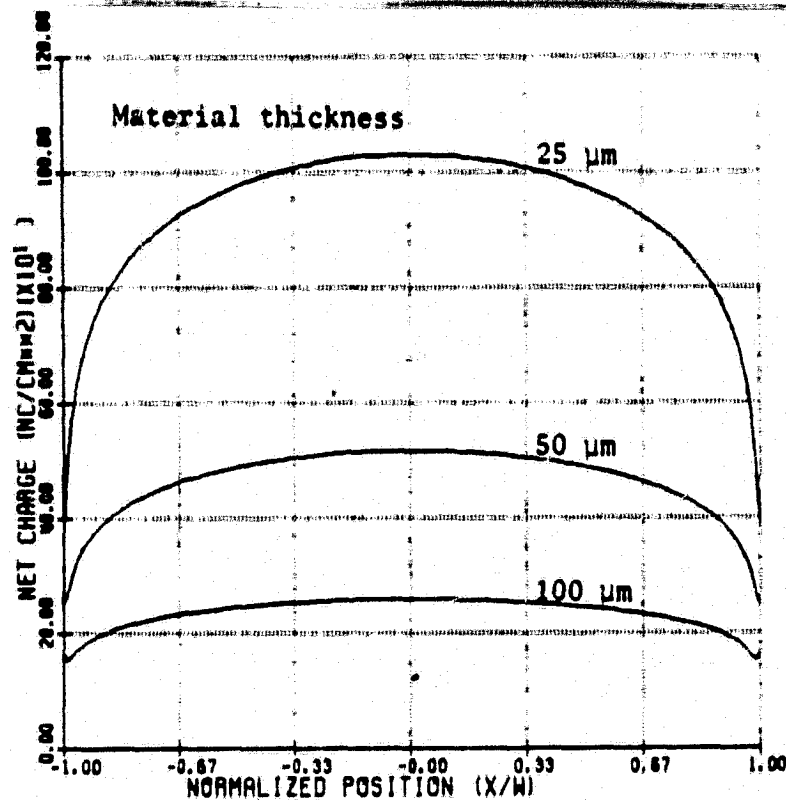


Fig. 6.36 Equilibrium surface charge density distributions.

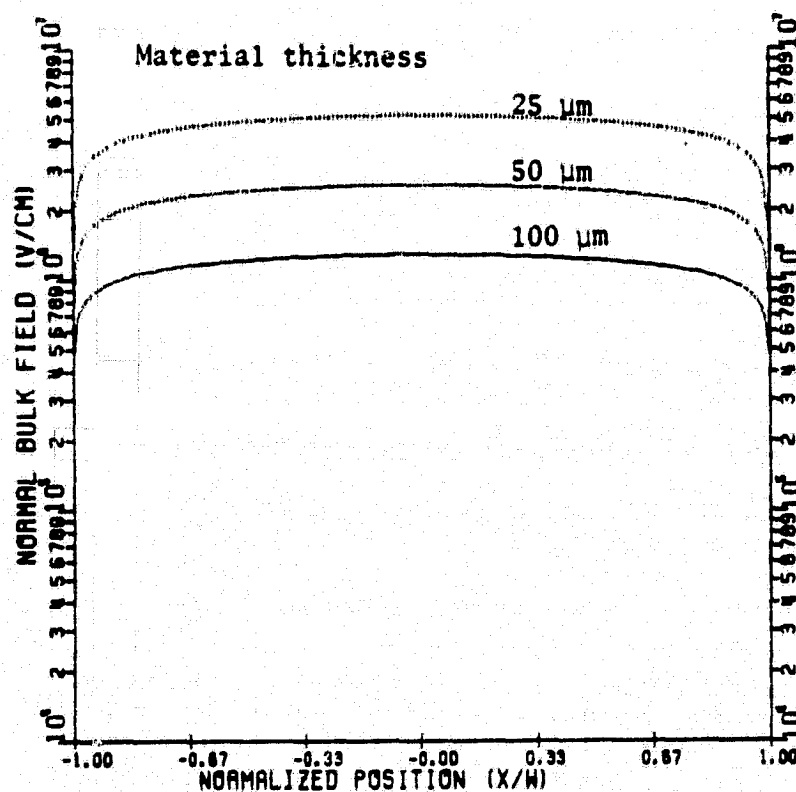


Fig. 6.37 Internal normal bulk field distributions at equilibrium.

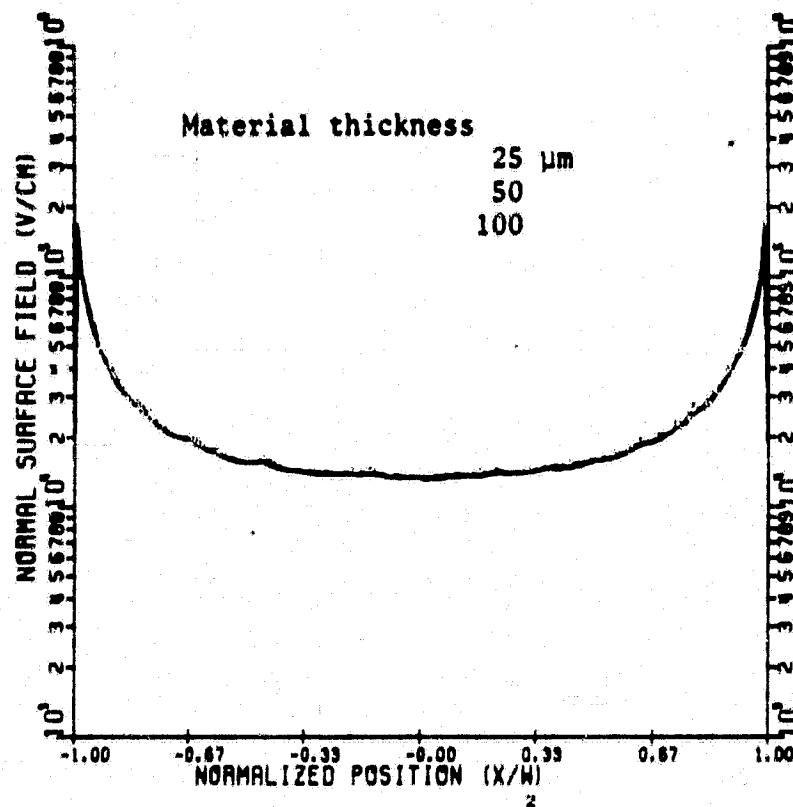


Fig. 6.38 External normal surface field distributions at equilibrium.

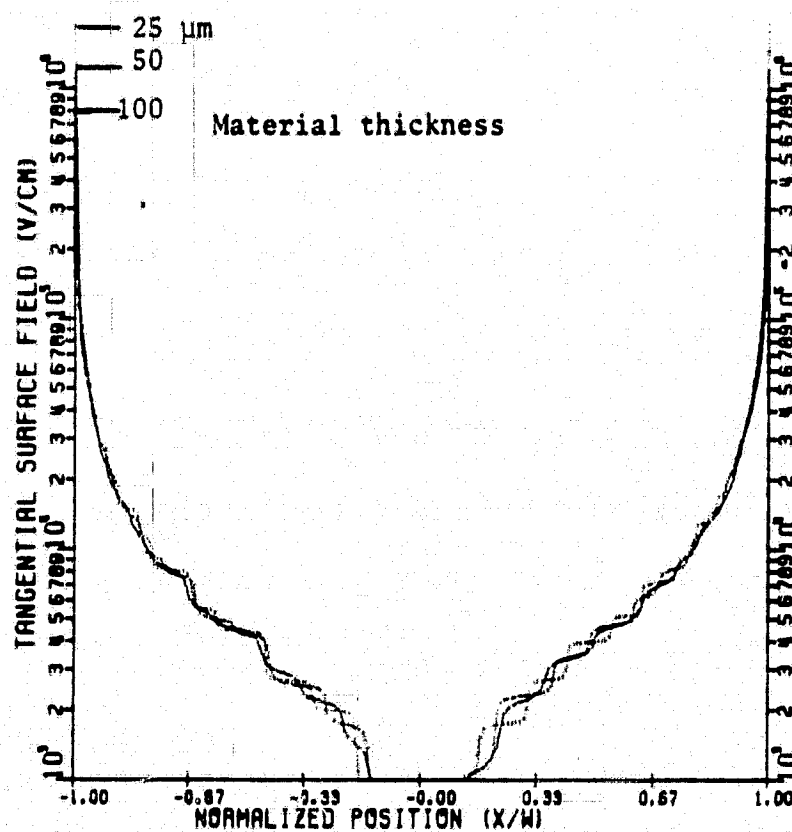


Fig. 6.39 External tangential surface field distributions at equilibrium.



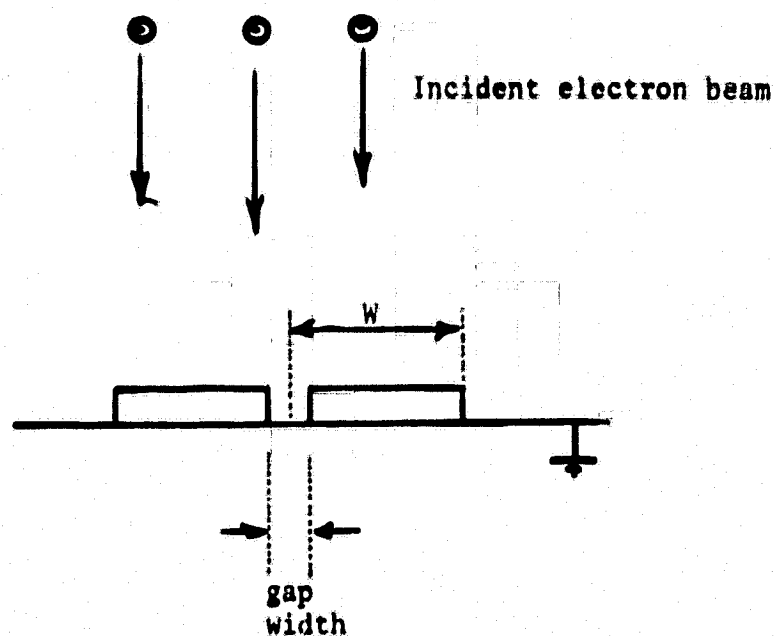


Fig. 6.40 Grounded central slot geometry.

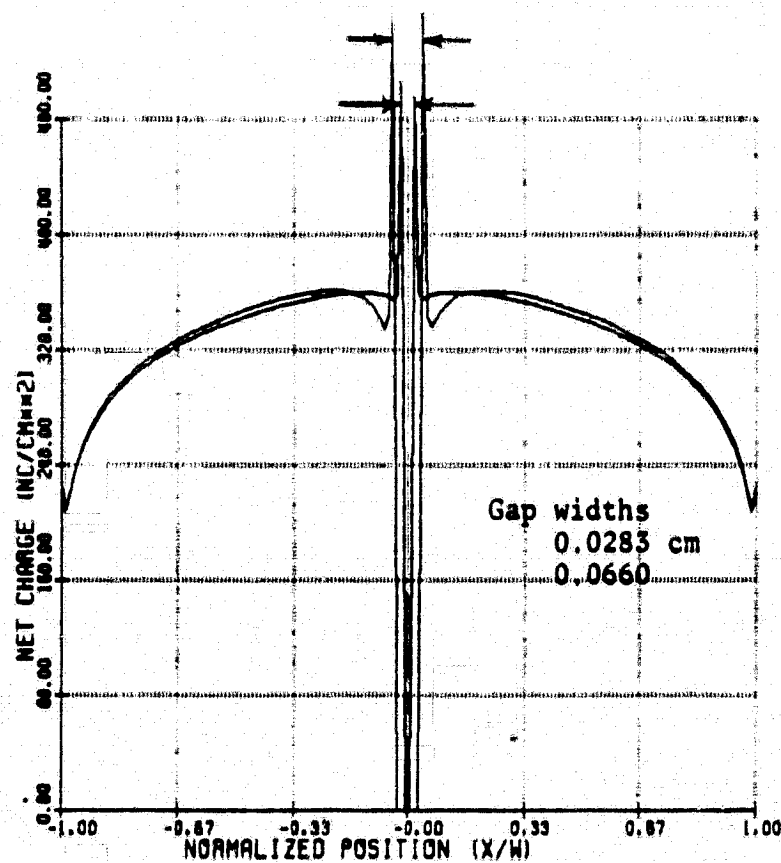


Fig. 6.41 Equilibrium surface charge density distributions.

The surface potential distribution is presented in Fig. 6.42. The angle of impact (Fig. 6.43) suggests considerable beam steering in the neighbourhood of the slot. Figure 6.44 traces sample incident electron trajectories at steady state for the 0.66 mm slot width. The equilibrium current density is given in Fig. 6.45 indicating considerable beam focusing into the slot area. The dose rate profile at equilibrium is very similar to that obtained for a uniform strip.

The external normal and tangential surface fields are presented in Figs. 6.46 and 6.47. Both display additional peaks at the inner edges. The narrower slot tends to produce a slightly larger maxima for both field components.

The internal bulk field can be determined from the surface potential. Its maximum value is little changed from that obtained for a uniform strip. The internal front face field is also similar to that found for a uniform strip.

Calculation of the equipotential lines at steady state reveals a saddle point 0.9 mm above the centre of the 0.283 mm gap. The corresponding barrier potential was 15.2 kV. These results compare favourably with the value obtained from the approximate analysis of Chapter 5 (eqs. 5.22 and 5.23 yield a saddle point potential 14.9 kV, 1.04 mm above the gap centre).

Measurements made by Robinson [1977] suggest a large increase in the rate of breakdown occurs when a slot is cut in the material. A 300 fold increase was observed for a 21 keV beam at  $40 \text{ nA/cm}^2$  when a slot was cut in the sample. The simulation results indicate that the increased tendency to discharge is consistent with increases in the surface fields and exposed edge length rather than the internal fields.

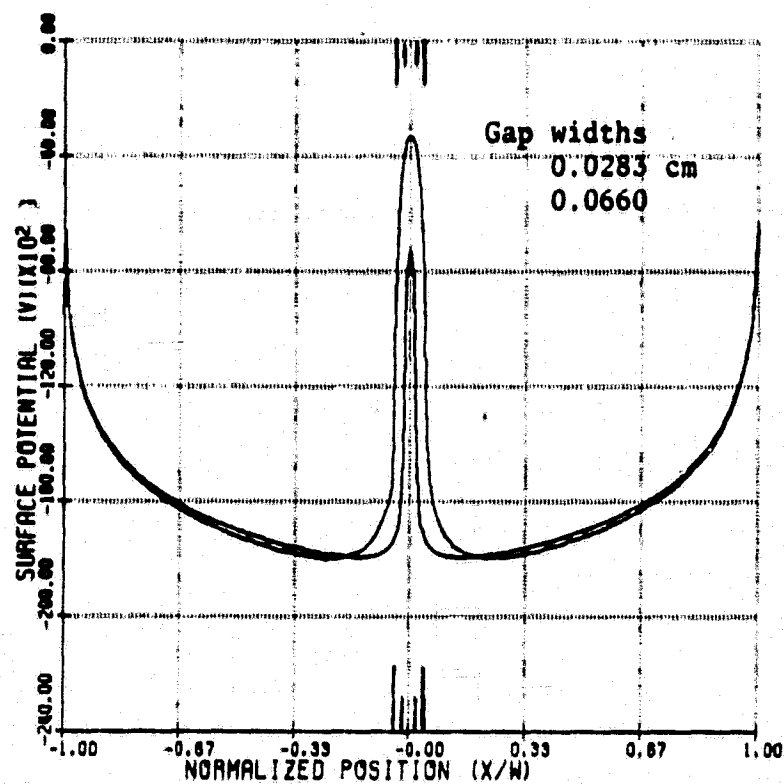


Fig. 6.42 Equilibrium surface potential distributions.

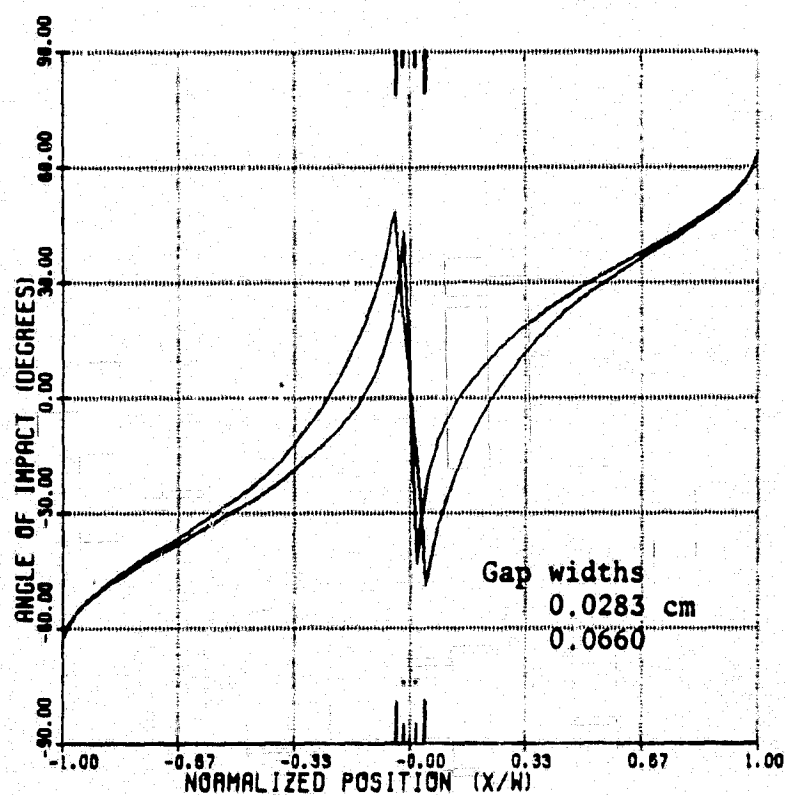


Fig. 6.43 Angle of incidence at equilibrium.

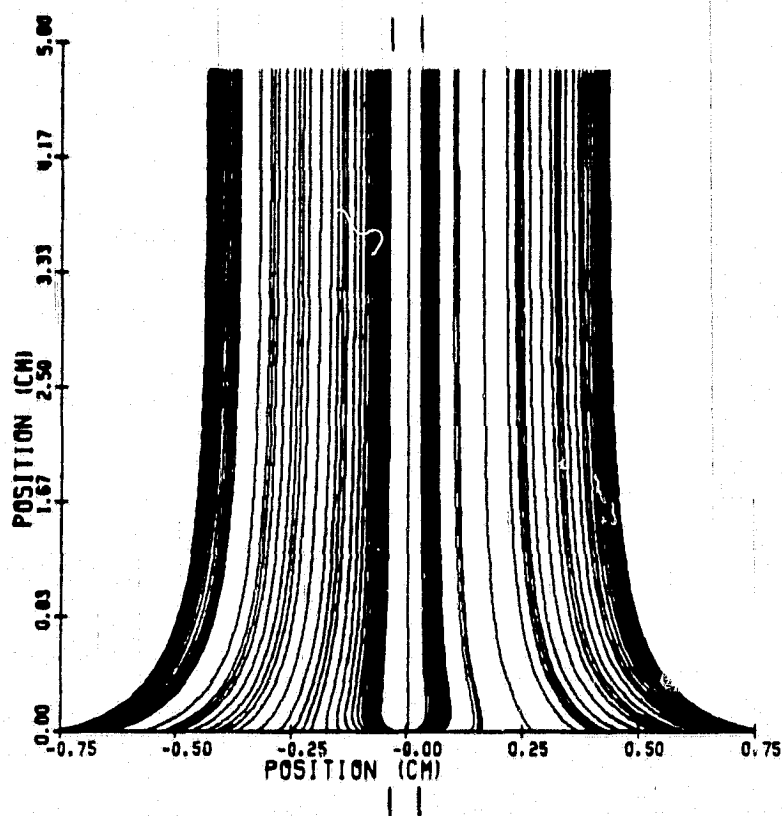


Fig. 6.44 Charging electron trajectories at equilibrium.  
Gap width 0.066 cm.

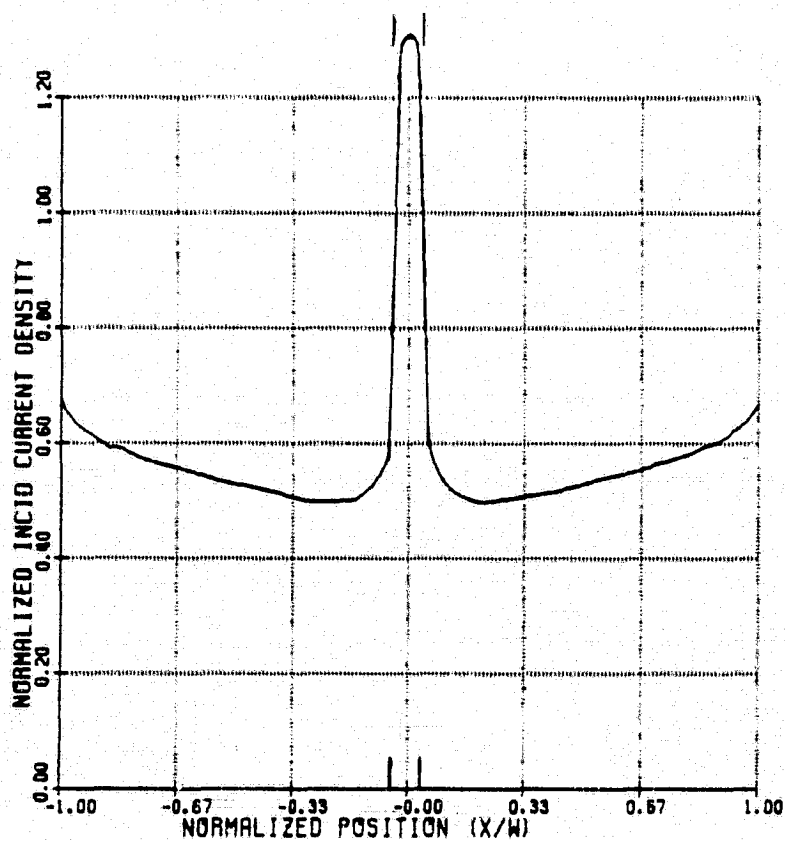


Fig. 6.45 Incident current density at equilibrium.  
Gap width 0.066 cm.

ORIGINAL PAGE IS  
OF POOR QUALITY

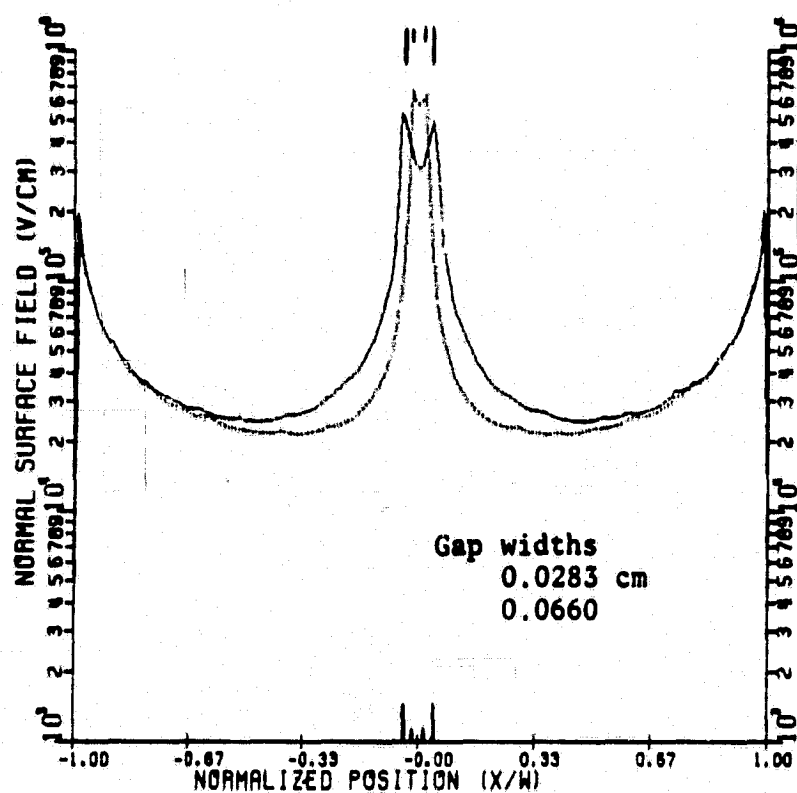


Fig. 6.46 External normal surface field at equilibrium.

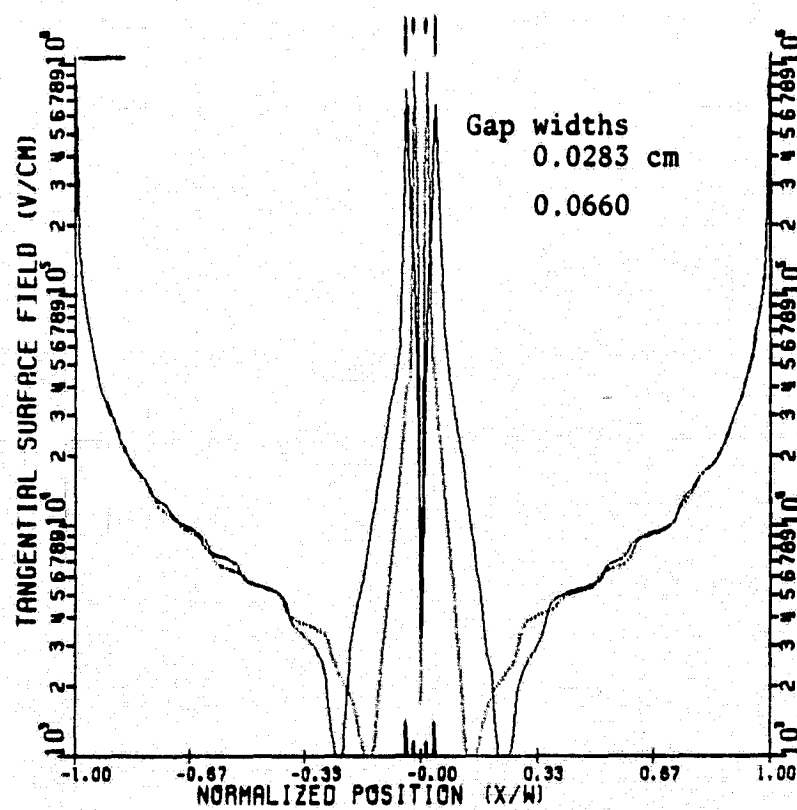


Fig. 6.47 External tangential surface field at equilibrium.

### 6.5.2 Precharging Effects

The effect of a non-zero initial charge distribution on Teflon has been investigated for a uniformly charged central sub-strip (material half width 0.75 cm, material thickness 100  $\mu\text{m}$ , beam energy 20 keV). A negative charge region of  $250 \text{ nC/cm}^2$  was used at two different widths, 0.94 mm and 0.235 mm. A positively charged region was investigated for the same charge density magnitude at a width of 0.47 mm. The charging dynamics are presented in Figs. 6.48, 6.49 and 6.50 for each case described above.

The charge density distributions tend to converge to a universal steady state typified by those simulations with zero initial conditions. However, near the boundaries of the precharged region the charge distribution continues to reflect the discontinuous nature of the assumed initial state.

The surface fields display the greatest sensitivity to the irregularities in the charge distribution at the end of the simulation (the term equilibrium is avoided as the net rate of charge transfer to the boundary region at the end of the simulation was at least an order of magnitude greater than that found over the remainder of the surface). The surface fields for the 0.94 mm negatively precharged stripe (Figs. 6.51 and 6.52) are typical of the other cases described. The magnitude of the field perturbation is of the order of  $10^5 \text{ V/cm}$  in both the normal and tangential component.

A non-zero initial charge distribution can be physically attributed to a partial discharge of the material's surface or static charging of the surface due to brushing or rubbing in the material's preparation. The charging dynamics in Figs. 6.48, 6.49 and 6.50 suggest that although the final charge distribution will approach that previously

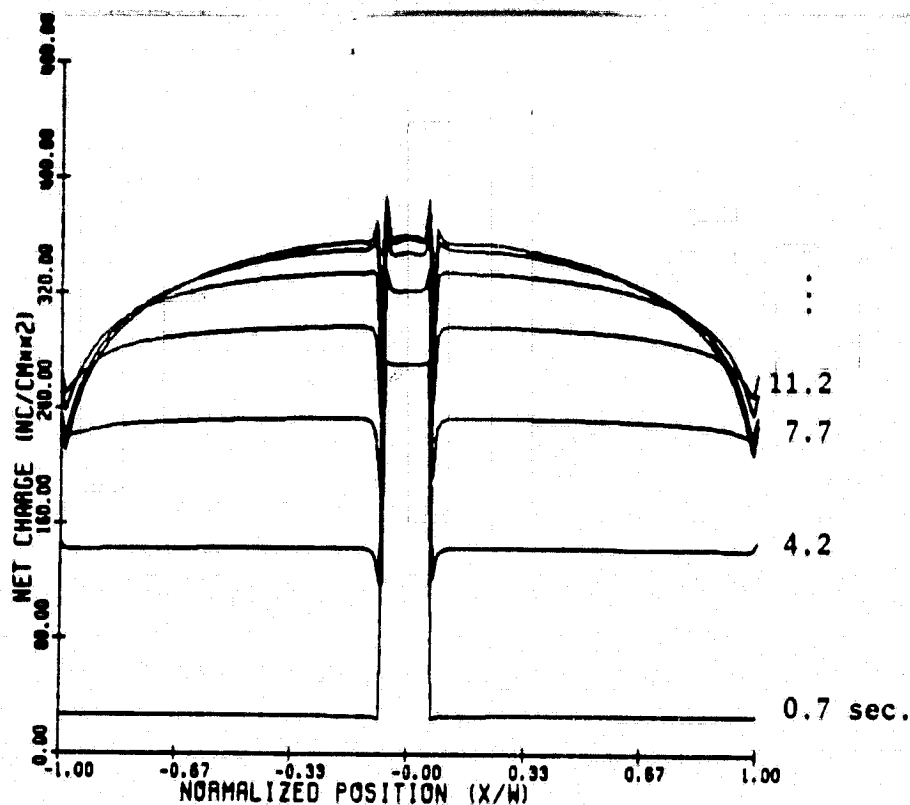


Fig. 6.48 Charging dynamics. Strip 0.094 cm wide, precharged to  $250 \text{ nC/cm}^2$  (electron charge density). Beam density  $50 \text{ nA/cm}^2$ .

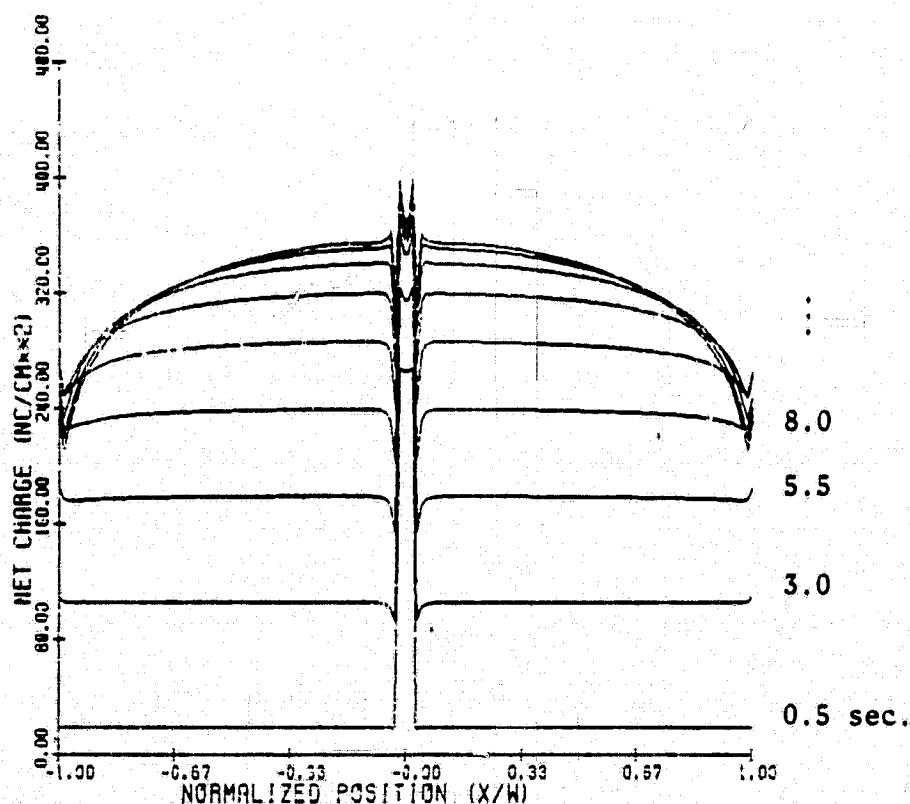


Fig. 6.49 Charging dynamics. Strip 0.0235 cm wide, precharged to  $250 \text{ nC/cm}^2$  (electron charge density). Beam density  $50 \text{ nA/cm}^2$ .

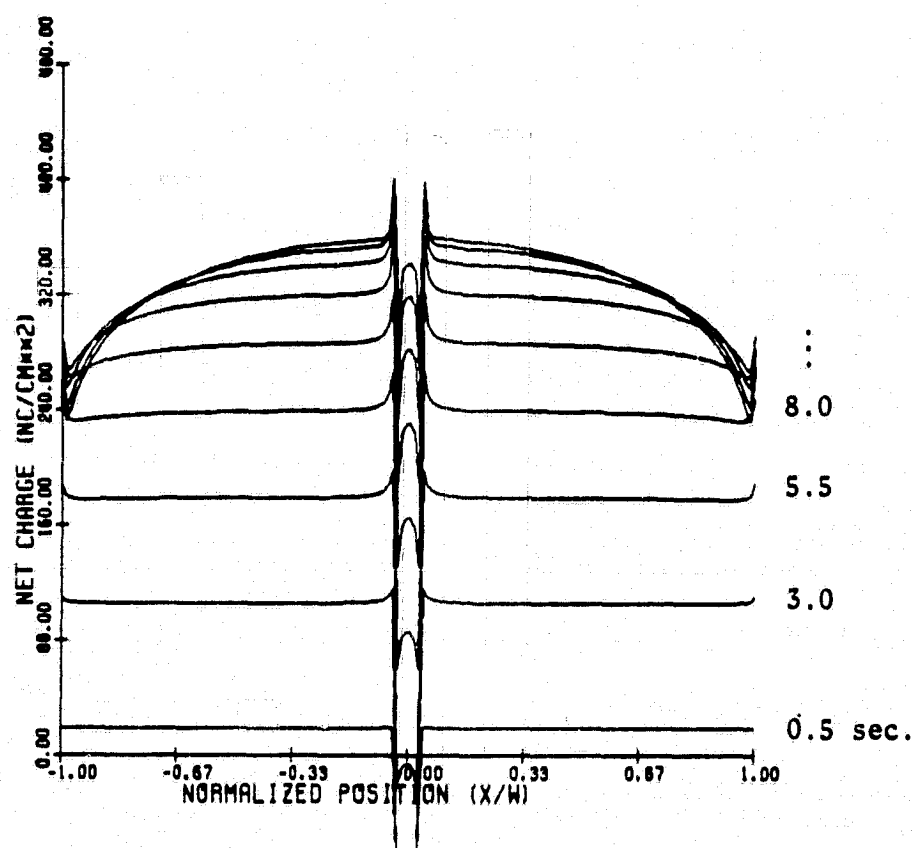


Fig. 6.50 Charging dynamics. Strip 0.047 cm wide, precharged to  $-250 \text{ nC/cm}^2$  (electron charge density). Beam density  $50 \text{ nA/cm}^2$ .



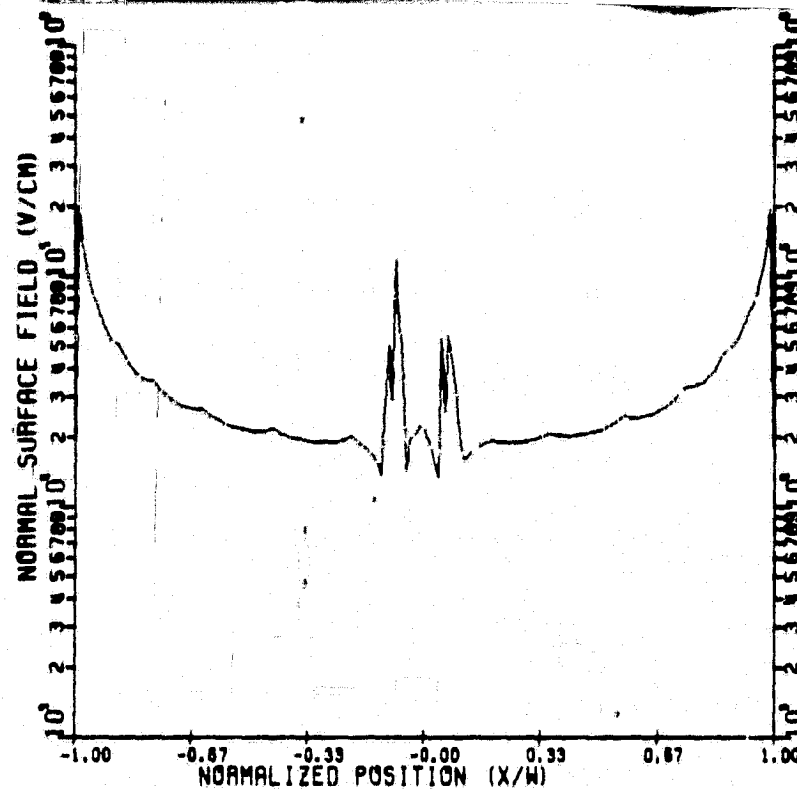


Fig. 6.51 External normal surface field distribution above the final charge profile in Fig. 6.48.

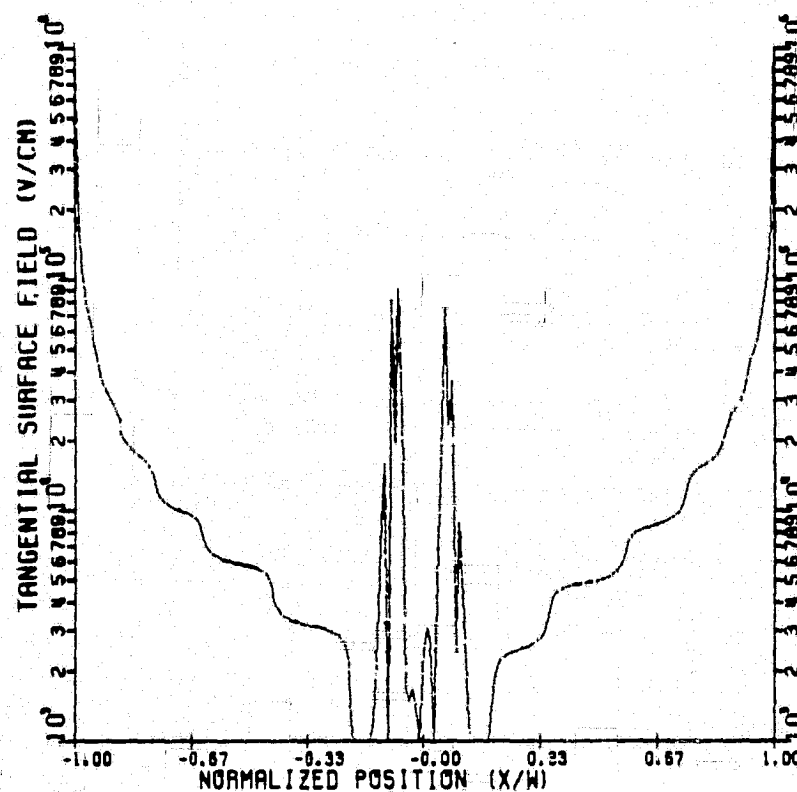


Fig. 6.52 External tangential surface field distribution above the final charge profile in Fig. 6.49.

observed for zero initial conditions, the charging rates across the sample are characteristic of each region's level of development. Near the precharge boundary the net charging rate approximates an average of the neighbouring rates causing highly localized perturbations that persist after the remainder of the surface has obtained equilibrium.

Laboratory experiments in which dielectric films have been brushed before irradiation indicate that the direction of brushing can influence the behaviour of the visible discharge arcs [K.G. Balmain, J.V. Staskus, personal communications]. Multiple arcs that parallel the direction of brushing were produced with either a camel hair brush or a paper tissue along either straight or circular paths.

A possible mechanism for such behaviour can be developed based upon the characteristics described in this section. If the sample were charged along lines parallel to the direction of brushing then irregularities in the developing charge profile could enhance local external surface fields, thus increasing the probability of discharge along these lines. If the discharge event is confined to these high field regions subsequent charging would again develop such conditions along the edge of the discharge region thus perpetuating the area's discharge activity.

#### 6.5.3 Non-uniform Material Thickness

The equilibrium net charge density profiles for a composite material consisting of two adjacent uniform sections with sample thicknesses of 50  $\mu\text{m}$  and 100  $\mu\text{m}$  are indicated in Fig. 6.53 (sections full width 0.75 cm, beam energy 15 keV). The general distribution is in agreement with those conclusions reached in determining the thickness dependence of the charging characteristics (section 6.3).

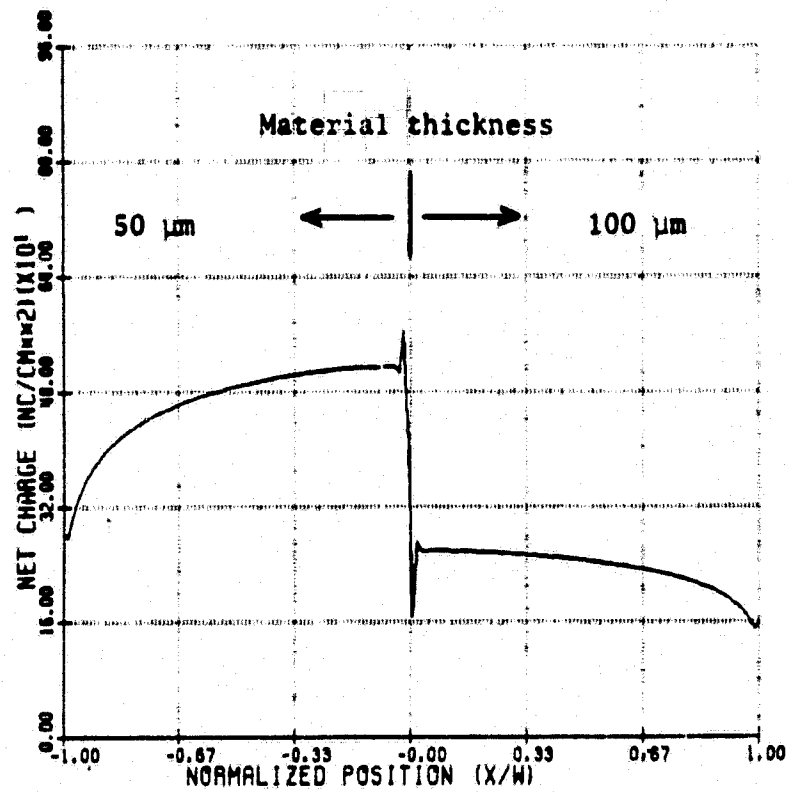


Fig. 6.53 Equilibrium surface charge density distributions.

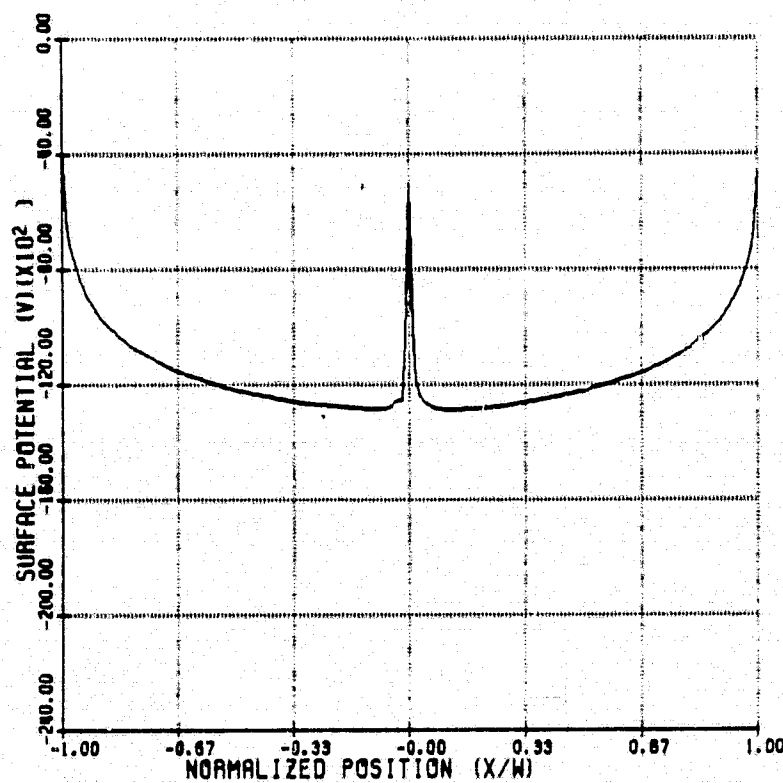


Fig. 6.54 Equilibrium surface potential distributions on non-uniform strip.

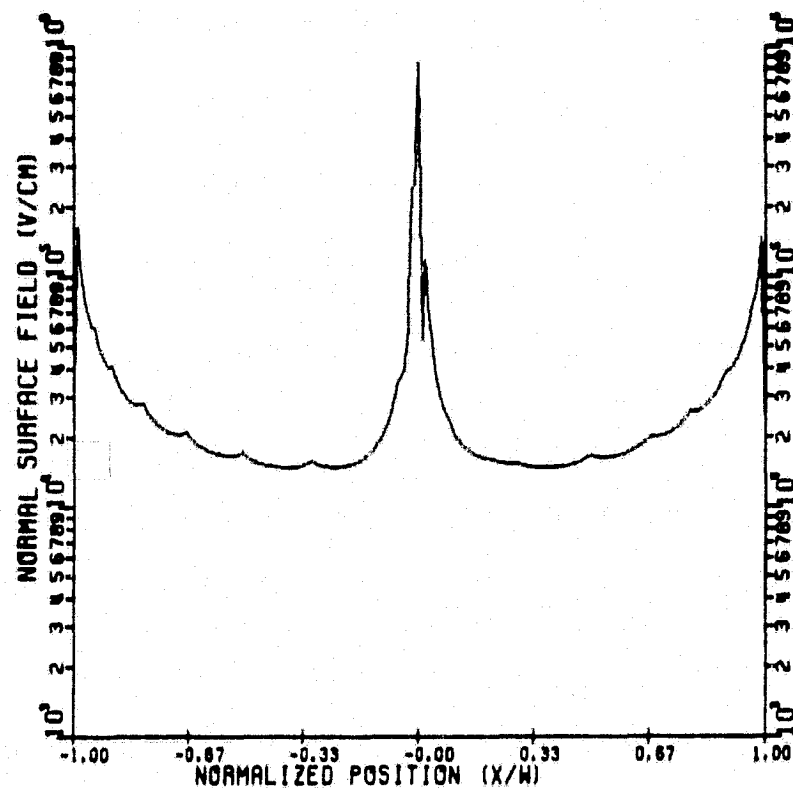


Fig. 6.55 External normal surface field at equilibrium on non-uniform strip.

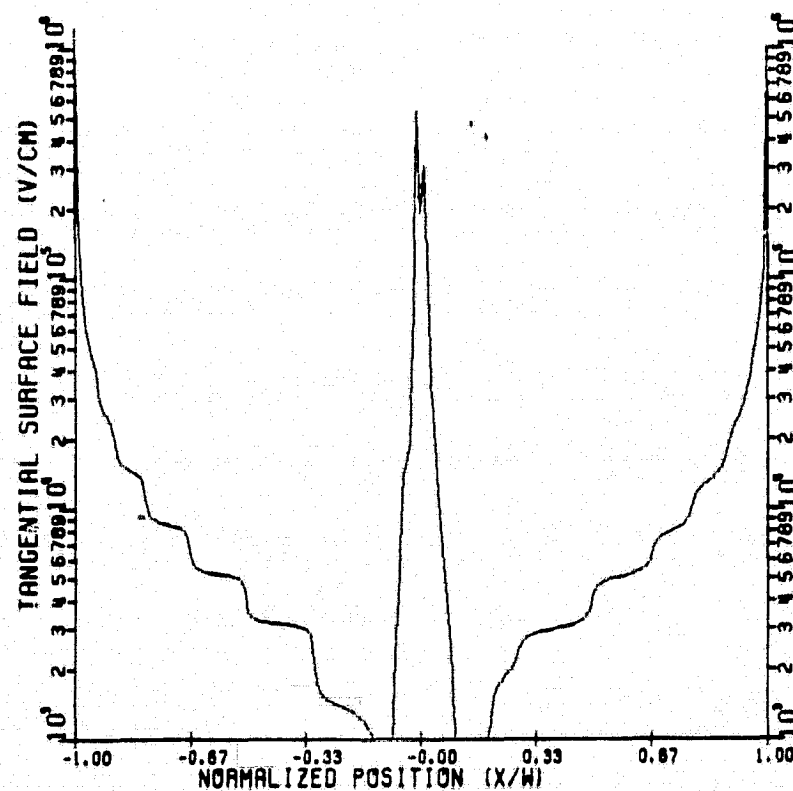


Fig. 6.56 External tangential surface field at equilibrium on non-uniform strip.

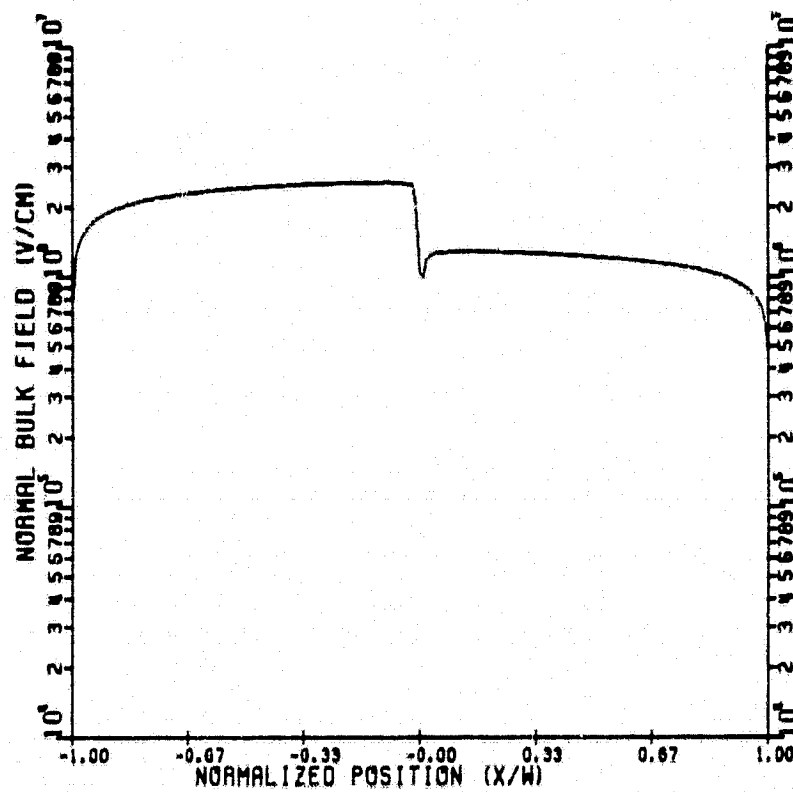


Fig. 6.57 Internal normal bulk field at equilibrium on non-uniform strip.

The resulting surface potential (Fig. 6.54) however resembles that obtained when a gap was present in the material. The external surface fields (Figs. 6.55 and 6.56) also reflect the discontinuity of the material. Both components have maxima occurring at the centre and edges.

The internal bulk field is presented in Fig. 6.57.

#### 6.6 Beam Current Dependence for Kapton

The equilibrium surface potential for Kapton was found to be sensitive to typical beam current densities ( $0.1 - 100.0 \text{ nA/cm}^2$ ) for material thicknesses of the order of  $50 \text{ }\mu\text{m}$  and beam energies near  $20 \text{ keV}$ . As indicated in Fig. 3.2 there exist two distinct regions of equilibrium: emission-limited and conduction-limited. The emission-limited surface potential is independent of the beam current density and the material thickness as is the case for Teflon. Conversely, the conduction-limited process is strongly influenced by both the current density and material thickness. These charging parameters have been chosen in this study to characterize the two-dimensional nature of each limiting mechanism.

Simulations were conducted for thicknesses of  $100 \text{ }\mu\text{m}$  and  $50 \text{ }\mu\text{m}$ , and at current densities of  $100 \text{ nA/cm}^2$  and  $1 \text{ nA/cm}^2$  (material half width  $0.75 \text{ cm}$ , beam energy  $20 \text{ keV}$ ).

The net charge density profiles at equilibrium are presented in Figs. 6.58 and 6.59. The high current thick sample simulation typifies the emission-limited state obtained with the Teflon model. The low current thin sample simulation is conduction-limited and displays a comparatively flat, uniform charge distribution.

The equilibrium surface potential is presented in Figs. 6.60 and 6.61. The conduction-limited potential is constant while at the edges the emission-limited value decreases to less than 50% of its peak central magnitude. As suggested in Chapter 3, Kapton if emission-limited tends to

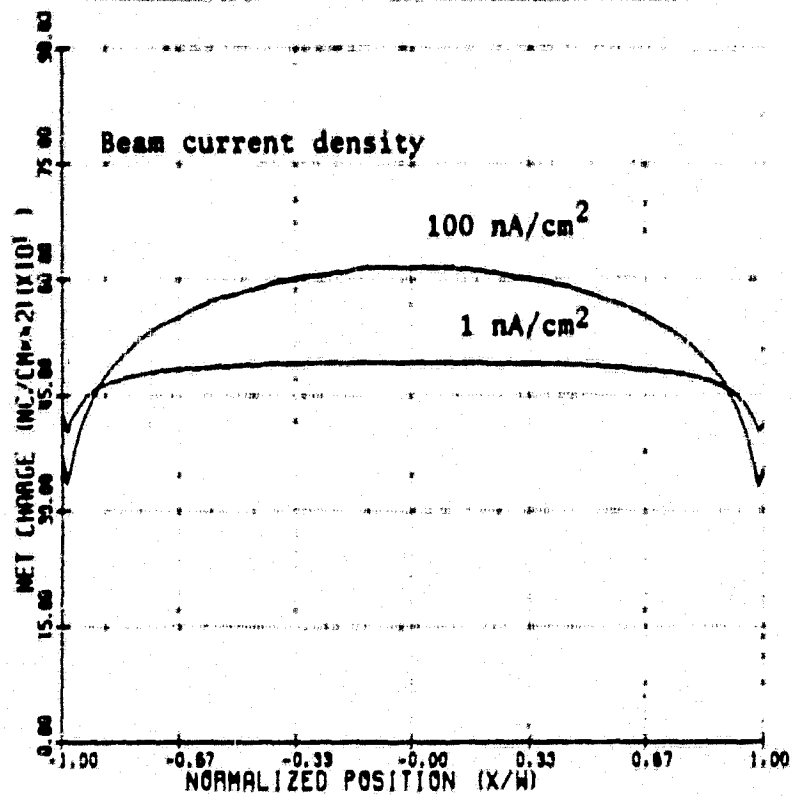


Fig. 6.58 Equilibrium charge density distributions for Kapton. Material thickness 100  $\mu\text{m}$ .

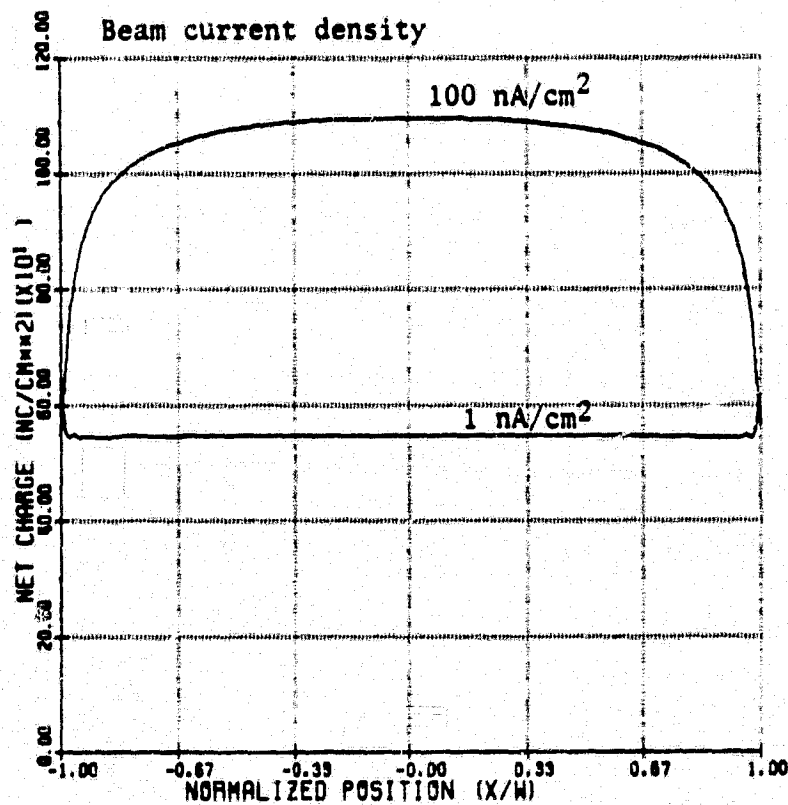


Fig. 6.59 Equilibrium charge density distributions for Kapton. Material thickness 50  $\mu\text{m}$ .

ORIGINAL PAGE IS  
OF POOR QUALITY

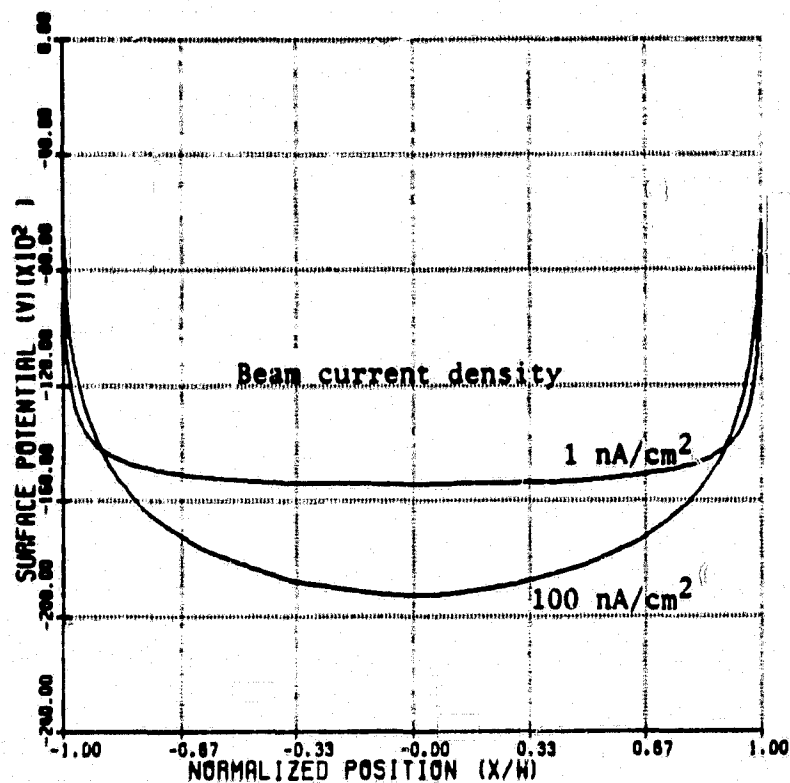


Fig. 6.60 Equilibrium surface potential profiles for Kapton.  
Material thickness 100  $\mu\text{m}$ .

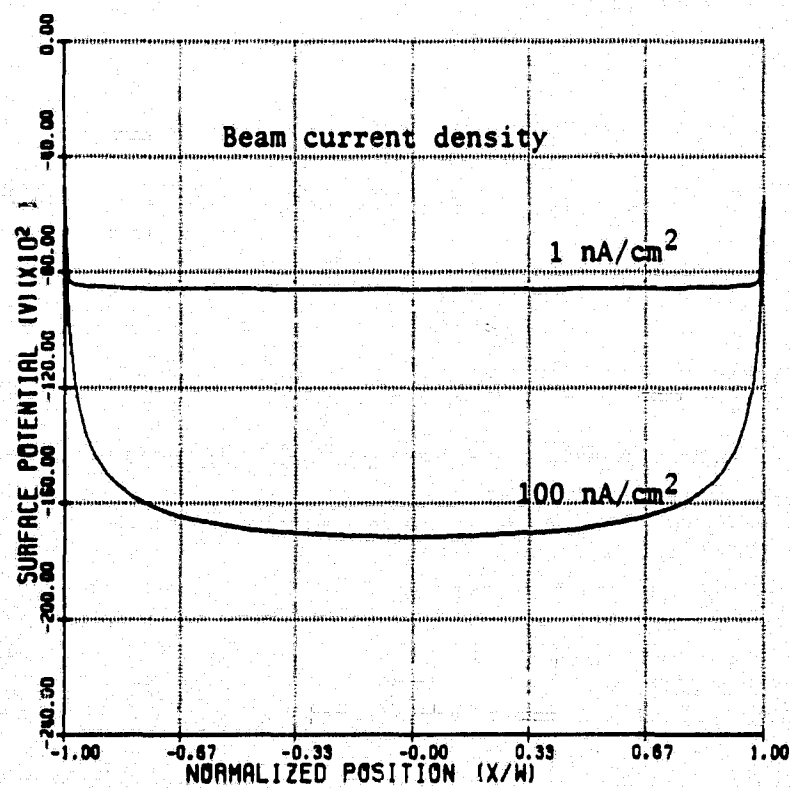


Fig. 6.61 Equilibrium surface potential profiles for Kapton.  
Material thickness 50  $\mu\text{m}$ .



charge to within 1 kV of the beam accelerating voltage compared to 2 kV for Teflon. The deflection of the beam at steady state is therefore greater for Kapton. The angle of incidence graphs (Figs. 6.62 and 6.63) indicate maxima at the edge of almost  $80^\circ$  compared to  $65^\circ$  for comparable Teflon simulations.

The uniformity of the results for conduction-limited charging can be understood in terms of the simplified analysis presented Chapter 5. The incident current density onto a uniform charge distribution was found to be constant over the central portion of the strip as would be the bulk internal fields. The conduction current density, the main charge balancing mechanism, would therefore also be uniform and a consistent equilibrium could be reached under the assumed charge profile.

The external surface normal fields (Figs. 6.64 and 6.65) are comparable to those obtained in the Teflon simulations. The tangential surface fields (Figs. 6.66 and 6.67) suggest that the flat conduction-limited charge distribution produces slightly larger maxima at the edges than does the emission-limited charge distribution.

The internal bulk fields (Figs. 6.68 and 6.69) have broad maxima at the centre of the strip. The internal front face fields (Figs. 6.70 and 6.71) are generally constant across the surface. The incident current density dependence suggested by eq. 3.27,  $J_i^{0.3}$ , is clearly evident. The required surface charge layers are presented in Figs. 6.72 and 6.73.

## 6.7 Tangential Current Results for Kapton

A tangential transfer of charge through an irradiated front surface layer (as outlined in section 4.3) has been implemented for Kapton in the following charging simulations. Two separate edge boundary conditions were investigated:  $\partial J_z / \partial z = 0$  and  $J_z = 0$ . The term zero edge resistance is used to describe the first case where there can be no charging at the

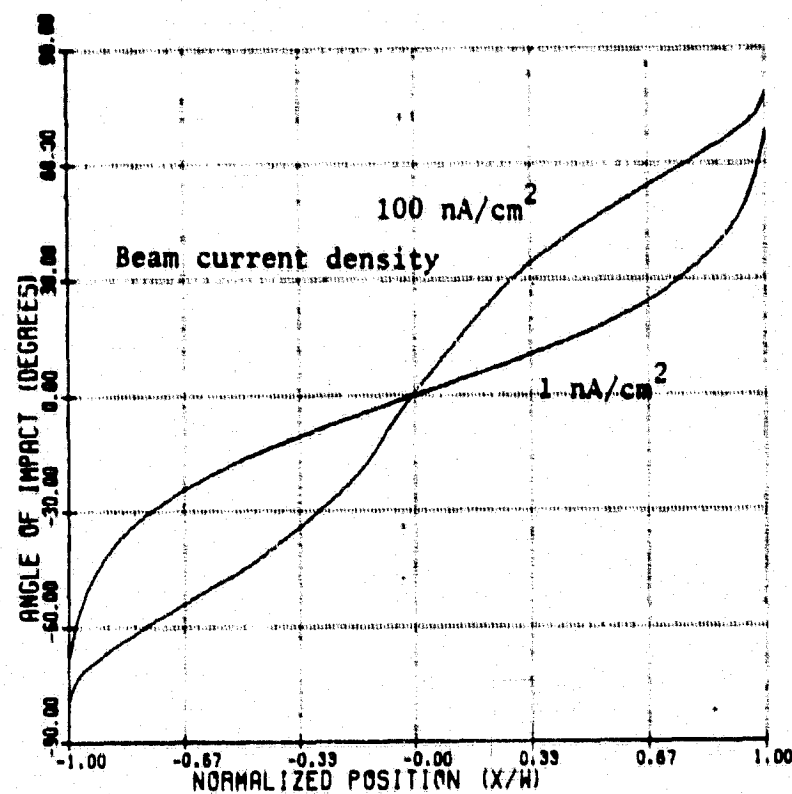


Fig. 6.62 Angle of incidence at equilibrium for Kapton.  
Material thickness 100  $\mu\text{m}$ .

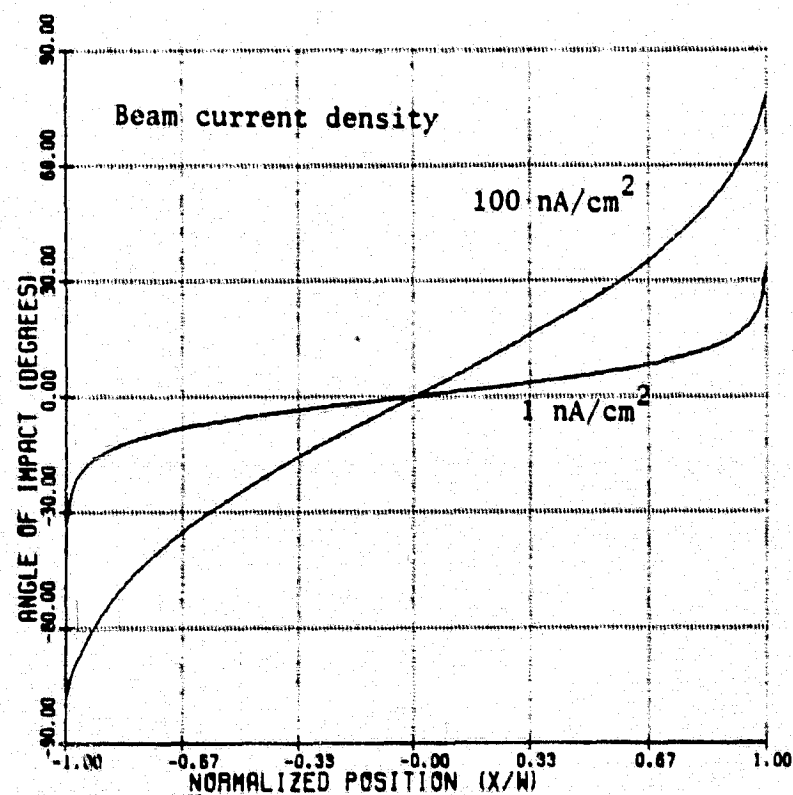


Fig. 6.63 Angle of incidence at equilibrium for Kapton.  
Material thickness 50  $\mu\text{m}$ .

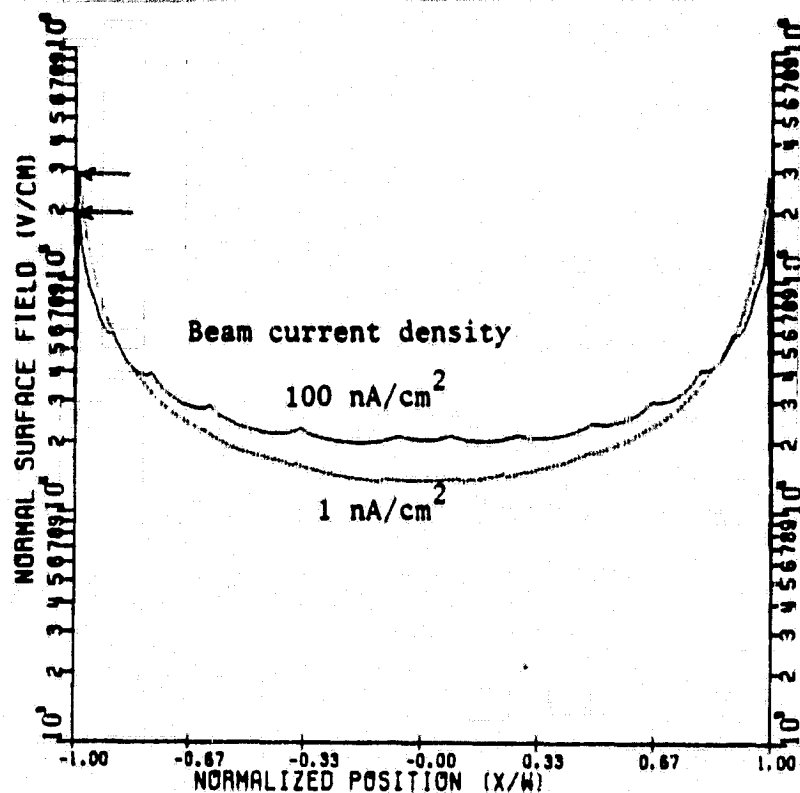


Fig. 6.64 Normal surface field at equilibrium for Kapton. Material thickness 100 μm.

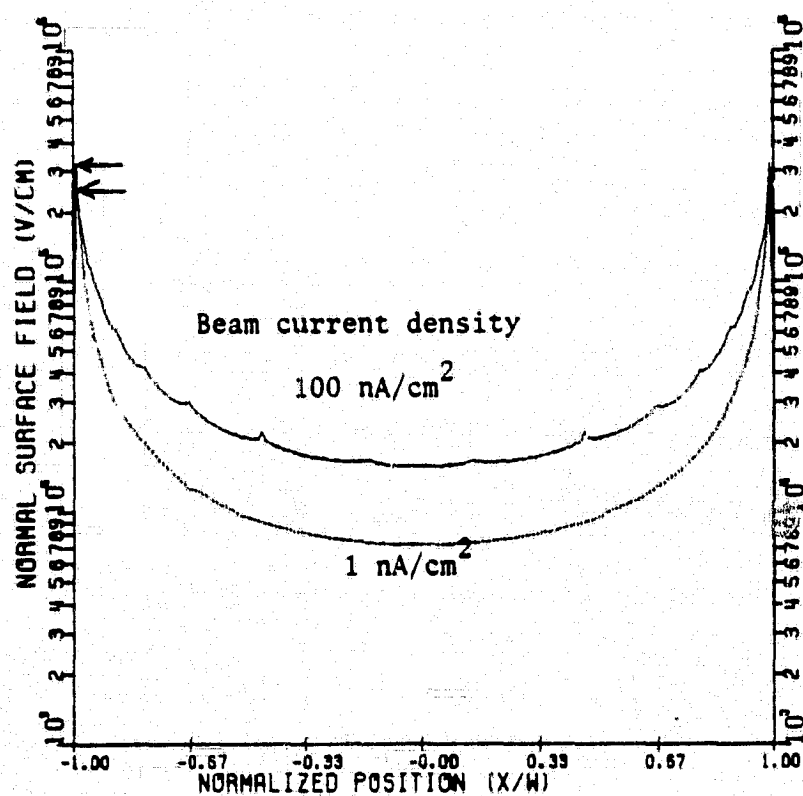


Fig. 6.65 Normal surface field at equilibrium for Kapton. Material thickness 50 μm.

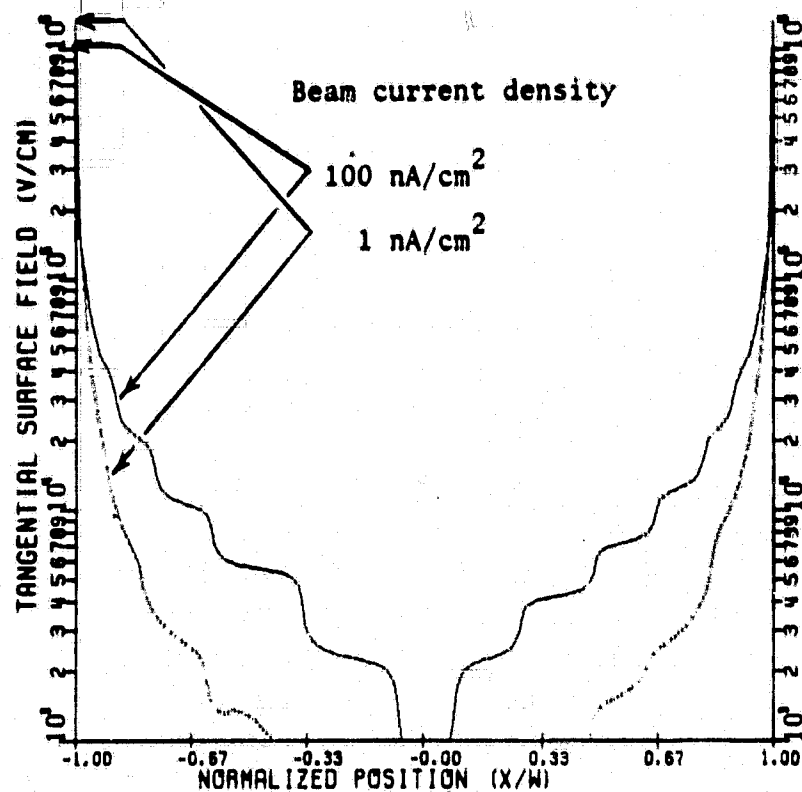


Fig. 6.66 External tangential surface field at equilibrium for Kapton. Material thickness 100  $\mu\text{m}$ .

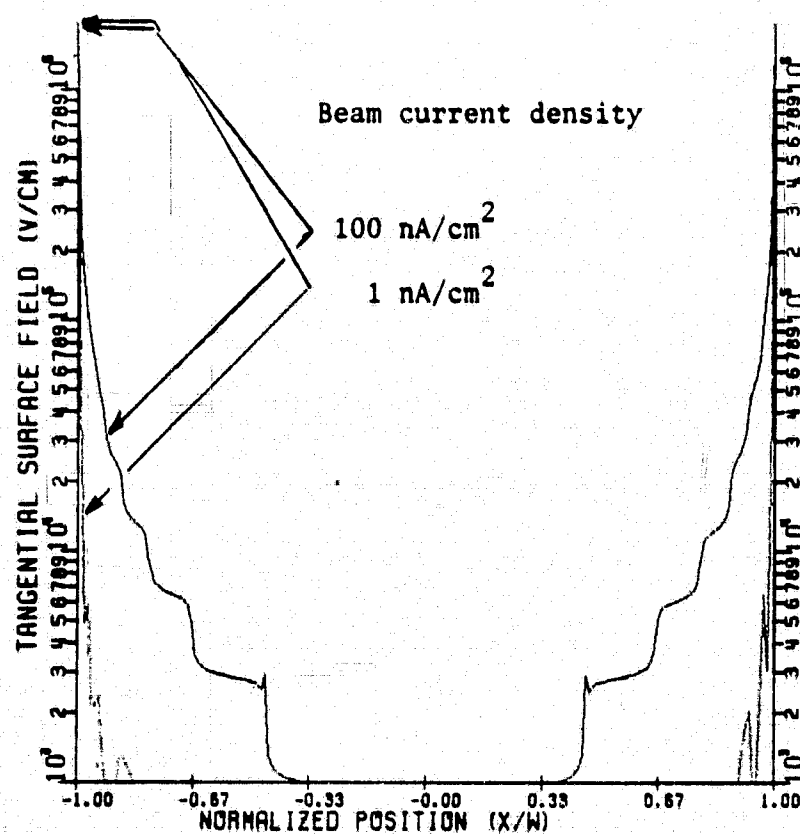


Fig. 6.67 External tangential surface field at equilibrium for Kapton. Material thickness 50  $\mu\text{m}$ .

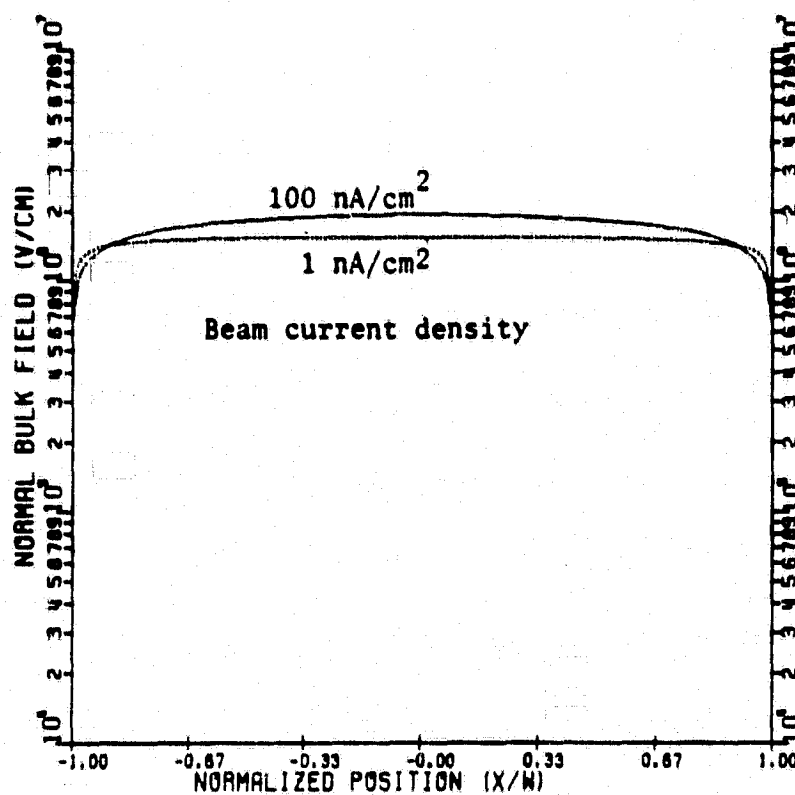


Fig. 6.68 Internal normal bulk field at equilibrium for Kapton.  
Material thickness 100 μm.

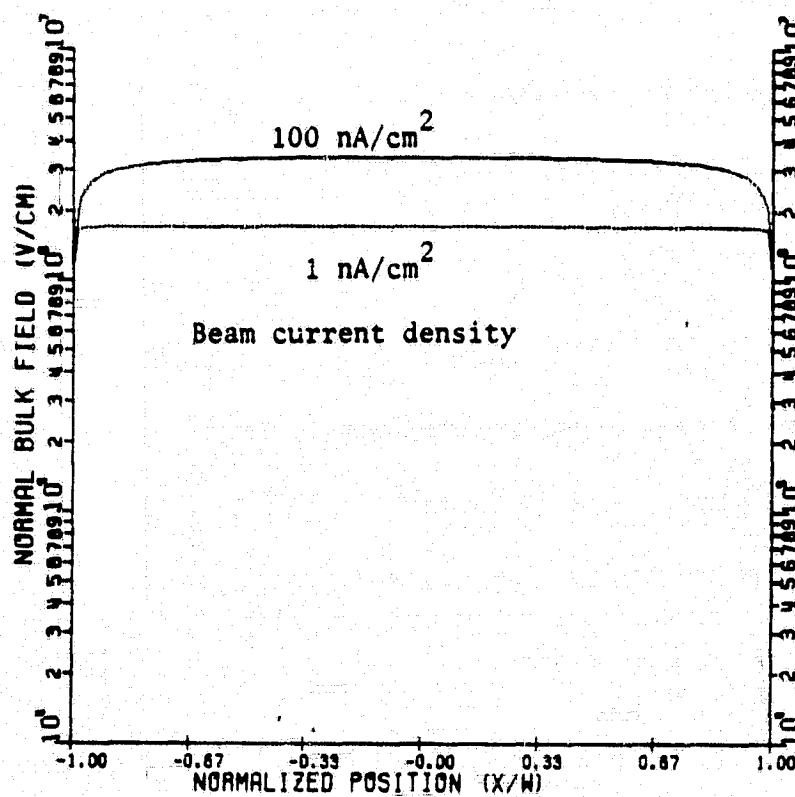


Fig. 6.69 Internal normal bulk field at equilibrium for Kapton.  
Material thickness 50 μm

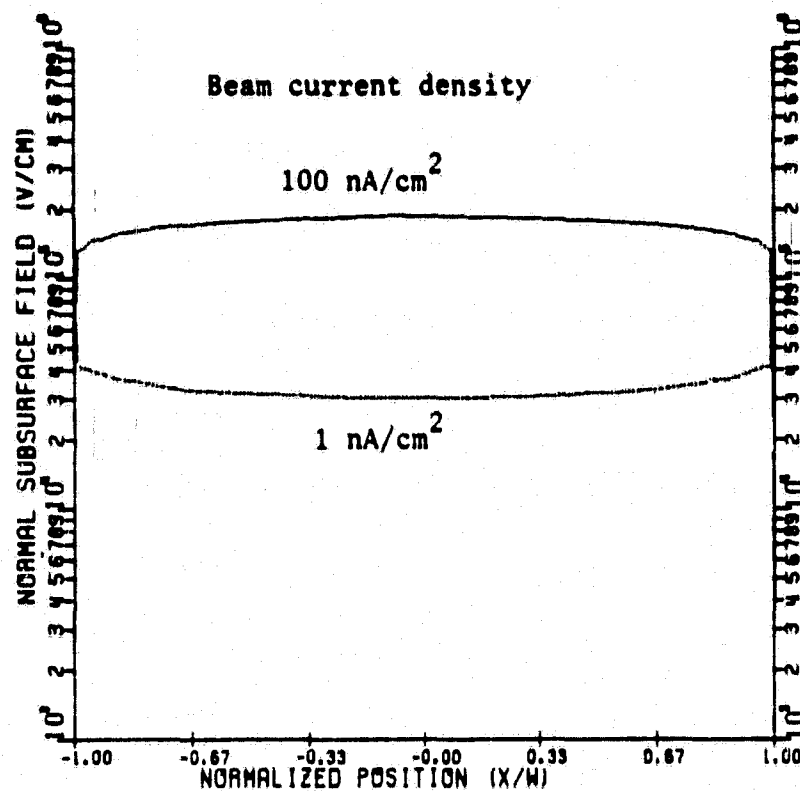


Fig. 6.70 Internal front face field at equilibrium for Kapton.  
Material thickness 100 μm.

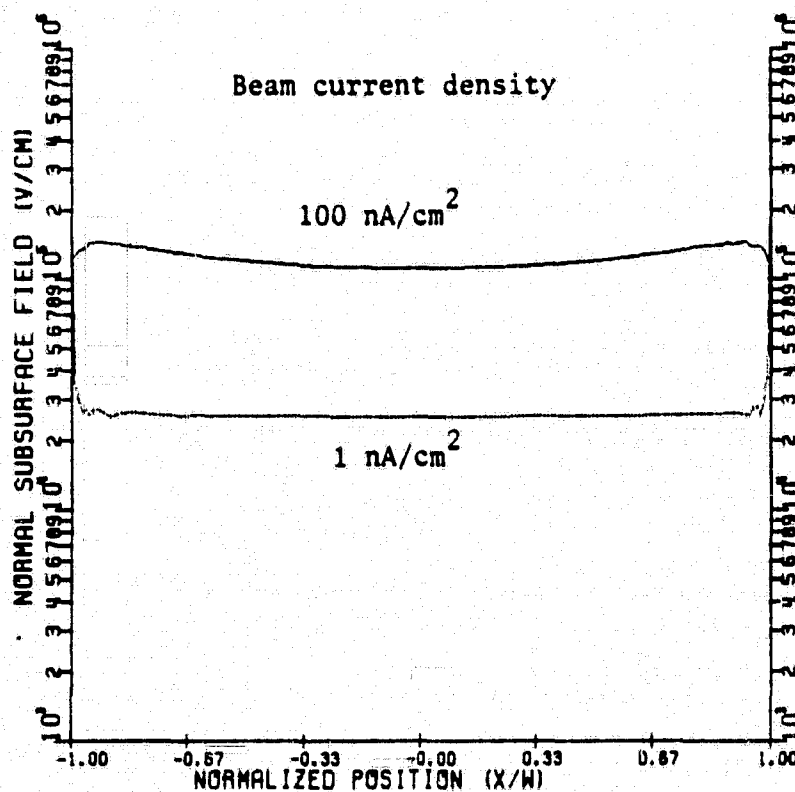


Fig. 6.71 Internal front face field at equilibrium for Kapton.  
Material thickness 50 μm.

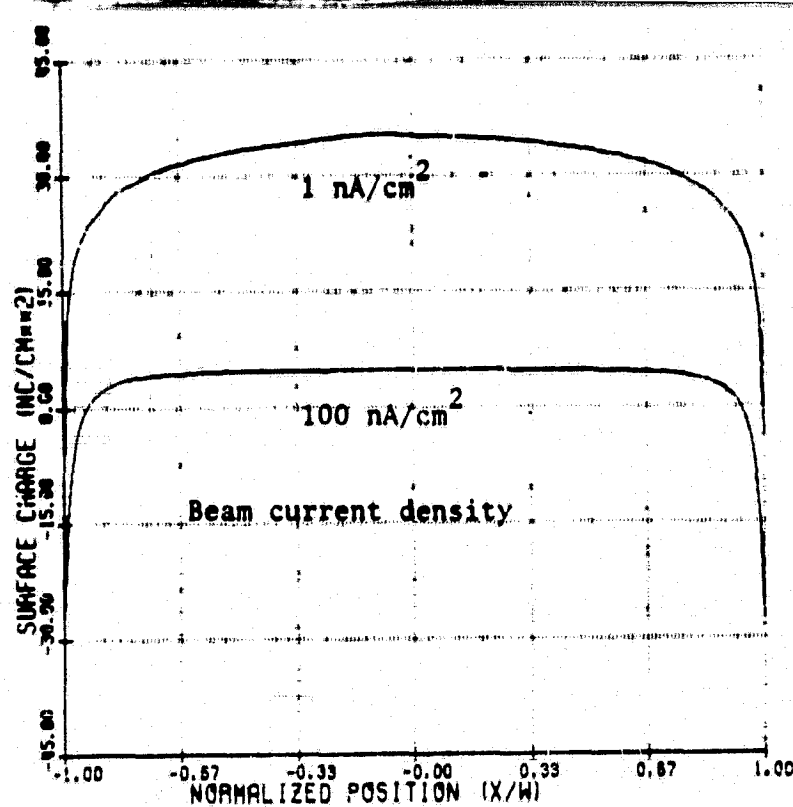


Fig. 6.72 Front face charge density distributions at equilibrium for Kapton. Material thickness 100  $\mu\text{m}$ .

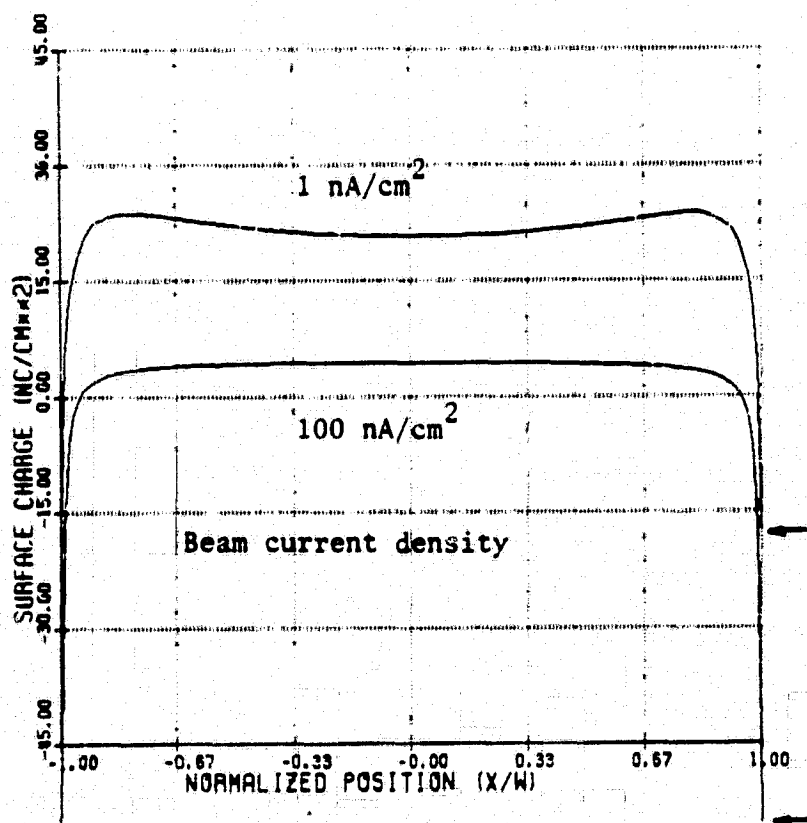


Fig. 6.73 Front face charge density distributions at equilibrium for Kapton. Material thickness 50  $\mu\text{m}$ .

edge due to transverse currents. The term infinite edge resistance is used to refer to the latter condition. The field gradient at the edge to be used in the calculation (eq. 4.18) is made between the edge and the adjacent material data point.

The material half width and the beam energy were kept constant at 0.75 and 20 keV respectively as was the case in section 6.5. Each boundary condition was tested on two models corresponding to emission-limited and conduction-limited conditions (material thicknesses 100  $\mu\text{m}$  and 50  $\mu\text{m}$ , beam current density 100  $\text{nA}/\text{cm}^2$  and 1  $\text{nA}/\text{cm}^2$  respectively).

The charging dynamics are presented at equal time intervals in Figs. 6.74, 6.75, 6.76, 6.77, 6.78 and 6.79. The results for an infinite edge resistance show no noticeable deviation from the curves generated for no transverse currents. With the exception of a slight depression at the edge the results for zero edge resistance also indicate no deviation.



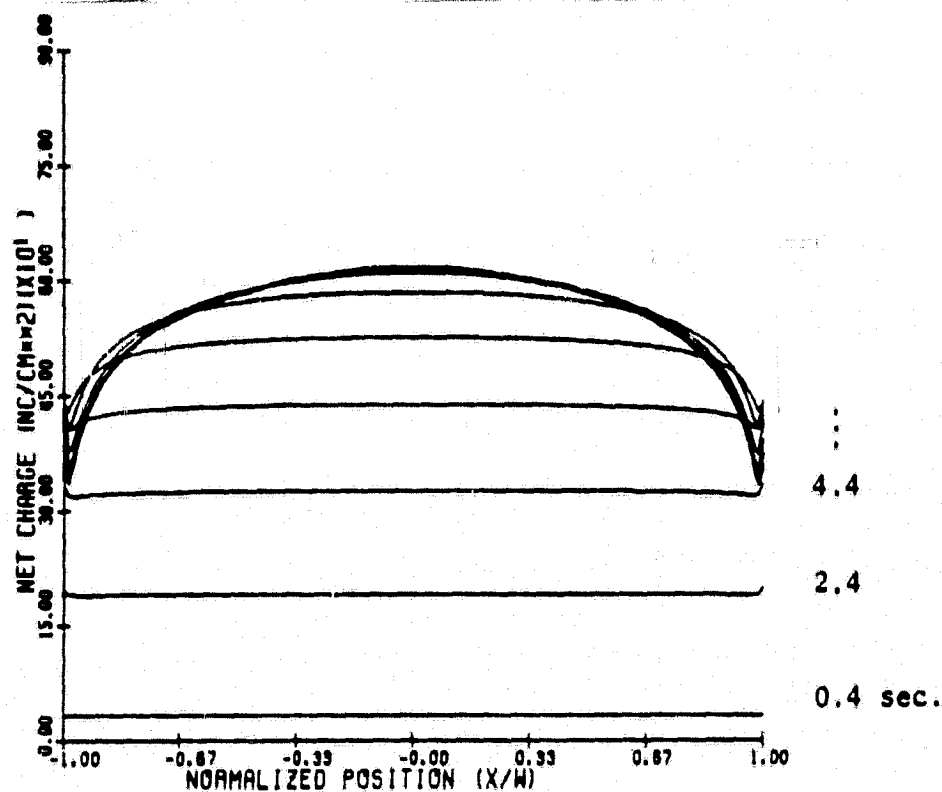


Fig. 6.74 Charging dynamics for Kapton. Material thickness 100  $\mu\text{m}$ , current density 100  $\text{nA}/\text{cm}^2$ . No tangential currents.

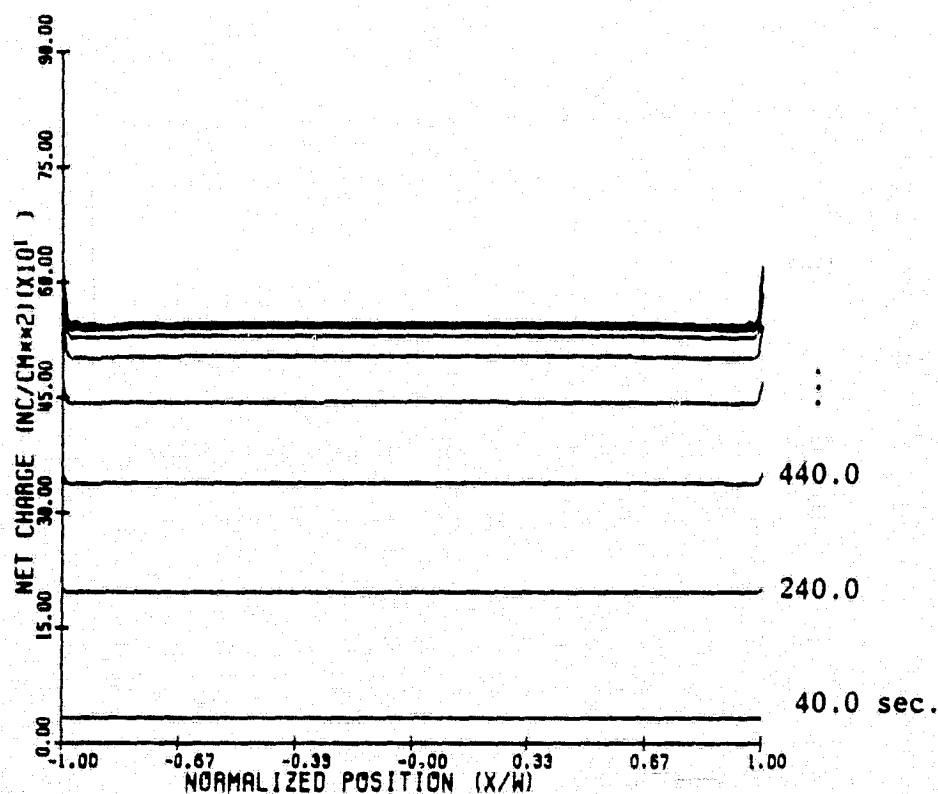


Fig. 6.75 Charging dynamics for Kapton. Material thickness 50  $\mu\text{m}$ , current density 1  $\text{nA}/\text{cm}^2$ . No tangential current.

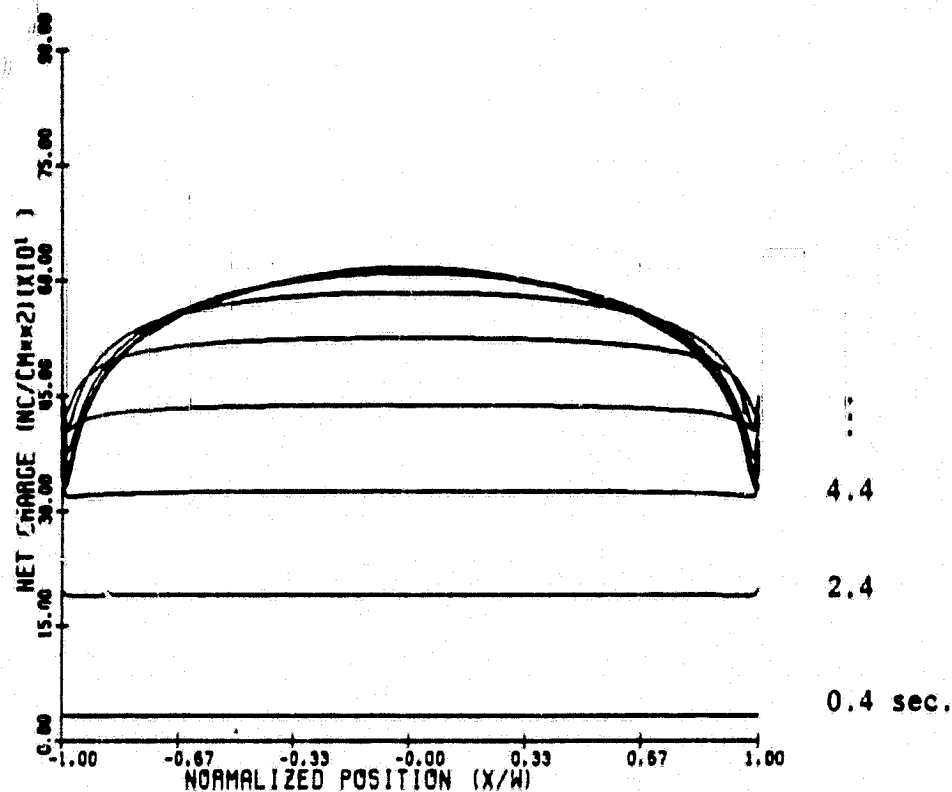


Fig. 6.76 Charging dynamics for Kapton. Material thickness 100  $\mu\text{m}$ , current density 100  $\text{nA}/\text{cm}^2$ . Tangential currents with boundary condition  $J_z=0$ .

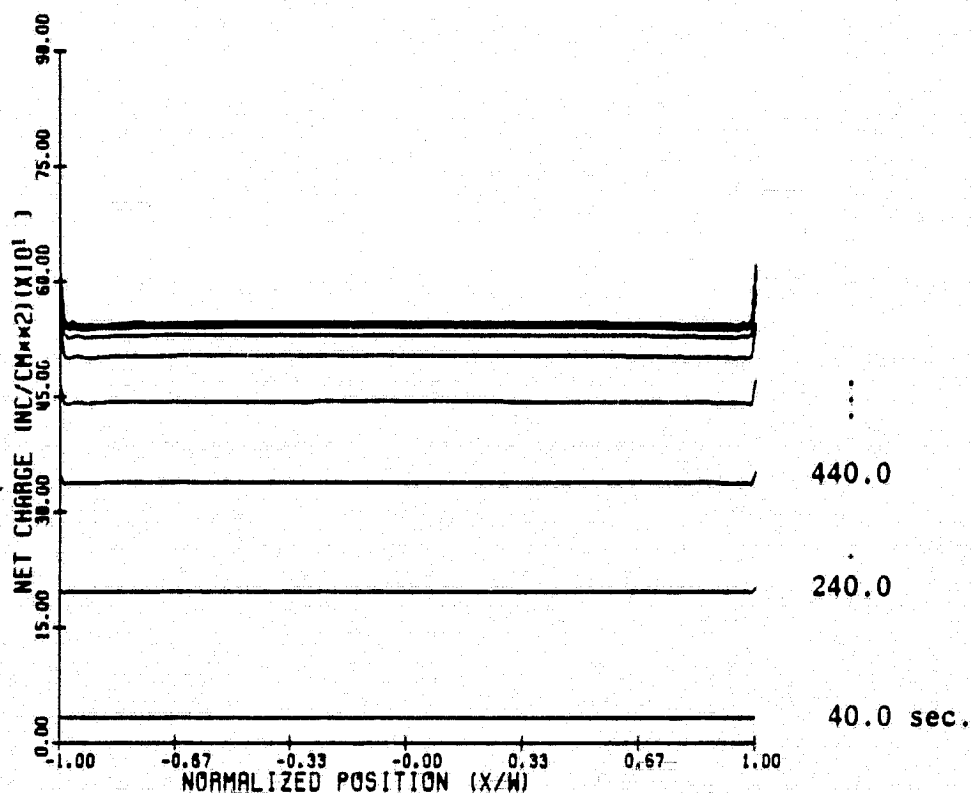


Fig. 6.77 Charging dynamics for Kapton. Material thickness 50  $\mu\text{m}$ , current density 1  $\text{nA}/\text{cm}^2$ . Tangential currents with boundary condition  $J_z=0$ .

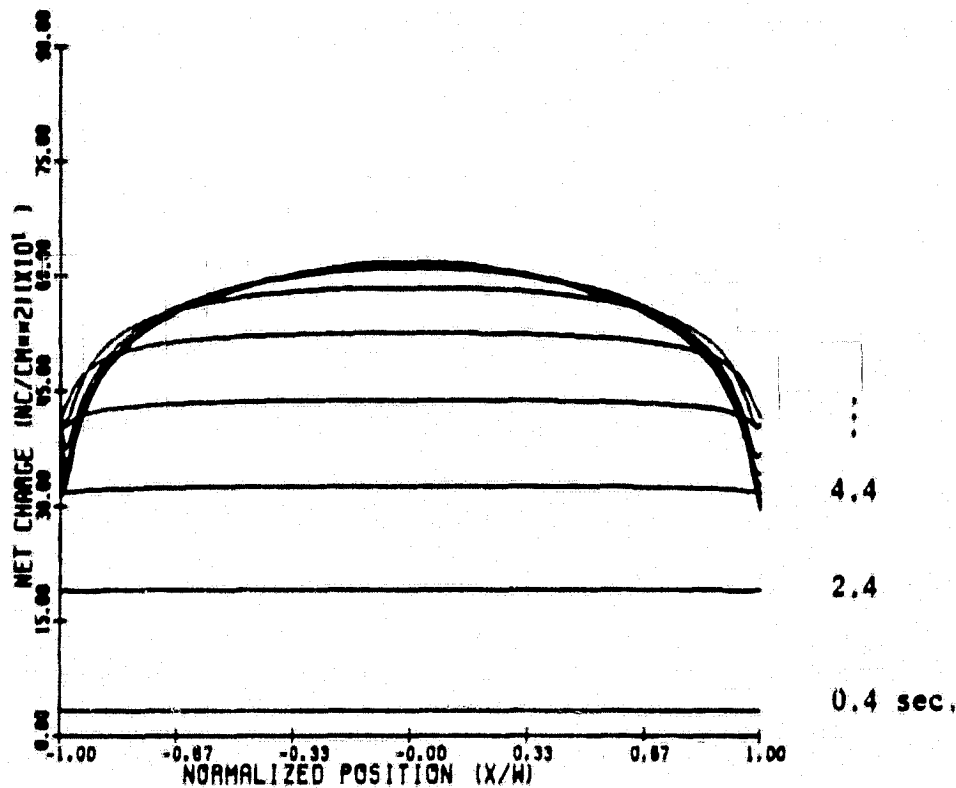


Fig. 6.78 Charging dynamics for Kapton. Material thickness 100 μm, current density 100 nA/cm². Tangential currents with boundary condition  $\partial J_z / \partial z = 0$ .

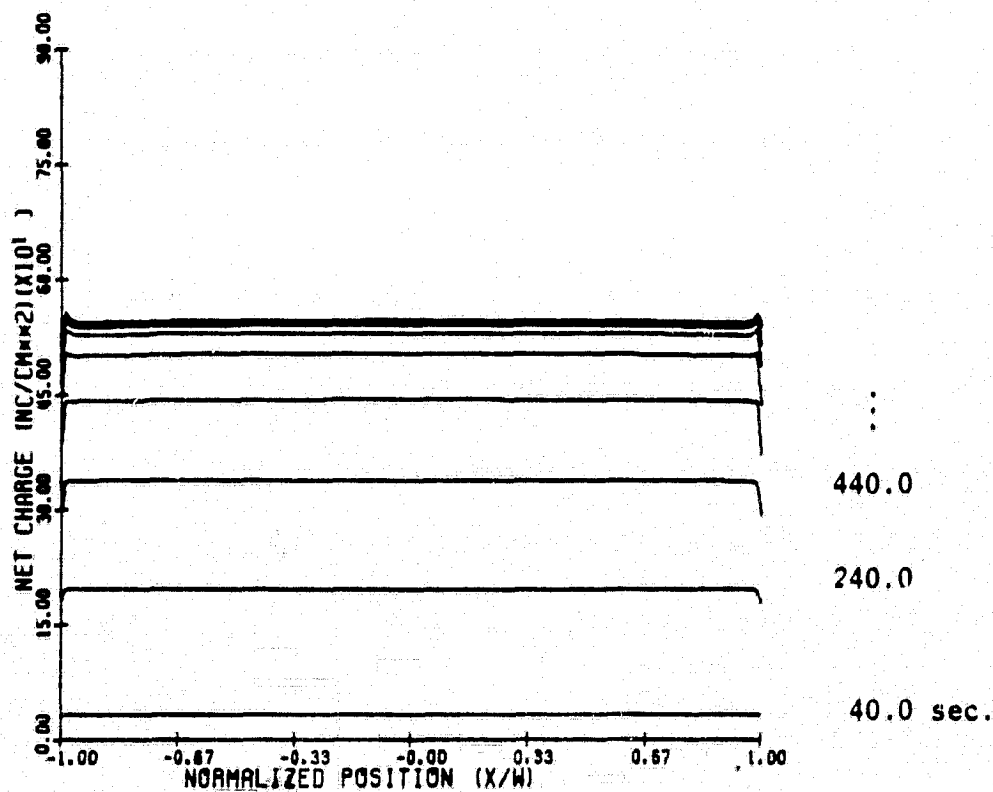


Fig. 6.79 Charging dynamics for Kapton. Material thickness 50 μm, current density 1 nA/cm². Tangential currents with boundary condition  $\partial J_z / \partial z = 0$ .

## 7. CONCLUSIONS

A two-dimensional model has been presented to describe the accumulation of charge on long, planar dielectric strips by a uniform monoenergetic electron beam used to simulate spacecraft charging conditions. Numerical results detail the net surface charge density, surface potential and material field profiles for both Teflon and Kapton. Teflon has been treated as being completely emission-limited whereas Kapton is governed by both emission and conduction currents. The response of both materials under a variety of charging conditions has been investigated.

The equilibrium state can be categorized as being either edge-like or centre-like. The edge, under normal charging conditions, is characterized by maxima in both the normal and tangential components of the external surface electric field and by minima in the surface charge density and surface potential. In general, the total external surface field at the edge is dominated by the tangential component. The centre is characterized by a maximum in both the internal bulk electric field and the net surface charge density, and by a minimum in both components of the external surface fields.

The one-dimensional analysis of Chapter 3 adequately describes the behaviour of the centre region whereas a complete two dimensional model is necessary at the edge. In the course of this study a positive correlation has been established between the edge-like regions and the apparent sites of discharge initiation and blow off whereas punchthrough discharges can be associated with the high internal bulk fields at the centre.

For emission limited charging and normal beam incidence it was found that the maximum surface and bulk fields were approximately proportional to the beam energy. The internal normal bulk field was found to be inversely proportional to the material thickness  $d$  and independent of the

material halfwidth  $W$ . The maximum edge tangential field was found to vary as  $(d)^{-0.61}$  and  $(W)^{-0.33}$ . The location of the maximum field in the material therefore depends on the ratio  $W/d$ . If  $W/d \leq 20$  the maximum material field is the surface tangential component at the edge; otherwise the maximum is the internal normal bulk component located at the centre of the strip.

The maximum bulk field was found to be independent of the beam angle whereas the peak tangential field at the edge nearest the beam source varied as  $10^{0.0104\theta}$  where  $\theta$  is in degrees. The location of the maximum bulk field corresponds to the point where the electrons impact the surface at  $0^\circ$  and was found to shift toward the near edge for increasing beam angles. The charge distribution for non-normal incidence was also found to shift toward the edge nearest the electron source. For angles greater than  $15^\circ$  the maximum charge density was found at the near edge.

The surface potential and field profiles were found to be functions of the normalized coordinate  $z/W$  over most of the sample surface. These quantities therefore can be described by a single scale length over a broad range of charging conditions.

The external field quantities except at the edge were found to be largely independent of the sample thickness  $d$ . The internal bulk normal field was found to be inversely proportional to  $d$ .

The simulation describing the charging of a specimen split by a central slot resembled that found for a uniform specimen over most of its surface. A region of charge accumulation near the slot edges is strongly influenced by the relative slot width. For large slots the profiles should evolve toward those describing two decoupled regions. External surface fields in the neighbourhood of the slot were found to be largely independent of the slot size and resembled the corresponding edge fields.

The precharging simulations suggest that highly localized perturba-

tions in the charge distribution could persist after most of the surface has attained a steady state.

The nonuniform material simulations suggest large surface fields can develop in the neighbourhood of the thickness transition.

The Kapton model, under emission-limited or conduction-limited charging conditions, produced two very different cross-sectional profiles. The conduction-limited cases produced a flat, uniform charge distribution whereas the emission-limited cases produced a broad central maximum. Maximum external surface fields were comparable although the tangential component associated with conduction-limited charging was very strongly localized at the edge.

The inclusion of tangential currents for Kapton had very little effect on the equilibrium state. No attempt was made to model a separate inherent surface conductivity.

The internal front face field was found to be nearly constant for most simulations. Its magnitude was significantly smaller than the peak surface or bulk fields for both Teflon and Kapton under typical charging conditions.

## REFERENCES

- Adamec, V. and Calderwood, J.H. (1975), Electrical Conduction in Dielectrics at High Fields, *Journal of Physics D*, Vol. 8, 551-560.
- Adamo, R.C., Nanevich, J.E. and Grier, N. (1977), Conductivity Effects in High-Voltage Spacecraft Insulating Materials, *Proceedings of the Spacecraft Charging Technology Conference*, Eds. C.P. Pike and R.R. Lovell, NASA TMX-73537, 669-686.
- Amborski, L.E. (1963), H-film a new high temperature dielectric, *Industry and Engineering Chemical Products Research and Development*, Vol. 2, 189.
- Aron, P.R. and Staskus, J.V. (1979), Area Scaling Investigations of Charging Phenomena, *Spacecraft Charging Technology-1978*, NASA CP-2071, 485-506.
- Ausloos, P. (1968), *Fundamental Processes in Radiation Chemistry*, Interscience Publishers, New York.
- Balmain, K.G. and Hirt, W. (1980), Dielectric Surface Discharges: Dependence on Incident Electron Flux, *IEEE Trans. on Nuclear Science*, Vol. NS-27, No. 6, 1770-1775.
- Balmain, K.G. and Dubois, G.R. (1979), Surface Discharges on Teflon, Mylar and Kapton, *IEEE Trans on Nuclear Science*, Vol. NS-26, No. 6, 5146-5151.
- Balmain, K.G. (1978), Scaling Laws and Edge Effects for Polymer Surface Discharges, *Spacecraft Charging Technology-1978*, NASA CP-2071, 646-656.
- Beers, B.L. Pine, V.W. and Ives, S.T. (1981), Internal Breakdown of Charged Spacecraft Dielectrics, paper presented at the 1981 IEEE Annual Conference on Nuclear and Space Radiation Effects, Seattle.
- Beers, B.L., Delmer, T.W. and Pine V.W. (1980), Theoretical Support for Arc Discharge Experiments, report prepared for SRI International, Beers Associates Inc., March 1980.
- Beers, B.L., Hwang, H., Lin, D.L. and Pine V.W. (1979), Electron Transport Model of dielectric Charging, *Spacecraft Charging Technology-1978*, NASA CP 2071, 209-238.
- Bosma, J. and Levadou, F. (1979), Electrostatic Charging and Space Materials, *Proceedings of an ESA Symposium on Spacecraft Materials*, ESA SP-145, 189-207.
- Budd, P.A. (1981), Secondary Electron Emission from Electrically Charged Fluorinated-Ethylene-Propylene Teflon for Normal and Non-normal Electron Incidence, Technical Report NASA Grant No. NSG-3166.
- Burke, E.A. (1980), Secondary Emission from Polymers, *IEEE Trans. on Nuclear Science*, NS-27, 1760-1764.
- Burke, E.A., Wall, J.A. and Frederickson A.R. (1972), Radiation Induced Low Energy Emission from Metals, *IEEE Trans. on Nuclear Science*, NS-19, 193-198.

- Cuchanski, M. (1978), Simulation Studies of Charging, Discharging and Discharge Pulse Propagation on Spacecraft Materials and Structures, M.A.Sc. Thesis, University of Toronto, Toronto, Canada.
- Darlington, E.H. (1975), Backscattering of 10-100 keV from Thick Targets, *Journal of Physics D*, Vol. 8, 85-93.
- Davies, D.K. (1979), The Charging and Discharging of Spacecraft Dielectrics, *Proceedings of an ESA Symposium on Spacecraft Materials*, ESA SP-145, 217-221.
- DeForest, S.E. (1972), Spacecraft Charging at Synchronous Orbit, *Journal of Geophys. Res.*, 77, 651.
- Feder, J. (1976), Storage and Examination of High-Resolution Charge Images on Teflon Foils, *Journal of Applied Physics*, Vol. 47, No. 5, 1741-1745.
- Flanagan, T.M., Denson, R., Mallon, C.E., Treadaway, M.J. and Wenaas, E.R. (1979), Effect of Laboratory Simulation Parameters on Spacecraft Dielectric Discharges, *IEEE Trans. on Nuclear Science*, Vol. NS-26, 5134-5140.
- Frederickson, A.R. (1979), Electric Fields in Irradiated Dielectrics, *Spacecraft Charging Technology Conference-1978*, NASA CP 2071, 554-569.
- Gross, B. (1980), Radiation-induced Charge Storage and Polarization Effects, in *Topics in Applied Physics, Electrets*, Vol. 33, Ed: G.M. Sessler, Springer-Verlag, 217-252.
- Gross, B. and Leal Ferreira (1979), Analytic Solution for Radiation-induced Charging and Discharging of Dielectrics, *Journal of Applied Physics*, Vol. 50, No. 3, 1506-1511.
- Gross, B., Sessler, G.M. and West, J.E. (1977), Location of Charge Centroid in Electron-beam-charged Polymer Films, *Journal of Applied Physics*, Vol. 48, No. 10, 4303-4306.
- Gross, B., Sessler, G.M. and West J.E. (1974), Charge Dynamics for Electron-irradiated polymer-foil electrets, *Journal of Applied Physics*, Vol. 45, No. 7, 2841-2851.
- Gross, B., Sessler, G.M. and West, J.E. (1974a), Radiation Hardening and Pressure Actuated Charge Release of Electron-irradiated Teflon Electrets, *Applied Physics Letters*, Vol. 24, No. 8, 351-353.
- Gross, B. (1957), Irradiation Effects in Borosilicate Glass, *Phys. Rev.*, Vol. 107, No. 2, 368-373.
- Hanscomb, J.R. and Calderwood, J.H. (1973), Thermally Assisted Tunnelling in Polyimide Film Under Steady-state and Transient Conditions, *Journal of Physics D*, Vol. 6, 1093-1104.
- Harrower, G.A. (1956), Energy Spectra of Secondary Electrons, *Physical Review*, Vol. 104, 52.
- Hirshberg, J. and Colburn, D.S. (1969), Interplanetary Field and Geomagnetic Variations: A Unified View, *Planet. Space Sci.*, 17, 1183.



- Inouye, G.T. (1976), Spacecraft Potentials in a Substorm Environment, in Spacecraft Charging by Magnetospheric Plasmas, Ed. A. Rosen, Progress in Astronautics and Aeronautics, 47, 103-120.
- Jordan, E.C. and Balmain K.G. (1968), Electromagnetic Waves and Radiating Systems, Second Edition, Prentice-Hall Inc., New Jersey.
- Katz, I., Cassidy, J.J., Mandell, M.J., Schnuelle, G.W., Steen, P.G. and Roche, J.C. (1979), The Capabilities of the NASA Charging Analyser Program, Spacecraft Charging Technology-1978, NASA CP-2071, 101-122.
- Katz, I., Parks, D.E., Mandell, M.J., Harvey, J.M., Brownell, D.H., Wang, S.S. and Rotenberg, M. (1977), A Three Dimensional Dynamic Study of Electrostatic Charging in Materials, NASA-CR 135256.
- Kinney, G.F. (1957), Engineering Properties of Plastics, Wiley.
- Koons, H.C. (1980), Characteristics of Electrical Discharges on the P78-2 Satellite (SCATHA), AIAA Paper 80-0333, Jan. 1980.
- Mandell, M.J., Katz, I., Schnuelle, G.W., Steen, P.G. and Roche, J.C. (1978), IEEE Trans. in Nuclear Science, Vol. NS-25, No. 6, 1313-1317.
- Marshall, J.S. and Ward, A.G. (1937), Canadian Journal of Research, A15, 39.
- McPherson, D.A. and Schober, W.R. (1976), Spacecraft Charging at High Attitudes: The Scatha Satellite Program, in Spacecraft Charging by Magnetospheric Plasmas, Ed. A. Rosen, Progress in Astronautics and Aeronautics, 47, 15-30.
- Meulenberg, A. (1976), Evidence for a New Discharge Mechanism for Dielectrics in Plasma, in Spacecraft Charging by Magnetospheric Plasmas, Ed. A. Rosen, Progress in Astronautics and Aeronautics, 47, 237-246.
- de Oliveira, L.N. and Gross, B. (1975), Space-charge-limited Currents in Electron-irradiated dielectrics, Journal of Applied Physics, Vol. 46, No. 7, 3132-3138.
- Purvis, C.K., Staskus, J.V., Roche, J.C. and Berkopce, F.D. (1979), Charging Rates of Metal-Dielectric Structures, Spacecraft Charging Technology-1978, NASA CP-2071, 507-523.
- Purvis, C.K., Stevens, N.J. and Oglebay, J.C. (1977), Charging Characteristics of Materials: Comparison of Experimental Results with Simple Analytic Models, Proceedings of the Spacecraft Charging Technology Conference, Eds. C.P. Pike and R.R. Lovell, NASA TMS-73537, 431-458.
- Robinson, J.W. and Budd, P.A. (1980), Oblique-incidence Secondary Emission, paper presented at the Spacecraft Charging Technology Conference-Colorado Springs 1980.
- Robinson, J.W. and Quôc-Nguyên, N. (1979), Electric Fields and Secondary Emission Near a Dielectric-metal Interface, IEEE Trans on Electrical Insulators, Vol. EI-14, No. 1, 14-20.
- Robinson, J.W. (1977), Charge Distributions Near Metal-Dielectric Interfaces Before and After Dielectric Surface Flashover, Proceedings of the

Spacecraft Charging Technology Conference, Eds. C.P. Pike and R.R. Lovell, NASA TMX-73537, 503-514.

Roche, J.C. and Purvis, C.K. (1979), Comparison of NASCAP Predictions with Experimental Data, Spacecraft Charging Technology-1978, NASA CP-2071, 734-747.

Rosato, D.V. (1968), Environmental Effects on Polymeric Materials, Vol. 1 Environments, Eds. D.V. Rosato and R.T. Schwartz, Interscience, 798-990.

Rosen, A. (1975), Large Discharges and Arcs on Spacecraft, Astronautics and Aeronautics, June, 36-44.

Sessler, G.M., West, J.E. and Berkley, D.A. (1977), Determination of Spatial Distribution of Charges in Thin Dielectrics, Phys. Res. Letters, 38, 368.

Sessler, G.M. and West, J.E. (1976), Trap Modulated Mobility of Electrons and Holes in Teflon FEP, Journal of Applied Physics, Vol. 47, No. 8, 3480-3484.

Sharp, R.D., Shelley, E.G. and Johnson, R.G. (1970), Preliminary Results of a Low Energy Particle Survey at Synchronous Altitude, Journal of Geophysical Res., 75, 6092

Stannard, P.R. and Katz, I. (1981), Bootstrap Charging of Surfaces Composed of Multiple Materials, paper presented at the 1981 IEEE Annual Conference on Nuclear and Space Radiation Effects, Seattle.

Stevens, N.J. (1981), Voltage Gradients in Solar Array Cavities as Possible Breakdown Sites in Spacecraft-charging-induced Discharges, paper presented at the 1981 IEEE Annual Conference on Nuclear and Space Radiation Effects, Seattle.

Stevens, N.J. (1980), Modelling of Environmentally Induced Discharges in Geosynchronous Satellites, IEEE Trans. on Nuclear Science, Vol. NS-27, No. 6, 1792-1796.

Stevens, N.J., Purvis, C.K. and Staskus, J.V. (1978), Insulator Edge Voltage Gradient Effects in Spacecraft Charging Phenomena, IEEE Trans. on Nuclear Science, Vol. NS-25, No. 6, 1304-1309.

Stevens, N.J., Berkopec, F.O., Staskus, J.V., Blech, R.A. and Narciso, S.J. (1977), Testing of Typical Spacecraft Materials in a Simulated Substorm Environment, Proceedings of the Spacecraft Charging Technology Conference, Eds. C.P. Pike and R.R. Lovell, NASA TMX-73537, 431-458.

Stenner, R., Marks, R. and Dancz, J. (1980), Physical Modelling of Spacecraft Discharge Processes and Associated Electron Blowoff, IEEE Trans on Nuclear Science, Vol. NS-27, No. 6, 1780-1785.

Streed, E.R. and Arvensen, J.C. (1967), A review of the Status of Spacecraft Thermal Control Materials, The Effects of the Space Environment on Materials, Science of Advanced Materials and Process Engineering Proceedings, 11, Society of Aerospace Material and Process Engineers, 181-192.

van Lint, V.A.J., Flanagan, T.M., Leadon, R.E., Naber, J.A. and Rogers, V.C. (1980), Mechanisms of Radiation Effects in Electronic Materials Vol. 1, John Wiley and Sons.

Wall, J.A., Burke, E.A. and Frederickson A.R. (1977), Results of a Literature Search on Dielectric Properties and Electron Interaction Phenomena Related to Spacecraft Charging, Proceedings of the Spacecraft Charging Technology Conference, Eds. C.P. Pike and R.R. Lovell, NASA TMS-73537, 569-592.

Weber, C. (1967), Numerical Solution of Laplace's and Poisson's Equations and the Calculation of Electron Trajectories and Electron Beams, in Focusing of Charged Particles Vol. 1, Ed. A. Septier, Academic Press, New York, 45-98.

Yadlowsky, E.J., Hazelton, R.C. and Churchill, R.J. (1980) Characteristics of Edge Breakdowns on Teflon Samples, IEEE Trans on Nuclear Science, Vol. NS-27, No. 6, 1765-1769.